# First Responder Immersive Training Simulation Environment (FRITSE): Downwind Hazard Modeling of Scenarios Final Contract Report

by
Fue-Sang Lien, Kun-Jung Hsieh and Hua Ji
Email: **fslien@watcfd.com**
Web site: **http://www.watcfd.com/**


Waterloo CFD Engineering Consulting Inc. (WATCFD)
534 Paradise Crescent, Waterloo
Ontario, N2L 3G1

Prepared for
Defence R&D Canada, Suffield Research Centre

Contract Number: W7702-25291/001/SV
Technical Authority: Eugene Yee

July 31, 2014

Prepared by:
Fue-Sang Lien, Kun-Jung Hsieh and Hua Ji
Waterloo CFD Engineering Consulting Inc. (WATCFD)
534 Paradise Crescent, Waterloo
Ontario, N2L 3G1

PWGSC Number: W7702-25291/001/SV

CSA: Eugene Yee, DRDC - Suffield Research Centre (403) 544-4605

The scientific or technical validity of this Contract Report is entirely the responsibility of the Contractor and the contents do not necessarily have the approval or endorsement of the Department of National Defence of Canada.

# ABSTRACT

In the Chemical, Biological, Radiological-Nuclear and Explosives Research and Technology Initiative (CRTI) Project 09-509TD, a persistent, highly realistic, game-based synthetic environment (SE) for incident commanders and first responders to conduct individual and/or team training and collaboration (at the tactical and/or strategic levels) to address deliberate or accidental Chemical, Biological, Radiological, Nuclear and Explosives (CBRNE) releases in an urban environment has been proposed. This will be achieved by integrating a state-of-the-science physics-based urban flow/dispersion modeling system and a high-fidelity building-aware Geographic Information System (GIS) representation of a real cityscape (The City of Calgary) with a proven game-based simulation engine developed by 3DInternet Inc. WATCFD is responsible for the provision of hazardous plume entities to the game-based simulation engine. The objective of this report is to provide a technical description of modeling and simulation of the highly disturbed building-induced flow field in downtown Calgary and the transport and dispersion of hazardous agents released into this complex flow field using the computational fluid dynamics (CFD) model urbanSTREAM, which consists of

1. generation of a structured computational grid from a building database for an urban landscape in the form of an Arc View Shape file for the City of Calgary;
2. generation of highly disturbed building-aware flow fields in the urban environment for various inflow conditions;
3. development of a heavy-gas modeling capability and implementing it in the dispersion module urbanEU;
4. simulation of dispersion for each of the CBRNE hazard scenarios described in the portfolio and archiving the concentration field as a function of space and time;
5. conversion of the concentration field datasets from various simulations into a "compact data" format compatible for utilization in the game-based simulation environment developed by 3DInternet Inc.;
6. provision of input/support for presentations in the 2012 annual Public Security S&T Summer Symposium

It is envisaged that the development of the game-based virtual reality CBRNE training environment developed in the present project will provide the highest quality training to incident commanders and first responders, allowing the end user to experience and respond to realistic high-risk scenarios involving CBRNE hazards in a complex cityscape in a completely safe and controlled environment.

**EXECUTIVE SUMMARY**

# First Responder Immersive Training Simulation Environment

Fue-Sang Lien[1,2], Kun-Jung Hsieh[1] and Hua Ji[1]

[1]: Waterloo CFD Engineering Consulting Inc. (WATCFD)
[2]: University of Waterloo

**Background:** Considerable efforts have been made to strengthen Canada's preparedness for, prevention of, response to, and recovery from Chemical, Biological, Radiological, Nuclear and Explosives (CBRNE) threats to public safety and security. An important part of this effort involves CBRNE training for first responders in order to provide them with the knowledge, competence and confidence to deal with a wide spectrum of CBRNE hazards. Presently, scenario-based training in Canada is limited to first responders' hands-on training (including live-agent training) at Defence R&D Canada, Suffield Research Centre and the Canadian Emergency Management College (CEMC). However, this training does not utilize simulated urban environments with realistic hazard scenarios. Consequently, there is a significant capability gap in providing realistic CBRNE training for first responders. In this project, a game-based synthetic environment will be developed to address this capability gap. 3DInternet Inc. will integrate their unique simulation engine with a downwind hazard dispersion model, a Geographic Information System (GIS) representation of Calgary, and expert first responder input to produce the overall simulation environment for training. The development of a portfolio of CBRNE hazard scenarios (e.g., a derailment and explosion involving volatile chlorine tanker in downtown Calgary, etc.) will be led by LuomaTech Inc., and all partners in the project will be involved in the portfolio development. WATCFD will utilize building-resolving urban flow/dispersion models to provide hazardous plume entities for the game-based simulation engine to be developed by 3DInternet Inc. This training environment will enable first responders to train together more frequently against a wider spectrum of realistic CBRNE hazard scenarios.

**Results:** This report provides a technical description of the modeling and simulation of the highly disturbed building-induced flow field in downtown Calgary and the transport and dispersion of hazardous agents released into this complex flow field using the computational fluid dynamics model urbanSTREAM developed by WATCFD which consists of

1. generation of a structured computational grid from a building database for an urban landscape in the form of an Arc View Shape file for the City of Calgary;
2. generation of the highly disturbed building-aware flow fields in the urban environment for various inflow conditions;
3. development of a heavy-gas modeling capability and implementing it in the dispersion module urbanEU;
4. simulation of dispersion for each of the CBRNE hazard scenarios described in the portfolio and archiving the concentration field as a function of space and time;
5. conversion of the concentration field data sets from the various simulations into a "compact data" format compatible for utilization in the game-based simulation environment developed by 3DInternet Inc.;

6. provision of input/support for presentations in the 2012 annual Public Security S&T Summer Symposium

**Significance:** It is envisaged that the development of the game-based virtual reality CBRNE training environment developed in the present project will provide the highest quality training to incident commanders and first responders, allowing the end user to experience and respond to realistic high-risk scenarios involving CBRNE hazards in a complex cityscape in a completely safe and controlled environment.

**Table of Contents**

**List of Tables**

## List of Figures

**Acknowledgements**

# 1. INTRODUCTION

Since the terrorist attacks of September 11, 2001, and the subsequent establishment of the Chemical, Biological, Radiological-Nuclear, and Explosives (CBRNE) Research and Technology Initiative (CRTI), considerable efforts have been made to strengthen Canada's preparedness for, prevention of, response to, and recovery from CBRNE threats to public safety and security. An important part of this effort involves CBRNE training for first responders in order to provide them with the knowledge, competence and confidence to deal with a wide spectrum of CBRNE incidents. At the present time, scenario-based training is limited to first responders' hands-on training at Defence R&D Canada, Suffield Research Centre (Counter Terrorism Technology Centre - CTTC) and other courses offered by the Canadian Emergency Management College (CEMC). A new CRTI project (09-509TD) has been funded to augment our current capabilities to train first responders to respond to CBRNE incidents.

The objective of this project is to develop a highly realistic, game-based simulation environment for first responders to conduct individual and/or team training and collaborations in addressing deliberate or accidental releases of CBRNE materials in a real cityscape. This will be achieved by integrating a physics-based urban flow and dispersion modeling system developed in previous CRTI projects and a high-fidelity GIS representation of an urban environment with a proven game-based simulation engine to produce a simulation environment for CBRNE training/ education that is realistic and engaging.

Under the current project, the following five tasks have been completed by WATCFD, which will be addressed in detail in the present report.

1. Generate an appropriate structured computational grid from a building database in the form of an Arc View Shapefile for the City of Calgary for the use of the subsequent simulation of the flow and dispersion of materials released into this urban environment;
2. For a given set of inflow conditions (mean wind speed, wind direction, and turbulence intensities), simulate the highly disturbed building-aware flow field in the urban environment and generate building-aware flow fields for various inflow conditions;
3. For a given portfolio of CBRNE hazard scenarios, and using the disturbed flow fields generated in Task 2 above, simulate the dispersion for each of these scenarios in the urban environment and archive the concentration field as a function of space and time;
4. Convert the concentration field datasets from the various simulations in a format compatible for utilization in the game-based simulation environment developed by 3DInternet Inc. (http://www.3dinternet.com/);
5. Provide input/support for presentations and/or technical papers prepared for various scientific meetings and symposia (including the annual Public Security S&T Summer Symposium).

In addition, a heavy-gas (or dense-gas) modeling capability has been also developed in this project, which is relevant to Scenario 2 (to be discussed in Sections 3 and 4), in which the derailment of a rail car containing chlorine is considered. Chlorine is a heavier-than-air (dense) gas.

## 2. TECHNICAL DESCRIPTION

### 2.1 Overview of the Integrated Urban Flow and Dispersion Modeling System

The urban modeling system developed from a previous CRTI Project 02-0093RD includes five main modules: urbanGRID, urbanSTREAM, urbanEU, urbanAEU, and urbanPOST. These modules and how they interface with each other and with other project components have been summarized in Figure 2 of the report by Yee et al. (2007). As stated in this report, urbanGRID imports building information encoded in Environmental Systems Research Institute (ESRI) Shapefiles and uses this data to generate a structured grid over a user-selected computational domain in a given cityscape. Furthermore, urbanGRID imports three-dimensional meteorological fields (e.g., mean wind, turbulence kinetic energy, etc.) provided by urban GEM LAM[1] and uses this information to provide inflow boundary conditions for the urban microscale flow model: urbanSTREAM. The structured grid and inflow boundary conditions provided by urbanGRID are used as inputs by urbanSTREAM to simulate the flows around and within the complex geometries of buildings in the cityscape, and to provide the high-resolution wind and turbulence fields for dispersion modeling. The two Eulerian dispersion models urbanEU (source-oriented) and urbanAEU (receptor-oriented) use the wind and turbulence fields provided by urbanSTREAM to simulate the dispersion of contaminants in the urban domain. Finally, urbanPOST is the post-processing module to process the primary output files from urbanSTREAM, which can then be visualized by third party visualization programs such as Tecplot[2].

To consider effect from complex terrain on a flow as required in the present project, urbanSTREAM applies curvilinear coordinates, allowing for the use of a body-fitted (or boundary-fitted) mesh to include the topographic capability. The governing equations written in curvilinear coordinates can be converted from those written in Cartesian coordinates based on a one-to-one (locally invertible) mapping (or transformation). For example, all the governing partial differential equations under Cartesian coordinates can be written in a generic form as follows,

$$\frac{\partial \phi}{\partial t} + \frac{\partial \overline{u}_j \phi}{\partial x_j} = \frac{\partial}{\partial x_j}\left( \Gamma_\phi \frac{\partial \phi}{\partial x_j} \right) + S_\phi \tag{1}$$

for a scalar $\phi$, which can be identified with any of the mean Cartesian velocity components $\overline{u}_j$, turbulence kinetic energy $k$, viscous dissipation $\varepsilon$, mean concentration $C$, or influence function $C^*$. Transforming the above equation from 3-D Cartesian coordinates to 3-D curvilinear coordinates, represented by $\xi^j$ ( $j = 1, 2, 3$ and $\xi^1 = \xi$, $\xi^2 = \eta$, $\xi^3 = \zeta$ ), produces a partial different equation in the following generic form,

---

[1] urban GEM LAM is a prognostic mesoscale model with an urban parameterization developed by Environment Canada for CRTI Project 02-0093RD.
[2] Tecplot (http://www.tecplot.com/) is a commercially-available CFD visualization software.

$$\frac{\partial \phi}{\partial t} + \frac{\partial U^j \phi}{\partial \xi^j} = \frac{\partial}{\partial \xi^j}\left[\Gamma_\phi J\left(q_{mm}^{jn}\frac{\partial \phi}{\partial \xi^n}\right)\right] + JS_\phi \tag{2}$$

where $m, n = 1, 2, 3$, are indices following Einstein summation convention, J is the Jacobian matrix of the transformation, that is,

$$J = \begin{bmatrix} x_\xi & x_\eta & x_\zeta \\ y_\xi & y_\eta & y_\zeta \\ z_\xi & z_\eta & z_\zeta \end{bmatrix} = \begin{vmatrix} \dfrac{\partial x}{\partial \xi} & \dfrac{\partial x}{\partial \eta} & \dfrac{\partial x}{\partial \zeta} \\ \dfrac{\partial y}{\partial \xi} & \dfrac{\partial y}{\partial \eta} & \dfrac{\partial y}{\partial \zeta} \\ \dfrac{\partial z}{\partial \xi} & \dfrac{\partial z}{\partial \eta} & \dfrac{\partial z}{\partial \zeta} \end{vmatrix} \tag{3}$$

and $U^j$ ($j = 1, 2, 3$) are the contravariant velocities, expressed as follows,

$$U^1 = U = J\left(u\xi_x + v\xi_y + w\xi_z\right) = J\left(u\frac{\partial \xi}{\partial x} + v\frac{\partial \xi}{\partial y} + w\frac{\partial \xi}{\partial z}\right) \tag{4}$$

$$U^2 = V = J\left(u\eta_x + v\eta_y + w\eta_z\right) = J\left(u\frac{\partial \eta}{\partial x} + v\frac{\partial \eta}{\partial y} + w\frac{\partial \eta}{\partial z}\right) \tag{5}$$

$$U^3 = W = J\left(u\zeta_x + v\zeta_y + w\zeta_z\right) = J\left(u\frac{\partial \zeta}{\partial x} + v\frac{\partial \zeta}{\partial y} + w\frac{\partial \zeta}{\partial z}\right) \tag{6}$$

in which $u, v, w$ denote the mean Cartesian velocity components.

The fourth-order tensor $q_{mi}^{jn}$ is defined as

$$q_{mi}^{jn} = \beta_m^j \beta_i^n \tag{7}$$

where $\beta_i^j$ ($i, j = 1, 2, 3$) are the elements of the following inverse Jacobian matrix,

$$J^{-1} = \begin{vmatrix} \xi_x & \xi_y & \xi_z \\ \eta_x & \eta_y & \eta_z \\ \zeta_x & \zeta_y & \zeta_z \end{vmatrix} \tag{8}$$

The transformation of the source term $S_\phi$ is very tedious and its end result is different for each governing equation. Due to space constraints, detailed expressions of transformed $S_\phi$ are not included in this section, and interested readers can refer to Lien (1992).

## 2.2 Inflow Boundary Condition

Instead of taking inflow velocity profiles from GEM LAM solutions, the velocity profiles at the inlet (or, inflow boundary) are approximated by the following power law:

$$\frac{u(z)}{u_{10}} \approx \left(\frac{z}{10}\right)^p \quad \text{for } z \leq 400 \text{ m}$$

$$\frac{u(z)}{u_{10}} \approx \left(\frac{400}{10}\right)^{0.3} \quad \text{for } z > 400 \text{ m}$$

$$(9)$$

based on the assumption that $p \approx 0.3$, and $u_{10} \approx 5.556$ m/s (or $u_{10} \approx 20$ km/h ), where $u_{10}$ is the wind speed at 10 m above the ground. The exponent $p \approx 0.3$ in equation (9) is a good approximation for wind speeds in suburbs. The profile of turbulence kinetic energy at the inflow boundary is expressed by using the following two-layer model:

$$\text{For } z \leq h_c, \, k \approx k_{max}\left(\frac{z}{h_c}\right). \tag{10}$$

$$\text{For } z > h_c, \, k \approx \left(\frac{k_{max} - k_{min}}{h_c - h_{BL}}\right)z + \left(\frac{k_{min}h_c - k_{max}h_{BL}}{h_c - h_{BL}}\right). \tag{11}$$

In equations (10) and (11), $h_c \approx 40$ m is the average building height in the inner region shown in Figures 7 and 8 later, and $h_{BL} \approx 1000$ m is the atmospheric boundary-layer thickness. The maximum turbulence kinetic energy $k_{max} \approx 0.4 \text{ m}^2/\text{s}^2$ is estimated from the IOP9 test problem (Allwine et al., 2004) in the Joint Urban 2003 (JU2003) experiment (https://ju2003-dpg.dpg.army.mil/), and $k_{min} \approx 0.01u_{10}^2$ at $z \approx h_{BL}$. Finally, the turbulence dissipation rate, $\varepsilon$, is approximated by

$$\varepsilon = \frac{k^{3/2}}{C_\mu^{-3/4} \min(\kappa z, h_{BL}/3)} \tag{12}$$

where $\kappa = 0.42$ is the von Karman constant, and $C_\mu = 0.09$ for the standard $k - \varepsilon$ turbulence closure model.

The resulting system of partial differential equations was solved numerically using a collocated, finite-volume method and implemented in the urbanSTREAM code (Yee et al., 2007; Lien et al., 2010). Diffusive volume-face fluxes were discretized using a second-order accurate central differencing scheme (CDS). Advective volume-face fluxes were approximated using a second-order accurate Upstream Monotonic Interpolation for Scalar Transport (UMIST) scheme (Lien and Leschziner, 1994). The transient term was discretized using a fully implicit, second-order accurate three-time-level method described in Ferziger and Peric (2002). The Semi-Implicit Method for Pressure-Linked Equations (SIMPLE) algorithm (Patankar and Spalding, 1972) was

used to determine the (gauge) pressure. A nonlinear interpolation scheme (Rhie and Chow, 1983) was used to interpolate the cell face velocities from the adjacent nodal velocities at the cell centers in order to prevent checkerboard oscillations from developing in the pressure field.

## 2.3 Inclusion of Heavy Gas Capability

### 2.3.1 Mathematical formulation and numerical framework

The dispersion of a heavier-than-air (dense) gas cloud is predicted by solving the three-dimensional conservation equations for mean (ensemble-averaged) quantities in a turbulent flow field. This involves solving the conservation equations of mass, momentum, and species concentration for an isothermal (constant temperature) fluid flow based on the Reynolds-averaged Navier-Stokes (RANS) approach:

$$\frac{\partial \rho}{\partial t} + \frac{\partial}{\partial x_j}\left(\rho \bar{u}_j\right) = 0, \tag{13}$$

$$\frac{\partial}{\partial t}\left(\rho \bar{u}_i\right) + \frac{\partial}{\partial x_j}\left(\rho \bar{u}_j \bar{u}_i\right) = -\frac{\partial \bar{p}}{\partial x_i} + \frac{\partial}{\partial x_j}\left(\mu \frac{\partial \bar{u}_i}{\partial x_j}\right) - \frac{\partial}{\partial x_j}\left(\rho \overline{u_i' u_j'}\right) + \left(\rho - \rho_0\right)g_i, \tag{14}$$

$$\frac{\partial}{\partial t}\left(\rho \bar{c}_k\right) + \frac{\partial}{\partial x_j}\left(\rho \bar{u}_j \bar{c}_k\right) = \frac{\partial}{\partial x_j}\left(\rho D \frac{\partial \bar{c}_k}{\partial x_j}\right) - \frac{\partial}{\partial x_j}\left(\rho \overline{u_j' c_k'}\right), \quad k = 1, 2, \ldots, N, \tag{15}$$

where $\bar{u}_i$ is the ensemble-mean (or, Reynolds-averaged) velocity in the $x_i$-direction with $i = 1, 2, 3$ representing the $x$, $y$, and $z$ directions, respectively; $t$ is the time; $\bar{p}$ is the mean (gauge) pressure; $\mu$ is the dynamic molecular viscosity of the fluid; $\bar{c}_k$ is the mass fraction (concentration) of the $k$-th scalar (or species) in the mixture; $D$ is the molecular diffusivity of the scalar; $g_i$ is the gravitational acceleration in the $x_i$-direction; $\rho$ is the density of the fluid; and, $\rho_0$ is a reference density (chosen herein as the density of air at sea level with a representative value of $\rho_0 = 1.25$ kg m$^{-3}$). Summation is implied by repeated indices. Reynolds-averaging of the momentum transport equation (14) and the advection-diffusion equation (15) gives rise, respectively, to the Reynolds stresses which are defined as the tensor $\overline{u_i' u_j'}$ and the turbulent scalar fluxes which are defined as the vector $\overline{u_j' c_k'}$ ($k = 1, 2, \ldots, N$). These equations, along with an equation of state that uses the ideal gas law approximation for the density, namely

$$\rho = \frac{P}{T \sum_{k=1}^{N} R_k \bar{c}_k} = \frac{P}{R_* T}, \tag{16}$$

are the main governing equations. Here, $P$ is the absolute pressure, $T$ is the absolute temperature (assumed to be a constant for the isothermal atmosphere considered herein), and $R_k \equiv G/M_k$ is the specific gas constant for species $k$ ($G = 8.314472 \times 10^3$ J K$^{-1}$ kg-mol$^{-1}$ is the universal gas constant and $M_k$ is the molecular weight of species $k$). Also, in equation (16), $R_*$ is the specific

gas constant for the mixture consisting of $N$ species. It is noted that the gauge pressure $\bar{p}$ in equation (14) is the pressure deviation from an adiabatic atmosphere in hydrostatic equilibrium with corresponding density $\rho_0$, with the result that the absolute pressure in equation (16) is related to the gauge pressure in equation (14) as $P = \bar{p} + P_0$, where $P_0$ is some nominal atmospheric pressure level in the adiabatic atmosphere (e.g., at the ground surface).

If the density variations are *not too large*, we can apply the Boussinesq approximation to equations (13), (14) and (15). The main step in developing the Boussinesq approximation is to treat the density as a constant (which can be taken as the reference density $\rho_0$) in the unsteady, convective and diffusive terms, while retaining the density variations only in the buoyancy (gravity) term $(\rho - \rho_0)g_i$ in the mean momentum transport equation. This approach was used by Perdikaris and Mayinger (1993) and Scargiali et al. (2005) to simulate dense gas dispersion over a topographically complex terrain. However, the approximation for the buoyancy term given in these two papers is not correctly stated. In consequence, we provide a simple derivation of the Boussinesq approximation of $(\rho - \rho_0)g_i$ in the context of the dispersion of a heavier-than-air gas released into the atmosphere. Towards this purpose, consider a Taylor series expansion of the density $\rho = \rho(P, T, \bar{c}_1, \ldots, \bar{c}_N)$ to first order about a reference state (denoted using a subscript 0) given by

$$\rho = \rho_0 + \left.\frac{\partial \rho}{\partial P}\right|_0 (P - P_0) + \left.\frac{\partial \rho}{\partial T}\right|_0 (T - T_0) + \sum_{k=1}^{N} \left.\frac{\partial \rho}{\partial \bar{c}_k}\right|_0 (\bar{c}_k - \bar{c}_{k,0}), \tag{17}$$

with the partial derivatives in equation (17) evaluated at the reference state $(P_0, T_0, \bar{c}_{1,0}, \ldots, \bar{c}_{N,0})$ and $\rho_0 = \rho(P_0, T_0, \bar{c}_{1,0}, \ldots, \bar{c}_{N,0})$. For an isothermal atmosphere, the third term on the right-hand side of equation (17) vanishes identically. Inserting the ideal gas law of equation (16) into equation (17), the density perturbations (from the reference state) can be expressed as follows:

$$\frac{\rho - \rho_0}{\rho_0} \equiv \frac{\delta\rho}{\rho_0} = \frac{(P - P_0)}{P_0} - \sum_{k=1}^{N} \alpha_k (\bar{c}_k - \bar{c}_{k,o}) \equiv \frac{\delta P}{P_0} - \sum_{k=1}^{N} \alpha_k (\bar{c}_k - \bar{c}_{k,o}), \tag{18}$$

where $\delta\rho \equiv (\rho - \rho_0)$ and $\delta P \equiv (P - P_0) = \bar{p}$ are used to denote the density and pressure perturbations, respectively; and,

$$\alpha_k \equiv -\frac{1}{\rho_0} \left.\frac{\partial \rho}{\partial \bar{c}_k}\right|_0 = \frac{R_k}{\sum_{i=1}^{N} R_i \bar{c}_{i,0}}, \tag{19}$$

is the volumetric expansion coefficient arising from perturbations in the concentration of species *k*.

To simplify the approximation in equation (18), we consider order-of-magnitude estimates for $\delta P / P_0$ in comparison to $\delta \rho / \rho_0$. To proceed, it is assumed that the pressure gradient term in the mean momentum transport equation (14) is of the same order of magnitude as the buoyancy term and, with the buoyancy force acting in the $y$ ($i = 2$) direction, this implies within the Boussinesq approximation that

$$\left| \frac{1}{\rho_0} \frac{\partial \overline{p}}{\partial y} \right| \equiv \left| \frac{1}{\rho_0} \frac{\partial \delta P}{\partial y} \right| \approx \left| \frac{\rho - \rho_0}{\rho_0} g \right| \equiv \left| \frac{\delta \rho}{\rho_0} g \right|. \tag{20}$$

An estimate of the magnitude of the term on the left-hand-side of equation (20) [obtained by using the ideal gas law of equation (16) for the reference state] gives

$$\left| \frac{1}{\rho_0} \frac{\partial \delta P}{\partial y} \right| \approx \frac{R_* T_0}{P_0} \frac{|\delta P|}{l_y}, \tag{21}$$

where $l_y$ is a representative or characteristic spatial scale of the circulations in the atmospheric surface layer (and typically, $l_y = O(100)$ m in an adiabatic atmosphere). Insertion of the order-of-magnitude estimate of equation (21) into equation (20) leads to

$$\frac{|\delta P|}{P_0} \approx \frac{l_y g}{R_* T_0} \frac{|\delta \rho|}{\rho_0} = \frac{l_y g}{P_0 / \rho_0} \frac{|\delta \rho|}{\rho_0} = \frac{l_y g \rho_0}{P_0} \frac{|\delta \rho|}{\rho_0}. \tag{22}$$

To proceed further, we need an estimate for $P_0$ which can be obtained as follows. The reference pressure $P_0$ at the Earth's surface is determined for an atmosphere in hydrostatic equilibrium, so $P_0 \approx \rho_0 g H_0$ where $H_0$ is the effective height in the atmosphere where the pressure is equal to zero (approximately). $H_0$ is estimated to be about $H_0 = O(8000)$ m (Pielke, 2002). Now, using this estimate for $P_0$ in equation (22), it follows that

$$\frac{|\delta P|}{P_0} \approx \frac{l_y g \rho_0}{P_0} \frac{|\delta \rho|}{\rho_0} = \frac{l_y g \rho_0}{\rho_0 g H_0} \frac{|\delta \rho|}{\rho_0} = \frac{l_y}{H_0} \frac{|\delta \rho|}{\rho_0}, \tag{23}$$

from which it is seen that $|\delta P| / P_0 << |\delta \rho| / \rho_0$ because $l_y / H_0 << 1$. From this observation, it is now evident that the density perturbations in equation (18) are well approximated as

$$\frac{\rho - \rho_0}{\rho_0} \equiv \frac{\delta \rho}{\rho_0} \approx -\sum_{k=1}^{N} \alpha_k \left( \overline{c}_k - \overline{c}_{k,o} \right). \tag{24}$$

Finally, for the special case of a two-component mixture consisting of air ($a$, or species $k = 1$) and a contaminant species ($g$, or species $k = 2$) [chlorine, Freon-12 or some other contaminant in the cases considered herein], the density perturbation of equation (24) reduces to

$$\frac{\rho - \rho_0}{\rho_0} = \alpha \bar{c} , \tag{25}$$

on noting $\bar{c}_a = 1 - \bar{c}_g \equiv 1 - \bar{c}$, $\alpha \equiv (\rho_g - \rho_a)/\rho_g$, and assuming that the concentrations of air and contaminant gas in the reference state are $\bar{c}_{a,0} = 1$ and $\bar{c}_{g,0} = 1 - \bar{c}_{a,0} = 0$. Using the density perturbation given by equation (25), the buoyancy term can be approximated as follows:

$$(\rho - \rho_0) g_i = \rho_0 \alpha \bar{c} g_i . \tag{26}$$

For the simulation of the dense gas dispersion scenarios in this report, equation (26) will be used to model the buoyancy term in the mean momentum equation within the framework of the Boussinesq approximation. It is noted that this approximation for the buoyancy term differs from that used in Scargiali et al. (2005) in that the quantity $\alpha$ involves normalization by $\rho_a$ rather than $\rho_g$ (as used in the current formulation). Finally, for a two-component mixture consisting of air and a contaminant gas, we need only consider a transport equation for the contaminant species concentration $\bar{c}$ because the concentration of the air in the mixture is determined from $(1 - \bar{c})$.

Within the framework of the standard high-Reynolds-number $k - \varepsilon$ model, the Reynolds stresses $\overline{u_i' u_j'}$ and the turbulent scalar fluxes $\overline{u_j' c'}$, required to close the transport equations for the mean momentum and mean concentration of the contaminant species, are modeled using the Boussinesq eddy-viscosity approximation (which should not be confused with the Boussinesq approximation for buoyant-driven flows) and the simple gradient diffusion hypothesis, respectively, as follows:

$$\overline{u_i' u_j'} = \frac{2}{3} k \delta_{ij} - \nu_t \left( \frac{\partial \bar{u}_i}{\partial x_j} + \frac{\partial \bar{u}_j}{\partial x_i} \right), \tag{27}$$

$$\overline{u_j' c'} = -\frac{\nu_t}{\sigma_c} \frac{\partial \bar{c}}{\partial x_j}, \tag{28}$$

where $\nu_t = C_\mu k^2 / \varepsilon$ is the kinematic (turbulent) eddy viscosity, $C_\mu = 0.09$ is a model constant, $\sigma_c = 0.63$ is the turbulent Schmidt number for the scalar, $k$ is the turbulence kinetic energy, $\varepsilon$ is the dissipation rate of $k$, and $\delta_{ij}$ is the Kronecker delta function. The modeled transport equations for $k$ and $\varepsilon$ in the standard $k - \varepsilon$ model with buoyancy terms assume the following form within the context of the Boussinesq approximation:

$$\frac{\partial}{\partial t}(\rho_0 k) + \frac{\partial}{\partial x_j}(\rho_0 \bar{u}_j k) = \frac{\partial}{\partial x_j}\left( \rho_0 \frac{\nu_t}{\sigma_k} \frac{\partial k}{\partial x_j} \right) + \rho_0 (P_k + G_k) - \rho_0 \varepsilon , \tag{29}$$

$$\frac{\partial}{\partial t}(\rho_0 \varepsilon) + \frac{\partial}{\partial x_j}(\rho_0 \bar{u}_j \varepsilon) = \frac{\partial}{\partial x_j}\left( \rho_0 \frac{\nu_t}{\sigma_\varepsilon} \frac{\partial \varepsilon}{\partial x_j} \right) + C_{\varepsilon 1} \rho_0 \frac{\varepsilon}{k}(P_k + G_k)(1 + C_{\varepsilon 3} R_f) - C_{\varepsilon 2} \rho_0 \frac{\varepsilon^2}{k} , \tag{30}$$

where $P_k \equiv -\overline{u_i' u_j'}\, \partial \overline{u}_i / \partial x_j$ is the turbulence kinetic energy production term, $\sigma_k = 1.0$, $\sigma_\varepsilon = 1.3$, $C_{\varepsilon 1} = 1.44$, and $C_{\varepsilon 2} = 1.92$ are model (closure) constants. Furthermore, in equations (29) and (30), $G_k$ is the production term relating to buoyancy and is given by

$$G_k = -\alpha g_i \frac{\nu_t}{\sigma_c} \frac{\partial \overline{c}}{\partial x_i},$$

(31)

for the case of a two-component mixture (where $\overline{c}$ is the contaminant species concentration). In equation (30), $R_f = -G_k / (P_k + G_k)$ is the flux Richardson number and $C_{\varepsilon 3} = 0.8$ is an additional model constant (Rodi, 1978) that is applicable both for vertical and horizontal buoyant shear layers. In particular, for a vertical shear layer where the lateral velocity component is normal to the direction of gravity, we note that $R_f = 0$. This is the case of relevance for our investigation.

### 2.3.2 Validation test case: Thorney Island

Extensive field trials on the dispersion of dense gas clouds at ground level in the atmosphere were performed by the Health and Safety Executive in Great Britain. The trials were conducted on the Thorney Island airfield in southern England from July 1982 to July 1983. In these trials, isothermal gas clouds of fixed volume and of varying density were instantaneously released into the atmosphere. The gas concentrations in the cloud, consisting of Freon-12 and air mixtures, were measured using sensors placed at various downwind fetches from the release location. In this paper, we consider the trials conducted in the second phase of the Thorney Island test series (Davies and Singh, 1985). In these experiments, the dense gas cloud dispersion was conducted in the presence of an obstacle. The obstacle used was a sharp-edged solid cube with a dimension of 9 m on each side. In the instantaneous releases, a cylindrical gas tent of 14 m diameter and 13 m height with a total volume of 2000 m$^3$ was filled with a mixture of Freon-12 (dichlorodifluoromethane, $CCl_2F_2$) and nitrogen. More specifically, the released gas consisted of a mixture of 68.4% nitrogen and 31.6% Freon-12 (w/w) to give a mixture density that is roughly twice that of air. The top and sides of the cylindrical tent were quickly removed, leaving an upright cylinder of dense gas exposed to the ambient conditions. The mixture immediately began to expand outwards isotropically in all horizontal directions by gravitational slumping. The gravitational slumping and atmospheric dispersion of this dense gas cloud is affected by its interaction with the cubical obstacle, either located downwind or upwind of the release.

In trial number 26, the windward face of the cubical obstacle was located 50 m downwind from the center of the cylindrical gas tent. The measured wind speed at 10 m above the ground was 1.9 m/s, and the concentration of the gas cloud was measured on the windward and leeward faces of the obstacle at heights of 6.4 m and 0.4 m above ground level, respectively. In trial number 29, the leeward face of the cubical obstacle was located 27 m upwind from the center of the cylindrical gas tent. The measured wind speed at 10 m above the ground was 5.6 m/s, and the concentration was measured on the leeward face of the obstacle at the height of 0.4 m above ground level.

Simulations of the flow and dense gas dispersion for trial number 26 were conducted on a computational mesh of 189×60×83 control volumes (nodes) in a spatial domain (shown in Figure

9

1) with an extent of $16.4H \times 4.4H \times 14.0H$ in the streamwise, vertical and spanwise directions, respectively, where $H = 9$ m is the height of the cubical obstacle. The simulations for trial number 29 were performed on a computational mesh of $139 \times 60 \times 83$ nodes in a spatial domain that spanned $15.9H \times 4.4H \times 14.0H$ in the streamwise, vertical and spanwise directions, respectively. The mesh used for the computational domain of trial number 29 (not shown) was very similar to that used in trial number 26, where the grid lines were preferentially concentrated near the solid surfaces in order to better capture the expected sharp gradients of the flow properties here.

At the inlet boundary of the spatial domain used for the simulations, the vertical profile of the mean streamwise velocity was approximated using a power-law functional form $\bar{u}(y) = \bar{u}_0 \left( y / y_0 \right)^n$, where $\bar{u}_0$ is the reference velocity at the reference height $y_0 = 10$ m. Table 1 summarizes the values of $\bar{u}_0$ and $n$ used in the simulations for trial numbers 26 and 29. This power-law profile was also used by Qin et al. (2007) and Sklavounos and Rigas (2004) for their simulations of Thorney Island. At the outlet boundary, zero Neumann boundary conditions were imposed on all flow variables. At the spanwise and top boundaries, symmetry and free-slip boundary conditions were applied to the flow variables, respectively. At all the solid boundaries (ground and obstacle faces), standard wall functions were used for the mean velocities and turbulence quantities, and the zero Neumann boundary condition was applied for the concentration of the gas (implying no flux of material across the solid boundary).

In the simulations, computations were conducted firstly to predict the steady-state flow field, including as such the complex influence of both the cylindrical gas tent and the cubical obstacle on the flow. This disturbed flow field was then used as the initial condition for the subsequent predictions of the dense gas dispersion, which occurred immediately after the collapse of the cylindrical gas tent. The gas mixture inside the cylindrical tent was released instantaneously to the atmosphere at time $t = 0$ s. Figures 2 and 3 show the mean flow streamlines and contours of concentration at different times after the dense gas cloud was released and documents the time evolution of dense gas cloud. The gravity slumping effect on the dispersion can be seen clearly in both figures, particularly at the earlier times where the streamlines within the highly concentrated gas cloud exhibit a strong downward bulk motion. Note that initially the buoyancy generated forces and pressure gradients arising from density differences between the gas cloud and its environment lead to a bulk motion that causes the dense cloud to spread in all directions near the release location (including a lateral spreading, as well as an upwind spreading against the prevailing wind direction). Further downstream from the release, the bulk flow resulting from the gravitational slumping weakens as diffusion, mixing, and entrainment between the gas cloud and the ambient air reduces the negative buoyancy effects of the cloud and strengthens the influence of the externally imposed velocity field on the transport and dispersion of the cloud. It is noted in trial number 26 that the dense gas cloud flows around and over the cubical obstacle located downwind of the release (cf. Figure 2). In contrast, for trial number 29, the cubical obstacle located upwind of the release is seen to block the further upwind spread of the dense gas cloud arising from the gravitational slumping. Also, in addition to the blocking effect, the gas cloud undergoes increased dilution in the wake of the upstream cubical obstacle (cf. Figure 3), as well as retention or "hold-up" of the material within the wake of the obstacle followed by a slow detrainment of material from the wake. This retention of material in the wake followed

10

subsequently by the detrainment of this material converts the putative instantaneous release into a time-varying one.

Figures 4 and 5 display a comparison between the measured and predicted gas concentration time histories for trial numbers 26 and 29, respectively. In particular, Figure 4 shows that the time histories of concentration observed at the windward and leeward faces of the cubical obstacle are quite different. Note that the persistence of the gas cloud (as measured by the difference between the arrival and departure times of the cloud) observed at the leeward face of the cubical obstacle is significantly greater than that observed at the windward face. This demonstrates the effect of the obstacle on dispersion, where the recirculation bubble in the wake region of the obstacle entrains and "holds-up" (traps) the contaminant material of the gas cloud. The hold-up mechanism within the wake of the obstacle is correctly predicted by the model.

Generally, numerical predictions of concentration are seen to be in quite good agreement with the experimental data. It is noted that in interpreting the level of agreement between predictions and measurements, one needs to recognize that the measurements of the short time-averaged concentration obtained in trial numbers 26 and 29 correspond to one realization of the instantaneous dispersion, whereas the predictions correspond to an ensemble-averaged concentration (and, as such, is associated with an average over an ensemble of realizations of the instantaneous dispersion). Because the model prediction is compared to one realization out of the ensemble of all possible realizations, the model cannot be expected to provide greater precision in its predictions than the expected variability in the atmospheric dispersion. Keeping this caveat in mind, the discrepancies between the predictions and the measurements could be attributed to the use of the standard $k-\varepsilon$ turbulence model. It is well known that the standard $k-\varepsilon$ model tends to over-predict levels of the turbulence kinetic energy for a flow impinging on a solid obstacle [the so-called the "stagnation point anomaly", (Durbin, 1996)], resulting in prediction of a larger recirculation bubble in the wake region of a three-dimensional obstacle than is actually observed.

For trial number 26, the more pronounced impingement of the approaching flow on the front face of the cylindrical gas tent resulting in a predicted larger recirculation bubble in the wake region of the tent will have the tendency to dilute the gas concentration faster after the tent collapses. In consequence, this will lead to a lower predicted concentration downstream of the cylindrical gas tent when compared to the associated measured concentration, as can be seen in Figure 4. For trial number 29, a larger recirculation bubble behind the upwind cubical obstacle will entrain material from the dense gas cloud (that has spread upwind owing to the gravity slumping) into the wake earlier. This effect will result in an earlier predicted arrival time for the cloud (at the leeward face of the upwind obstacle) in comparison to the measurements, as can be seen in Figure 5.

The effect of the buoyancy production term $G_k$ in the $k-\varepsilon$ model [cf. equations (29) and (30)] on the prediction of dense gas dispersion is investigated and demonstrated in Figure 6. It was found that the inclusion of $G_k$ term in the $k-\varepsilon$ model suppresses the turbulence kinetic energy, particularly in the wake region of the obstacle, which is not too surprising owing to the negative buoyancy effect of the dense gas cloud. In contrast, the effect of the $G_k$ term on the prediction of the concentration levels in the cloud appears to be insignificant. This observation is similar to the

findings of Worthy et al. (2001), where they reported that the $G_k$ term made very little difference to the modeling of buoyant thermal plumes.


## 3. DESCRIPTION OF SCENARIOS – DOWNWIND HAZARD MODELING

The downwind hazard modeling for the multi-spectrum scenario will consist of the following components, and will involve two primary locations in Calgary; namely along the railway tracks south of the intersection of (1) 9th Avenue SE and 4th Street SE and (2) 9th Avenue SW and 11th Street SW. The release involving the van will take place within about 1 block of the "accidental" release along the railway line. Suggested locations relative to the primary release along the railway line are summarized below. Note that the release involving chlorine and a chemical agent each involves two components – an near-instantaneous release and a longer continuous release involving evaporation of the material. During the evaporation phase, first responders with the proper detection equipment may be able to identify the chemical agent released from the nearby van. The toxic industrial materials can be identified probably from UN labels on the railway tanker cars.


### 3.1 Scenario 1: derailment of a rail car containing methanol (UN 1230, Class 3) – liquid density of methanol is 791 kg/m$^3$

Rail car could potentially release up to 34,500 US gallons of methanol. It will be assumed that the rail car is only ¾ full, so the rail car only holds about 25,000 US gallons of methanol. Methanol is flammable, and it is assumed that the process causing the derailment also results in a fire. The fire is assumed to destroy about 20% of the methanol. Of the remaining methanol not destroyed by the fire (about 20,000 US gallons, or about 75 m$^3$), roughly ½ of this volume was "flashed" to the atmosphere in form of vapor/aerosol droplets and remaining methanol was released to atmosphere in continuous manner at a constant emission rate. Initial "flash" caused instantaneous release of 791×37.5 ≈ 30,000 kg of methanol. The remaining methanol was "boiled" off by the fire at a constant emission rate of 1000 kg/min (for about 30 min).

**Location 1:** 51 deg, 02', 37.12" N, 114 deg, 03', 11.89" W
**Location 2:** 51 deg, 02', 41.07" N, 114 deg, 05', 14.09" W

Note – Location 1 is along the rail tracks that lie south of 9th Avenue SE. The location lies about 1 block south of the intersection of 9th Avenue SE and 4th Street SE. Location 2 is along the rail tracks that lie south of 9th Avenue SW. The location lies about 1 block south of the intersection of 9th Avenue SW and 11th Street SW, along the rail tracks that run through downtown Calgary.


### 3.2 Scenario 2: derailment of a rail car containing chlorine (UN 1017, Class 2)

Rail car (model ERG ID 1017) which can hold up to 25,700 US gallons of liquefied chlorine is only ½ full. It is assumed that the derailment caused 10,000 kg of chlorine to be expelled into the atmosphere in the form of vapor/aerosol droplets. This material was "flashed" to the atmosphere over a short time of 100 s, at a release rate of 100 kg/s over this period of time. In addition, 5,000 kg of liquid chlorine was spilled on the ground as a result of the derailment. The liquid pool of chlorine is assumed to be evaporating from the ground surface at a constant rate of 2.78 kg/s over

a period of 30 minutes, at which time all chlorine in the liquid pool would have evaporated. Of course, there is still quite a bit of liquid chlorine that remains inside the rail car that will need to be cleaned up by the first responders.

**Location 1:** 51 deg, 02', 37.12" N, 114 deg, 03', 11.89" W
**Location 2:** 51 deg, 02', 41.07" N, 114 deg, 05', 14.09" W

Locations 1 and 2 are the same as those in Scenario 1.

For the simulations of Scenarios 1 and 2 above, several wind directions, including 45°, 90°, 135°, 225°, 270° and 315° are chosen that will carry the material into the downtown area of Calgary (where all the tall office towers are).

### 3.3    Scenario 3: van containing two drums of an unknown chemical agent

This scenario corresponds to a volume of about 0.38 m³. Terrorists have planted explosives in the van, and when the explosive incident occurs, it is assumed about a certain quantity of the chemical agent is destroyed in the explosive event. A specified amount of the chemical agent is released instantaneously as a result of the explosion in the form of vapor/aerosol droplets, and the remaining amount of liquid chemical agent spilled on the ground. The material evaporates from the ground surface at a constant rate of over a period of time. The actual quantities released are not reported here. They are available in a separate confidential document (private communication Yee, 2012).

The location of the van is with a block or two of the site of the derailment, and 9 possible locations are chosen as follows:

Relative to "accident" at **Location 1**, the following 4 locations are used in our simulations, in which only the southeast (or 135°) wind direction is considered:

1. 51 deg, 02', 39.18" N, 114 deg, 03', 17.20" W (referred to as L3-1)
2. 51 deg, 02', 38.62" N, 114 deg, 03', 20.18" W (referred to as L3-2)
3. 51 deg, 02', 35.87" N, 114 deg, 03', 16.91" W (referred to as L3-3)
4. 51 deg, 02', 35.81" N, 114 deg, 03', 19.56" W (referred to as L3-4)

Relative to "accident" at **Location 2**, the following 5 locations are used in our simulations, in which only the southwest (or 225°) wind direction is considered:

1. 51 deg, 02', 41.46" N, 114 deg, 05', 21.06" W (referred to as L4-1)
2. 51 deg, 02', 41.30" N, 114 deg, 05', 17.71" W (referred to as L4-2)
3. 51 deg, 02', 40.57" N, 114 deg, 05', 20.43" W (referred to as L4-3)
4. 51 deg, 02', 40.50" N, 114 deg, 05', 18.24" W (referred to as L4-4)
5. 51 deg, 02', 40.96" N, 114 deg, 05', 19.48" W [referred as L4-LC (level crossing plume point)].

# 4. RESULTS AND DISCUSSION FOR DIFFERENT SCENARIOS

The modeling (outer) domain with the extent of 6,400 m × 4,200 m × 830 m in the $x$- (or, W-E), $y$- (or, S-N) and $z$- (or, vertical) directions, respectively, with its southwest (SW) and northeast (NE) corners located at (702,260 m E, 5,656,815 m N) and (708,660 m E, 5,661,015 m N), respectively, in the Universal Transverse Mercator (UTM) coordinate system are shown in Figures 7 and 8. The internal (dimensionless) coordinate system used in urbanSTREAM is normalized by a reference length scale which is chosen in this case to be $L$ = 3,593 m. A proper sub-domain within this modeling region is chosen as the "inner region" in which buildings will be explicitly resolved in the flow simulation. For this example, this rectangular building-aware region of the size of 3,600 m × 2,100 m has its southwest corner at (703,660 m E, 5,657,865 m N) and its northeast corner at (707,260 m E, 5,659,965 m N) in the UTM coordinate system. In the portion of the solution domain lying outside the building-aware (inner) region, all buildings are treated as *virtual* and their effects on the flow are modeled using a distributed drag force representation in the mean momentum equations [see, e.g., Lien & Yee (2004, 2005), Lien et al. (2005)].

A building database in the form of an Arc View Shapefile for the City of Calgary is initially available from Environment Canada. However, it was identified in the early stage of the project that a few key buildings, such as the Bow Building (see Figure 9), was missing in the database. A new building database was later on provided by 3DInternet Inc. and used for the rest of our CFD simulations. These Shapefiles were used in urbanGRID to generate automatically a grid mesh over the modeling region as shown in Figure 10. Then, the simulation was carried out in a 3-D Cartesian framework, and curved surfaces on buildings or planar building surfaces that are not aligned with the grid lines are approximated by stepwise surfaces. A mesh of 498×336×65 grid lines in the $x$-, $y$-, and $z$-directions, respectively, was used to accommodate all the necessary geometrical details. The inner building-aware region was covered with a fine mesh of 450×300×65 grid lines to better approximate the building features in this region. The grid arrangement adopted here is shown on the $x$-$y$ plane in Figure 8. Hence, the fine grid used in the building-aware region contains 8,775,000 nodes, whereas the entire computational domain was covered with a mesh of 10,876,320 nodes. The grid lines were preferentially concentrated near the solid surfaces (ground, building rooftops and walls) where the gradients in the flow properties are expected to be the greatest, and the spacings between the grid lines were gently stretched with an increasing distance from the solid surfaces.

The flow field in the computational domain was computed using urbanSTREAM in a standalone mode, and the inflow condition for a given wind direction was described in Section 2.2. The flow simulation in the computational domain was carried out in the steady RANS mode assuming there was no change in the mean speed or mean direction of the flow within the 45 minutes simulation time period. The effects of the buildings on the flow field outside the building-aware region (viz., in the "virtual building" region) were represented by a distributed drag force approximation in the mean momentum equation given below:

$$\frac{\partial \bar{u}_i}{\partial t} + \frac{\partial \bar{u}_j \bar{u}_i}{\partial x_j} = -\frac{\partial \bar{p}}{\partial x_i} + v \frac{\partial^2 \bar{u}_i}{\partial x_j^2} - \frac{\partial}{\partial x_j}\left(\overline{u_i' u_j'}\right) - 2\varepsilon_{ijk}\Omega_j \bar{u}_k + \bar{f}_{d,i} \qquad (32)$$

where $\bar{f}_{d,i}$ can be derived and approximated as follows (Lien et al., 2005)

$$\bar{f}_{d,i} = -C_d \hat{A} \left[ \left( Q + \frac{5}{3}\frac{k}{Q} \right) \bar{u}_i - v_t \left( \frac{\partial \bar{u}_i}{\partial x_j} + \frac{\partial \bar{u}_j}{\partial x_i} \right) \frac{\bar{u}_j}{Q} \right] \qquad (33)$$

with a normalized drag coefficient of $C_d = 100$. The specification of this value is based on our earlier calculations for the IOP9 test problem in comparison with the experimental data [see, e.g., Lien et al (2008)]. In equation (33), $\hat{A}$ is the frontal area density (frontal area of buildings exposed to the wind per unit volume) and $Q = |\bar{u}_i|$ is the magnitude of the spatially-averaged time-mean wind speed. A modified $k - \varepsilon$ model consistent with equations (32)-(33) can be found in Lien et al. (2005). Sample results at the wind directions of 135° and 225° within and in the building-resolved regions of the city are shown in Figures 11 and 12 to illustrate the complexity of streamline patterns and associated velocity fields. Most results presented in Section 4 are obtained with the parallel version of urbanSTREAM (or urbanSTREAM-P) running on SHARCNET using 16 nodes unless stated otherwise.

### 4.1 Scenario 1: derailment of a rail car containing methanol

In Scenario 1, the amount of methanol in the rail car is 34,500 gal×(3/4) [3/4 full]=25,875 gal, in which only 80% of methanol is left [20% of the methanol is destroyed]; i.e., only 25,875 gal ×4/5 =20,700 gal (=78.35 m³) of methanol is left. Of the remaining methanol not destroyed by the fire, we can split the dispersion processes into two parts:

1. "Instantaneous puff release" ("puff release" or R2 release): ½ of this volume [i.e., 20,700×1/2=10,350 gal (or 39.18 m³)] was "flashed" to the atmosphere in form of vapor/aerosol droplets. The density of methanol at standard temperature and temperature (STP) condition is about 791 kg/ m³. So 39.18×791=30,991 kg ≈ 30,000 kg of methanol, which is treated as a neutrally buoyant (or passive) gas in our simulations, was "flashed" to the atmosphere during the first time step: $\Delta t = 10$ sec.
2. "Continuous release" (or R1 release): another ½ of this volume "boiled" off by the fire for about 30 min at a constant emission rate of 30,000/30=1000 kg/min=16.667 kg/s.

Since both releases above are governed by the *linear* advection-diffusion equation for concentration of methanol with a given velocity field, the superposition principle applies. Therefore, simulations for continuous and puff releases are done separately, and the resulting concentration fields to be shown later are the solutions obtained by combining both releases together.

Sample streamline patterns superimposed with iso-surfaces of concentration at 225° wind direction are shown in Figures 13 (front view) and 14 (rear view), respectively, to illustrate the complexity of flow and concentration fields in the wake region of buildings.

15

Figures 15 to 20 are contours of concentration on a logarithmic scale for the source at Location 1 (51 deg, 02', 37.12" N, 114 deg, 03', 11.89" W) at $t = 5$ and 30 min for the wind direction of 45°, 90° and 135°, respectively. For the source at Location 2 (51 deg, 02', 41.07" N, 114 deg, 05', 14.09" W), similar contours of concentration are given in Figures 21 to 26 at $t = 5$ and 30 min for the wind direction of 225°, 270° and 315°. In these figures, iso-surfaces of $\log_{10}(C) = -2.2, -3.3, -4.4$, where the unit of C is $kg/m^3$, are shown, and $\log_{10}(C) < 12$ are omitted because they are insignificant for practical applications.

Let us consider, e.g., Figures 15 and 16 at $t = 5$ and 30 min for an incident wind direction of 45°. It is clearly seen that both R1 and R2 releases co-exist in Figure 15 in terms of $\log_{10}(C)=-4.4$ iso-surface. However, at $t = 30$ the "puff" (associated with the R2 release) already leaves the solution domain, and only iso-surfaces for R1 (continuous) release are present in Figure 16. Similar comments apply to the figures at the other wind directions (i.e., Figures 17 to 20 with a source at Location 1, and Figures 21 to 26 with a source at Location 2).

Before discussing results for Scenario 2, we repeat the calculations for Scenario 1 except replacing methanol by liquefied chlorine, and using the heavy-gas model described in Section 2.3 to simulate dispersion of chlorine with the source at Location 1 at the wind direction of 135°.

Let us first introduce the following dimensionless groups:

$$\hat{x}_i = \frac{x_i}{L}, \hat{t} = \frac{tU}{L}, \hat{u}_i = \frac{\overline{u}_i}{U}, \hat{p}_i = \frac{\overline{p}_i}{\rho_0 U^2}, \overline{\hat{u}_i'\hat{u}_j'} = \frac{\overline{u_i'u_j'}}{U^2}, \hat{c} = \frac{c}{c_s}, \hat{v}_t = \frac{v_t}{UL} \qquad (34)$$

where the reference length $L = 3{,}593$ m, and the reference velocity $U = 5.556$ m/s in the present calculations. Equation (14) in dimensionless form can be written as

$$\frac{\partial}{\partial \hat{t}}(\hat{u}_i) + \frac{\partial}{\partial \hat{x}_j}(\hat{u}_j \hat{u}_i) = -\frac{\partial \hat{p}}{\partial \hat{x}_i} + \frac{\partial}{\partial \hat{x}_j}\left(\frac{1}{Re}\frac{\partial \hat{u}_i}{\partial \hat{x}_j}\right) - \frac{\partial}{\partial \hat{x}_j}\left(\overline{\hat{u}_i'\hat{u}_j'}\right) + \frac{L}{U^2}\alpha \hat{c} g_i \qquad (35)$$

where $Re = \dfrac{\rho_0 U L}{\mu}$, and

$$\alpha = 1 - \frac{\rho_0}{\rho_g} = 1 - \frac{M_0}{M_g} \qquad (36)$$

In equation (36), $M_0 = 28.97$ kg/kmol and $M_g = 70.91$ kg/kmol are the molecular weights for air and chlorine, respectively. Similarly, equation (15) combined with equation (28) can be non-dimensionalized as

$$\frac{\partial}{\partial \hat{t}}(\hat{c}) + \frac{\partial}{\partial \hat{x}_j}(\hat{u}_j \hat{c}) = \frac{\partial}{\partial \hat{x}_j}\left(\frac{\hat{v}_t}{\sigma_c}\frac{\partial \hat{c}}{\partial \hat{x}_j}\right) + \left(\frac{L}{U c_s}\right)\dot{Q}\delta(\vec{x} - \vec{x}_s) \qquad (37)$$

where $\dot{Q}$ in kg/s is the source strength and $\vec{x}_s$ is the source location. Note that the source term in equation (37) was not in equation (15), and the unit for $\delta(\vec{x}-\vec{x}_s)$ is m$^{-3}$. To be consistent with the Thorney Island test problem, $\sigma_c = 0.63$ is chosen here, which is the turbulent Schmidt number. Also, the molecular diffusion in equation (37) is ignored in order to be compatible with the standard (or high-Re) $k-\varepsilon$ model adopted in the present study. Integrating the last term of equation (37) over a (dimensionless) finite volume containing the source on the ground gives us

$$\int\left(\frac{L}{Uc_s}\right)\dot{Q}\delta(\vec{x}-\vec{x}_s)d\hat{V} = \frac{\dot{Q}}{c_s L^2 U} \tag{38}$$

where $\dot{Q} = 16.667$ kg/s. $c_s$ in equations (34) and (38) is chosen to be 1 kg/m$^3$ for simplicity. In the following, two approaches will be introduced into urbanEU to model the (effect of) source term: one through $\dot{Q}$ and the other through the concentration boundary condition on the ground at $\vec{x} = \vec{x}_s$.

### 4.1.1 Q-approach

In the "Q-approach", $\dfrac{\dot{Q}}{c_s L^2 U}$ in urbanEU is turned on when $0 \le t \le 30$ min. The simulation starts with the use of urbanSTREAM to obtain a *quasi-steady* state velocity and turbulence field for a constant-density (incompressible) flow (viz., the solution converges at around 10 iterations per time step). With this as the initial condition, urbanEU is then coupled to urbanSTREAM to restart the calculations for another 270 time steps at $\Delta t = 10$ sec.

### 4.1.2 W$_{jet}$-approach

To further validate the implementation of heavy-gas modeling capability in urbanEU, an alternative approach - referred to as the "W$_{jet}$ approach" is proposed here. Firstly, we set $\dfrac{\dot{Q}}{c_s L^2 U} = 0$. At the source location (i.e., at $\vec{x} = \vec{x}_s$) on the ground, we set

1. $\hat{c} = 1$ (or $c = c_s$),

2. $\hat{w} = \dfrac{\dot{Q}}{c_s U A_s}$,

where $\hat{w}$ is the dimensionless vertical component of the (jet) velocity at the source location, and $A_s$ is the source surface area.

Sample results showing iso-surfaces of concentration of log(C) = -5, -7 and -10 at $t = 10$ min obtained with both the Q- and W$_{jet}$ approaches are shown in Figures 27 and 28. It is observed that both results are virtually identical.

We also compare contours of log(C) superimposed with the velocity vector field near the source location at $t$ = 10 min obtained with the dense-gas model (using the Q-approach) and the passive-gas model, which are shown in Figures 29 and 30, respectively. Interestingly, both results are quite similar. It is noted here that in the case of the passive-gas approach, urbanEU is decoupled from urbanSTREAM, and only the concentration equation is required to be solved. In contrast, if the dense-gas model is employed, urbanEU and urbanSTREAM are strongly coupled together, and typically 175 "outer" iterations per time step is required to reach convergence. In terms of CPU time consumption, the passive-gas approach is approximately 400 times faster than the dense-gas approach (whether using either the Q-approach or $W_{jet}$ approach). Since the results shown in Figures 29 and 30 seem to suggest that there is no major difference using either the dense-gas or the passive-gas approach, only the passive-gas approach will be considered for the rest of the scenarios to save computing resources as there are many cases that need to be computed for the present project.

## 4.2    Scenario 2: derailment of a rail car containing chlorine

In Scenario 2, the amount liquefied chlorine of in the rail car (model ERG ID 1017) is 25,700 gal×(1/2) [1/2 full]=12,850 gal ≈ 76,000 kg based on the density of the liquefied chlorine being 1562.5 kg/m$^3$ (at 1.013 bar at boiling point). It is assumed that the derailment caused 10,000 kg of chlorine to be expelled into the atmosphere in the form of vapor/aerosol droplets over a short time of 100 sec, at a release rate of 10,000/10=100 kg/s over this period of time, which will be considered as "instantaneous release" (or R2 release) in our simulations.

In addition, 5,000 kg of liquid chlorine that was spilled on the ground is assumed to be evaporating from the ground surface over a period of 30 minutes (or 1,800 sec) at a constant rate of 5,000/1,800 =2.78 kg/s, at which time all chlorine in the liquid pool would have evaporated, and treated as "continuous release" (or R1 release) in our simulations. In both releases, chlorine gas is considered as a passive gas to save computing resources.

Figures 31 to 36 are contours of concentration on a logarithmic scale for the source at Location 1 (51 deg, 02', 37.12" N, 114 deg, 03', 11.89" W) at $t$ = 5 and 30 min for the wind direction of 45°, 90° and 135°. For the source at Location 2 (51 deg, 02', 41.07" N, 114 deg, 05', 14.09" W), similar contours of concentration are given in Figures 37 to 42 at $t$ = 5 and 30 min for the wind direction of 225°, 270° and 315°. In these figures, iso-surfaces of $\log_{10}(C)$ = -2.2, -3.3, -4.4 are shown, and $\log_{10}(C)$ < 12 are omitted for the same reason as in Scenario 1.

Note that the 3 iso-surfaces in Figures 15 to 26 for Scenario 1, and in Figures 31 to 42 for Scenario 2 are chosen at the same values of $\log_{10}(C)$ = -2.2, -3.3, -4.4 for comparison purposes later. Let us compare R1 (continuous) and R2 (instantaneous or puff) releases in Scenarios 1 and 2 based on the following Table:

|  | R1 release | R2 release |
|---|---|---|
| **Scenario 1** | 30,000 kg over 30 min | 30,000 kg over 10 sec |
| **Scenario 2** | 5,000 kg over 30 min | 10,000 kg over 100 sec |

Similar to what we observe in the results for Scenario 1, iso-surfaces of $\log_{10}(C)$ for both R1 and R2 releases of Scenario 2 co-exist at $t = 5$ min for all wind directions with a source at Location 1 as shown in Figures 31, 33 and 35, and with a source at Location 2 as shown in Figures 37, 39 and 41. In contrast, at $t = 30$ min the "puff" (or R2 release) has been convected out of the solution domain, and only iso-surfaces associated with the R1 release can be seen in Figures 32, 34, 36, 38, 40 and 42. Also, at $t = 30$ min for a given wind direction, say 135°, the volume corresponding to $\log_{10}(C) = -4.4$ for Scenario 2 (shown in Figure 36) is smaller than that for Scenario 1 (shown in Figure 20). This is because the amount of R1 release (30,000 kg) for Scenario 1 is 6 times larger than that (5,000 kg) for Scenario 2.

## 4.3 Scenario 3: van containing two drums of an unknown chemical agent

In Scenario 3, it is assumed that a quantity of an unknown chemical agent is released instantaneously as a result of the explosion in the form of vapor/aerosol droplets. This is treated as "instantaneous puff release" during the first time step of $\Delta t = 10$ sec.

In addition, as a result of the explosion in the form of vapor/aerosol droplets, and a certain quantity of the liquid agent is spilled on the ground. The material evaporates from the ground surface at a constant rate over a period of 30 minutes.

Four source locations close to "Location 1" (at 51 deg, 02', 37.12" N, 114 deg, 03', 11.89" W) for both Scenarios 1 and 2, referred to as L3-1, L3-2, L3-3 and L3-4 in Section 3.3, are shown in Figures 43, 47, 51 and 55 on a google map. The corresponding top (or $x$-$y$) view of contours of $\log_{10}(C)$, where C is concentration in arbitrary units, are given in Figures 44, 48, 52 and 56 at a wind direction of 135° (or southeast wind). Figures 45 and 46, Figures 49 and 50, Figures 53 and 54, and Figures 57 and 58 are contours of $\log_{10}(C)$ in conjunction with 3 iso-surfaces of $\log_{10}(C)=-5, -6$ and $-7$ (with C in arbitrary units) at $t = 5$ and 15 min for sources at L3-1, L3-2, L3-3 and L3-4, respectively.

Similarly, five source locations close to "Location 2" (at 51 deg, 02', 41.07" N, 114 deg, 05', 14.09" W) for Scenarios 1 and 2, referred to as L4-1, L4-2, L4-3, L4-4 and L4-LC in Section 3.3, are shown in Figures 59, 63, 67, 71 and 75 on a google map. The corresponding top (or $x$-$y$) view of contours of $\log_{10}(C)$ are given in Figures 60, 64, 68, 72 and 76 at a wind direction of 225° (or southwest wind). Figures 61 and 62, Figures 65 and 66, Figures 69 and 70, Figures 73 and 74, and Figures 77 and 78 show contours of $\log_{10}(C)$ in conjunction with 3 iso-surfaces of $\log_{10}(C)=-5, -6$ and $-7$ at $t = 5$ and 15 min for sources at L4-1, L4-2, L4-3, L4-4 and L4-LC, respectively.

As seen from Figures 44, 48, 52 and 56 for sources located close to Location 1 (at 51 deg, 02', 37.12" N, 114 deg, 03', 11.89" W) for a southeast wind (i.e., at a wind direction of 135°), the "domain of influence" [or spread of the iso-surfaces of $\log_{10}(C)$] downstream of the source is mainly determined by the wind direction and source location. However, the concentration fields near sources at L3-1 and L3-4 (see Figures 44 and 56) are strongly influenced by the presence of buildings immediately upstream of the sources. Let us examine contours and iso-surfaces of $\log_{10}(C)$ at $t = 5$ and 15 min shown in Figures 45 and 46 at L3-1 source location. It is seen that both R1 and R2 releases still co-exist in the solution domain even at $t = 15$ min. However, contours projected on the $y$-$z$ and $x$-$z$ planes suggest that the "puff" is moving (and decaying) in

the southeast direction, which is consistent with the wind direction of 135°. Similar observation applies to L3-2, L3-3 and L3-4 source locations.

For sources located close to Location 2 (51 deg, 02', 41.07" N, 114 deg, 05', 14.09" W) at a wind direction of 225°, the top view of the overall shape of the downstream plume in terms of $\log_{10}(C)$=-7 is quite similar for all five source locations examined here (see Figures 60, 64, 68, 72 and 76). This suggests that as the size of the plume grows to the extent that its length scale is larger than the average building height, the shape of the plume is hardly affected by the detailed configuration (i.e., shape, size and orientation) of the buildings underneath. The basic idea of the drag-force model described by equations (32) and (33) is essentially based on the above observation, which hypothesizes that the effects of buildings only influence the *large scale* of the wind field and concentration fields [after volume-averaging of the RANS equation (see, e.g., Lien et al., 2005)]. Note that all buildings in the "inner region" are explicitly resolved here. Also, contours projected on the *y-z* and *x-z* planes in Figures 62, 66, 70, 74 and 78 at L4-1, L4-2, L4-3, L4-4 and L4-LC source locations suggest that the "puff" is moving (and decaying) in the southwest direction, which is consistent with the wind direction of 225°.

## 4.4 Development of a compact data structure for file transfer

To facilitate the transfer of concentration data over 40 min at the time interval of every 1 sec for $0 \le t \le 1$ min, every 5 sec for 1 min $< t \le 10$ min, and every 10 sec for 10 min $< t \le 40$ min on a grid of the size of $\approx 11$ million nodes, a compact data structure is developed for this project, in which only the concentration values of greater than the cut-off number (chosen to be $10^{-20}$ kg/m$^3$ in the present report) are stored.

### 4.4.1 Data structure and its parallel implementation

In urbanSTREAM-P, a new module: **datatype.f90** is developed and listed below:

```
      MODULE datatype
!>>TYPE
      TYPE OUTPUT_TYPE
      INTEGER :: MX
      INTEGER :: IL, JL, KL
      INTEGER :: IG, JG, KG
      END TYPE OUTPUT_TYPE
!>>TYPE
!>>TYPE
      TYPE OUTPUTC_TYPE
      INTEGER :: I, J, K
      REAL:: C
      END TYPE OUTPUTC_TYPE
!>>TYPE

      TYPE(OUTPUT_TYPE ), allocatable, dimension(:,:) :: OUTPUT
      TYPE(OUTPUTC_TYPE), allocatable, dimension(:  ) :: OUTPUTC
      INTEGER :: ndata
      REAL, PARAMETER :: C_cutoff = 1.E-20
      END MODULE datatype
```

in which **(IL,JL,KL)** and **(IG,JG,KG)** represent (I,J,K) indices in the local and global coordinate systems, respectively. Note that the local indices **(IL,JL,KL)** are the indices on a partition (or sub-domain) of the solution domain designated by its node (or CPU) number: **node** when the MPI library is used for message passing on a parallel Linux cluster in SHARCNET. The global indices **(IG,JG,KG)** correspond to the indices on a single grid before grid partitioning is done by the pre-processor: **urbanPartitioning.f90**.

A header file: **compact.h** listed below using the data type **output(:,:)** and **outputc(:)** defined above is included in the main program of urbanSTREAM-P:

```
      ndata=0
      DO K=NKBEG(NB)+2,NKEND(NB)-2
      DO J=NJBEG(NB)+2,NJEND(NB)-2
      DO I=NIBEG(NB)+2,NIEND(NB)-2
      C_dimensional=abs(C(I,J,K))*C_SOURCE              ![kg/m^3]
      IF(C_dimensional<C_cutoff) CYCLE
      ndata=ndata+1
      END DO
      END DO
      END DO
      allocate(outputc(ndata))
!
      ijk_max=
     1 (NIEND(NB)-NIBEG(NB)-3)
     1*(NJEND(NB)-NJBEG(NB)-3)
     1*(NKEND(NB)-NKBEG(NB)-3)
!
      n =0
      nn=0
      DO K=NKBEG(NB)+2,NKEND(NB)-2
      DO J=NJBEG(NB)+2,NJEND(NB)-2
      DO I=NIBEG(NB)+2,NIEND(NB)-2
      nn=nn+1
      C_dimensional=abs(C(I,J,K))*C_SOURCE              ![kg/m^3]
      IF(C_dimensional<C_cutoff) CYCLE
      n=n+1
      outputc(n)%i=output(nn,node+1)%IG
      outputc(n)%j=output(nn,node+1)%JG
      outputc(n)%k=output(nn,node+1)%KG
      outputc(n)%c=C_dimensional
      END DO
      END DO
      END DO
!
      write(30) nint(itime*delt*Tscal)
      write(30) ndata
      if(ndata/=0) then
      write(30)(outputc(n)%i,outputc(n)%j,outputc(n)%k,outputc(n)%c,
     1n=1,ndata)
      end if
!
      deallocate(outputc)
```

Box annotation (pointing to the `ndata=ndata+1` / allocate section):

> compute total number of concentration data where C>C_cutoff is exported to urbanCollect.f90 for post-processing

Note that the info about global indices **(IG,JG,KG)** are provided by the pre-processor: **urbanPartitioning.f90** through the subroutine **geometry.f90** in urbanSTREAM-P shown below:

```
 read(io)n,nnmax
 allocate(output(nnmax,nbloc))
 read(io)((
1output(nn,n)%IL,output(nn,n)%JL,output(nn,n)%KL,
1output(nn,n)%IG,output(nn,n)%JG,output(nn,n)%KG),
1nn=1,nnmax)
```
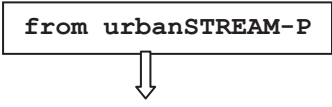
The output of concentration fields obtained with urbanSTREAM-P from each CPU (or **node** in the sample code) is collected by **urbanCollect.f90** to map (or merge) solutions from each partition onto a single mesh of 498×336×65 grid points before post-processing the results using Tecplot. The main part of **urbanCollect.f90** is listed below for illustration purpose:
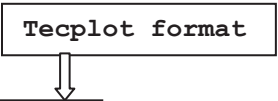
```
      read(30+node) time
      read(30+node) ndata
c
      if(ndata/=0) then                         from urbanSTREAM-P
      allocate(outputc(ndata))
c                                                        ⇩
      read(30+node)(outputc(n)%i,outputc(n)%j,outputc(n)%k,outputc(n)%c,
     1n=1,ndata)
c
      do n=1,ndata
      IG=outputc(n)%i
      JG=outputc(n)%j
      KG=outputc(n)%k
      C(IG,JG,KG)=outputc(n)%c
      end do
c
      deallocate(outputc)
      end if
c
      end do !end of block-loop
!
! tecplot format
!
      i0=(time-mod(time,1000))/1000
      i1=(time-i0*1000-mod(time,100))/100
      i2=(time-i0*1000-i1*100-mod(time-i0*1000-i1*100,10))/10
      i3=time-i0*1000-i1*100-i2*10
!comp
      str3='C'//char(48+i0)//char(48+i1)//char(48+i2)//char(48+i3)    Tecplot format
!comp
                                                                            ⇩
      write(*,*)str3
      open(60,file='comp_'//str3)
      WRITE(60,*)'VARIABLES = "X","Y","Z","C"'
      WRITE(60,*)'ZONE F=POINT, I=',NIM2, ', J=',NJM2, ', K=',NKM2
      DO K=2,NK-1
      DO J=2,NJ-1
      DO I=2,NI-1
      WRITE(60,*)XC(I,J,K),YC(I,J,K),ZC(I,J,K),C(I,J,K)
```

22

```
        END DO
        END DO
        END DO
        close(60)
```

In summary, the compact data structure developed in the present project is added to urbanSTREAM-P, the parallel version of urbanSTREAM, `urbanPartitioning.f90` and `urbanCollect.f90`. As shown in Figure 79, `urbanPartitioning.f90` and `urbanCollect.f90` are pre-processor and post-processor of urbanSTREAM-P interfacing urbanGRID and urbanPOST.

### 4.4.2 Validation and storage efficiency test

Sample iso-surfaces of the concentration field at log(C) = -3, -5 and -8 for a southwest (or 225°) wind direction for Scenario 1 are shown in Figures 80 and 81 at $t = 1,800$ sec, where contours of log(C) below -12 are not shown as they are insignificant for practical applications. As seen from Figure 80 (no compact data structure is used) and Figure 81 (the proposed compact data structure is adopted), the results are essentially identical. The time history of the compression ratio is given in Figure 82. When time is small, say, $t = 60$ sec, the compression ratio is as low as 0.8%. As the time approaches to $t = 1,800$ sec, the compression ratio reaches about 27%.

### 4.4.3 File transfer and dataset naming conventions

In order to transfer (via ftp) the dataset for each scenario at different times up to $t = 40$ min to 3DInternet Inc., a Fortran code: `read_data.f90` was provided to 3DInternet Inc. to reproduce our results generated by Tecplot. The key portion of the code is listed below to convert the concentration data from the compact data structure to the standard `(I,J,K)` array data structure:

```
        do n=1,ndata
        C(output(n)%i,output(n)%j,output(n)%k)=output(n)%c
        end do
```

The complete listing of the Fortran program is given in Appendix A for information only. Sample concentration results obtained from urbanPOST and `read_data.f90`, respectively, are given in Figures 83, and identical results are seen to ensure the validity of the code.

For each scenario with a given source location, two sets of data are provided individually; namely, one for the continuous release and the other for the puff release as explained below. For Scenario 1 discussed in Section 3.1, the release can be split into two parts:

- Release 1 (**R1**): 30,000 kg over 30 min or 1,000 kg/min (=16.667 kg/s) over 30 min at $\Delta t$ = 10 sec, which is considered as "continuous release".
- Release 2 (**R2**): 30,000 kg over one time step: $\Delta t = 10$ sec, which is considered as "instantaneous puff release" or "puff release".

Since the concentration equation is a *linear* PDE (partial-differential equation), with a given velocity field the final solution of the concentration field is obtained by combining R1 and R2

releases together. Iso-surfaces of the concentration field at $\log_{10}(C)=$ -2.2, -3.3 and -4.4 for a source of continuous release, of puff release and of combining continuous and puff releases together at the northwest wind direction are shown in Figures 84, 85 and 86, respectively.

Two zip files are produced for Scenario 1: S1-R1-315.tar.gz and S1-R2-315.tar.gz, where the naming conventions are:

- S1: Scenario 1;
- R1, R2: continuous and puff releases, respectively;
- 315: 315° wind direction.

Similar naming conventions apply to Scenario 2 at 6 other wind directions: 45°, 90°, 135°, 225°, 270° and 315°, except R1, R2 are defined differently as follows:

- Release 1 (**R1**): 2.7778 kg/s over 30 min at $\Delta t = 10$ sec, which is considered as "continuous release".
- Release 2 (**R2**): 10,000 kg over 100 sec (or 10 time steps at $\Delta t = 10$ sec), which is considered as "instantaneous release".

For each release (R1 or R2) in Scenarios 1 and 2 at various wind directions, 270 data files in total at every 10 sec for $0 \leq t \leq 45$ min are generated.

For Scenario 3, concentration results with only one wind direction at 135° are obtained for source locations at L3-1, L3-2, L3-3 and L3-4 defined in Section 3.3. Therefore, datasets named by S3-R1-L3-1.tar.gz and S3-R1-L3-1.tar.gz mean that

- S3: Scenario 3 at southeast (or 135°) wind direction;
- R1, R2: continuous and puff releases, respectively;
- L3-1: source located at L3-1 [or at (51 deg, 02', 39.18" N, 114 deg, 03', 17.20" W)].

Similarly, for source locations at L4-1, L4-2, L4-3, L4-4 and L4-LC defined in Section 3.3, only one wind direction at 225° are considered to generate the concentration field results. Datasets, such as, S3-R1-L4-1.tar.gz and S3-R1-L4-1 mean that

- S3: Scenario 3 at southwest (or 225°) wind direction;
- R1, R2: continuous and puff releases, respectively;
- L4-1: source located at L4-1 [or at (51 deg, 02', 41.46" N, 114 deg, 05', 21.06" W) ].

R1 and R2 above for Scenario 3 are defined as follows:

- Release 1 (**R1**): 50 kg over 30 min or 1.667 kg/min (=0.02778 kg/s) at $\Delta t = 1$ sec, which is considered as "continuous release".
- Release 2 (**R2**): 300 kg over one time step: $\Delta t = 1$ sec, which is considered as "puff release".

In total, 348 data files for each release (R1 or R2) in Scenario 3 at various source locations are generated according to the following frequency:

- every 1 sec for $0 \leq t \leq 1$ min;
- every 5 sec for 1 min $< t \leq 10$ min;
- every 10 sec for 10 min $< t \leq 40$ min.


## 5.   CONCLUSIONS AND RECOMMENDATIONS

In this contract, extensive hazardous plume entities have been computed by coupling urbanSTREAM with urbanEU in order to provide the resulting concentration datasets over a period of about 45 min to the game-based simulation engine developed by 3DInternet Inc. as part of the CRTI project 09-509TD. urbanSTREAM was executed in a standalone mode. In consequence, at the inflow (inlet) boundary of the computational domain a power-law velocity profile described in Section 2.2 was used to define the inflow boundary conditions for the simulations. The new dense-gas model presented in Section 2 and results discussed in Section 4 allow the following conclusions to be drawn, and recommendation for the future work to be made:

1.  The development of a realistic multi-spectrum CBRNE scenario for an actual urban environment (downtown Calgary) involves three sequential events consisting of accidental and deliberate releases of hazardous materials (toxic industrial chemicals and chemical agent) and detonation of an explosive device, which are referred to as Scenarios 1 to 3 in Section 3. There are 42 concentration files (each $\approx$ 10 GB in size) that need to be transferred to 3DInternet Inc. via FileTransfer Protocol (ftp) utility program. Since $C < 10^{-12}$ kg/m$^3$ is insignificant for practical applications, a "compact data structure" described in Section 4.4 is developed to facilitate the transfer of the datasets. For example, the compression ratio of the dataset over a period of 30 min is less than 27% (see Figure 82) when the compact data structure is included in urbanSTREAM-P [parallel version of urbanSTREAM (Yee et al., 2007)] and, its preprocessor and postprocessors: **urban-Partitioning.f90** and **urbanCollect.f90**.

2.  For the dense-gas model, a simple and rigorous derivation for the modeling of the buoyancy term within the framework of the Boussinesq approximation is provided and results obtained with this model has been published in the *International Journal of Greenhouse Gas Control* (Hsieh et al., 2013). The effects of buildings and/or complex topography on the dispersion of dense gas clouds/plumes are studied. It is shown that the model is able to provide fair to good predictions for the Thorney Island test gas, where experimental data is available.

3.  In order to verify the implementation of dense-gas model in urbanEU, two methods, referred to as the "Q-approach" and "$W_{jet}$-appraoch", are attempted here. Preliminary dispersion results obtained with both dense-gas and passive gas models for Scenario 1 in the City of Calgary are fairly comparable. With a pre-computed quasi-steady wind and turbulence fields as the initial condition, the dense-gas model is approximately 400 times

more costly than the passive-gas approach. For the latter, the advection-diffusion equation for the passive scalar (or concentration) is entirely decoupled from the other 6 equations (namely, pressure-correction equations, 3 momentum equations, $k$- and $\varepsilon$- equations for turbulence). In other words, only the *linear* advection-diffusion equation is required to be solved for the passive-gas approach. Therefore, most dispersion results presented in this report are obtained with the passive-gas approach.

4. To further validate the proposed dense-gas model, LES (large eddy simulations) or hybrid RANS/LES, such as DES (Detached Eddy Simulation) [see, e.g., Strelets (2001)], PRNS (Partially Resolved Numerical Simulation) [see, e.g., Shih and Liu (2008), Hsieh et al. (2010)] might be a better approach than the present (U)RANS method. However, application of LES or hybrid RANS/LES to simulate the highly disturbed flow in a cityscape, in which a large portion of buildings is explicitly resolved, can be prohibitively expensive and therefore was not considered in this project.

5. In addition to the Thorney Island field trials, which was conducted from July 1982 to July 1983, more recent dense-gas field experiment, such as the industrial scale pipeline rupture experiments in the European project entitled "CO$_2$PipeHaz" (http://www.co2pipehaz.eu/) [see, also Woolley et al. (2013)], should be considered for future investigation when the data becomes publicly available.

6. In Scenario 2, it was assumed that derailment caused 10,000 kg of chlorine to be expelled into the atmosphere and "flashed" in the form of vapor/aerosol droplets. It is recommended that a (more rigorous) chlorine source term model [see, e.g., Barrett (2009)] be included in urbanEU.

7. Scenario 3 involved the explosive release of an unknown chemical agent. It is recommended that an unconfined vapor cloud explosion source term model [see, e.g., the SEVEX project (Ronday, et al., 1995)] be developed based on WATCFD's recent capability in CFD modeling of various explosion problems [see, e.g., Ji et al. (2010), Xu et al. (2013)] as a potential extension of the present project.

## Appendix A: Fortran Code Listing for read_data.f90

```fortran
      MODULE data
!>>TYPE
      TYPE OUTPUT_TYPE
      INTEGER :: I, J, K
      REAL:: C
      END TYPE OUTPUT_TYPE
!>>TYPE
      END MODULE data

      PROGRAM read_data
!
      USE data
      TYPE(OUTPUT_TYPE), allocatable, dimension(:) :: OUTPUT
      INTEGER :: ndata
!
      real, dimension(:,:,:), ALLOCATABLE:: C
      real, dimension(:,:,:), ALLOCATABLE:: X,Y,Z
      character*80 str
      open(10,file='GRID.dat')
      read(10,*)NI,NJ,NK
!
      ALLOCATE(X(NI,NJ,NK),Y(NI,NJ,NK),Z(NI,NJ,NK))
      ALLOCATE(C(NI,NJ,NK))
!
      read(10,*)(((X(I,J,K),I=1,NI),J=1,NJ),K=1,NK)
      read(10,*)(((Y(I,J,K),I=1,NI),J=1,NJ),K=1,NK)
      read(10,*)(((Z(I,J,K),I=1,NI),J=1,NJ),K=1,NK)
!
      CALL GETARG(1,str)

      WRITE(*,*) 'Input file name:',str
      WRITE(*,*)

      OPEN(UNIT = 11, FILE = TRIM(str), STATUS = 'OLD',  FORM='FORMATTED',
ACTION = 'READ')
      read(11,*) ndata
      allocate(output(ndata))
      read(11,20)(output(n)%i,output(n)%j,output(n)%k,output(n)%c,n=1,ndata)
 20   format(3I5,E15.8)
      close(11)
!
      write(*,*)'number of nozero C>C_cutoff, number of total data, &
compression ratio'
      write(*,*)ndata,(ni)*(nj)*(nk),&
               float(ndata)/float( (ni)*(nj)*(nk) )
      C=0.
      do n=1,ndata
      C(output(n)%i,output(n)%j,output(n)%k)=output(n)%c
      end do
!
! tecplot format
!
      open(60,file='comp_'//str)
      WRITE(60,*)'VARIABLES = "X","Y","Z","C"'
```

```
      WRITE(60,*)'ZONE F=POINT, I=',NI, ', J=',NJ, ', K=',NK
      DO K=1,NK
      DO J=1,NJ
      DO I=1,NI
      WRITE(60,*)X(I,J,K),Y(I,J,K),Z(I,J,K),C(I,J,K)
      END DO
      END DO
      END DO
!
      END PROGRAM read_data
```

## REFERENCES

Allwine, K., Leach, M., Stockham, L., Shinn, J., Hosker, R., Bowers, J., Pace, J. (2004), "Overview of Joint Urban 2003 - an Atmospheric Dispersion Study in Oklahoma City", Symposium on Planning, Nowcasting, and Forecasting in the Urban Zone, American Meteorological Society, Seattle, USA, 11-15 January 2004.

Barrett, A.M. (2009), Mathematically Modelling and Decision Analysis for Terrorism Defence: Assessing Chlorine Truck Attack Consequence and Countermeasure Cost Effectiveness, PhD Thesis, Carnegie Mellon University, USA.

Davies, M.E., Singh, S. (1985), "The Phase II Trials: a Data Set on the Effect of Obstructions", *Journal of Hazardous Materials*, **11**, 301–323.

Durbin, P.A. (1996), "On the $k - \varepsilon$ Stagnation Point Anomaly", *International Journal of Heat and Fluid Flow*, **17**, pp. 89–90.

Ferziger, J.H., Peric, M. (2002), Computational Methods for Fluid Dynamics, Springer-Verlag.

Hsieh, K.J., Lien, F.S., Yee, E. (2010), "Towards a Unified Turbulence Simulation Approach for Wall-Bounded Flows", *Flow, Turbulence and Combustion*, **84**, 193-218.

Hsieh, K.J., Lien, F.S., Yee, E. (2013), "Dense Gas Dispersion of $CO_2$ Released From Carbon Capture and Storage Infrastructure into a Complex Environment", *International Journal of Greenhouse Gas Control*, **17**, 127-139.

Ji, H., Lien, F.S., Yee, E. (2010), "A New Adaptive Mesh Refinement Data Structure with an Application to Detonation", *Journal of Computational Physics*, **229**, 8981-8993.

Lien, F.S. (1992), Computational Modelling of 3D Flow in Complex Ducts and Passages, PhD Thesis, University of Manchester Institute of Science and Technology, UK.

Lien, F.S., Leschziner, M.A. (1994), "Upstream Monotonic Interpolation for Scalar Transport with Application in Complex Turbulent Flows", *International Journal for Numerical Methods in Fluids*, **19**, 527–548.

Lien, F.S., Yee, E. (2004), "Numerical Modelling of the Turbulent Flow Developing Within and Over a 3-D Building Array, Part I: Application of a High-Resolution Reynolds-Averaged Navier-Stokes Approach", *Boundary-Layer Meteorology*, **112**, 427-466.

Lien, F.S., Yee, E. (2005), "Numerical Modelling of the Turbulent Flow Developing Within and Over a 3-D Building Array, Part III: A Distributed Drag Force Approach, Its Implementation and Application", *Boundary-Layer Meteorology*, **114**, 287-313.

Lien, F.S., Yee, E., Wilson, J.D. (2005), "Numerical Modelling of the Turbulent Flow Developing Within and Over a 3-D Building Array, Part II: Mathematical Formulation for a Distributed Drag Force Approach", *Boundary-Layer Meteorology*, **114**, 245-285.

Lien, F.S., Yee, E., Ji, H., Hsieh, K.J. (2008), "Partially Resolved Numerical Simulation and RANS Modeling of Flow and Passive Scalar Transport in an Urban Environment", Special Issue of *Journal of Wind Engineering & Industrial Aerodynamics*, **96**, 1832-1842.

Lien, F.S., Yee, E., Wang, B.C., Ji, H. (2010), "Grand Computational Challenges for Prediction of the Turbulent Wind Flow and Contaminant Transport and Dispersion in the Complex Urban Environment", Atmospheric Turbulence, Meteorological Modeling and Aerodynamics, P.R. Lang and F.S. Lombargo (Eds.), Nova Science Publishers.

Patankar, S.V., Spalding, D.B. (1972), "A Calculation Procedure for Heat, Mass and Momentum Transfer in Three-dimensional Parabolic Flows", *International Journal of Heat and Mass Transfer*, **15**, 1787–1806.

Perdikaris, G.A., Mayinger, F. (1993), "Numerical Simulation of Heavy Gas Cloud Dispersion Within Topographically Complex Terrain", *Journal of Loss Prevention in the Process Industries*, **7**, 391–396.

Pielke, Sr., R.A. (2002), Mesoscale Meteorological Modeling (Second Edition), Academic Press.

Qin, T.X., Guo, Y.C., Lin, W.Y. (2007), "Large Eddy Simulation of Heavy Gas Dispersion Around an Obstacle", Proceedings of the Fifth International Conference on Fluid Mechanics, Shanghai, China.

Rhie, C.M., Chow, W.L. (1983), "Numerical Study of the Turbulent Flow Past an Airfoil with Trailing Edge Separation", *AIAA Journal*, **21**, 1525–1532.

Rodi, W. (1978), Turbulence Models and Their Applications in Hydraulics – A State of the Art Review, University of Karlsruhe SFB 80/T/127.

Ronday F., Everbecq, E., Bourouag, T., Deliège, J.F., Dzisiak, J.P., Delvosalle, C., Levert, J.M., Benjelloun, F., Schayes, Castel-Branco, J. (1995), "Assessment and validation of the SEVEX PROJECT", *International Journal of Environment and Pollution*, **5**, 645-654.

Scargiali, F., Di Rienzo, E., Ciofalo, M., Grisafi, F., Brucato, A. (2005), "Heavy Gas Dispersion Modeling Over a Topographically Complex Mesoscale: A CFD Based Approach", *Process Safety and Environmental Protection*, **83**, 242–256.

Shih, T.H., Liu, N.S. (2008), "Modeling of Internal Reacting Flows and External Static Stall Flows Using RANS and PRNS", *Flow, Turbulence and Combustion*, **81**, 279–299.

Sklavounos, S., Rigas, F. (2004), "Validation of Turbulence Models in Heavy Gas Dispersion Over Obstacles", *Journal of Hazardous Materials*, **108**, 9–20.

Strelets, M. (2001), "Detached Eddy Simulation of Massively Separated Flows", AIAA Paper 2001-0879.

Woolley, R.M., Fairweatherb, M., Wareing, C.J., Falle, S.A.E.G., Proust, C., Hebrard, J., Jamois, D. (2013), "Experimental Measurement and Reynolds-Averaged Navier-Stokes Modeling of the Near-Field Structure of Multi-phase $CO_2$ Jet Releases", *International Journal of Greenhouse Gas Control*, **18**, 139-149.

Worthy, J., Sanderson, V., Rubini, P. (2001), "Comparison of Modified $k-\varepsilon$ Turbulence Models for Buoyant Plumes", *Numerical Heat Transfer*, Part B, **39**, 151–165.

Xu, T., Lien, F.S., Ji, H., Zhang, F. (2013), "Formation of Particle Jetting in a Cylindrical Shock Tube", *Shock Waves*, **23**, 619-634.

Yee, E., Lien, F.S., Ji, H. (2007), "Technical Description of Urban Microscale Modeling System: Component 1 of CRTI Project 02-0093RD", DRDC Suffield TR 2007-067.

**Table 1.** Parameters used for the power-law specification of the vertical profile of the streamwise mean wind velocity for Thorney Island trial numbers 26 and 29 (Phase II).

| Trial number | Wind speed $\bar{u}_0$ (m/s) | Exponent $n$ |
|---|---|---|
| 26 | 1.9 | 0.07 |
| 29 | 5.6 | 0.15 |
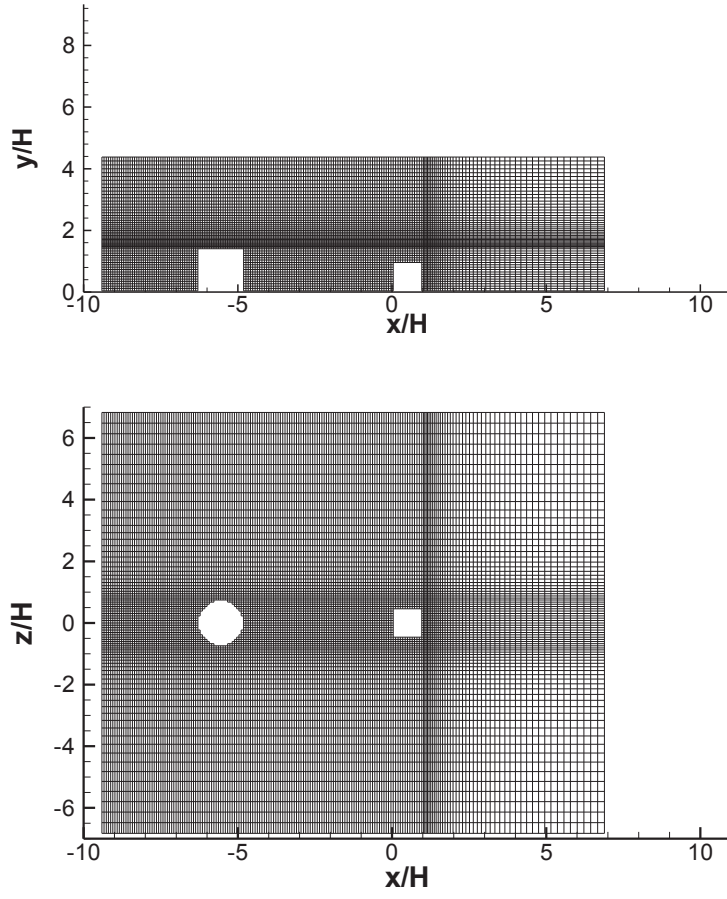
**Figure 1.** A two-dimensional view of the computational mesh for trial number 26 in a vertical *x-y* plane at *z* = 0 (top panel) and in a horizontal *x-z* plane at *y* = 0 (bottom panel). The mesh consists of 189 × 60 × 83 nodes in the streamwise (*x*), vertical (*y*), and spanwise (*z*) directions, respectively.
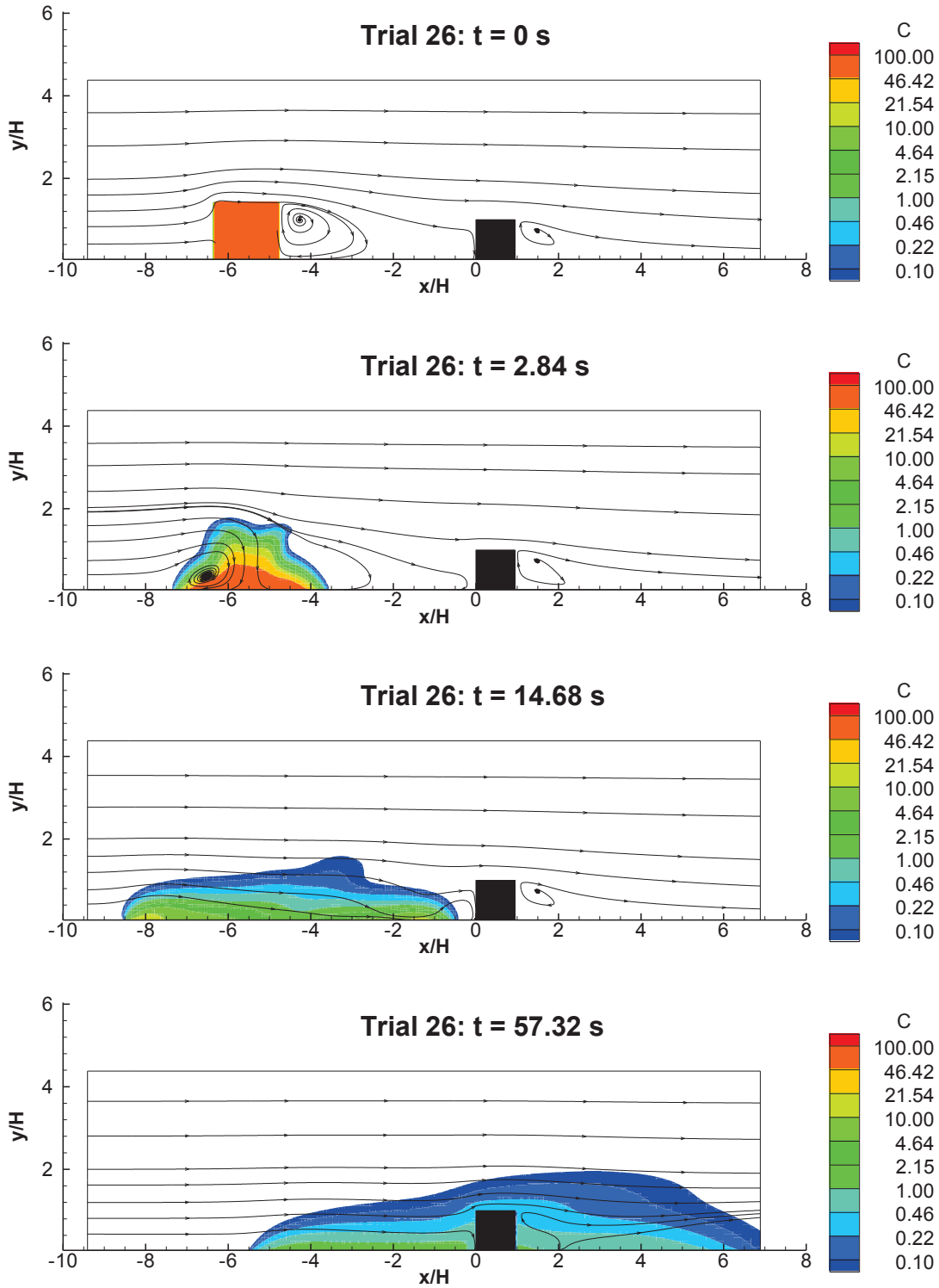
**Figure 2.** Time evolution of mean flow streamlines and contours of mean concentration (% v/v) of the gas cloud in a vertical plane at *z/H* = 0 for trial number 26.
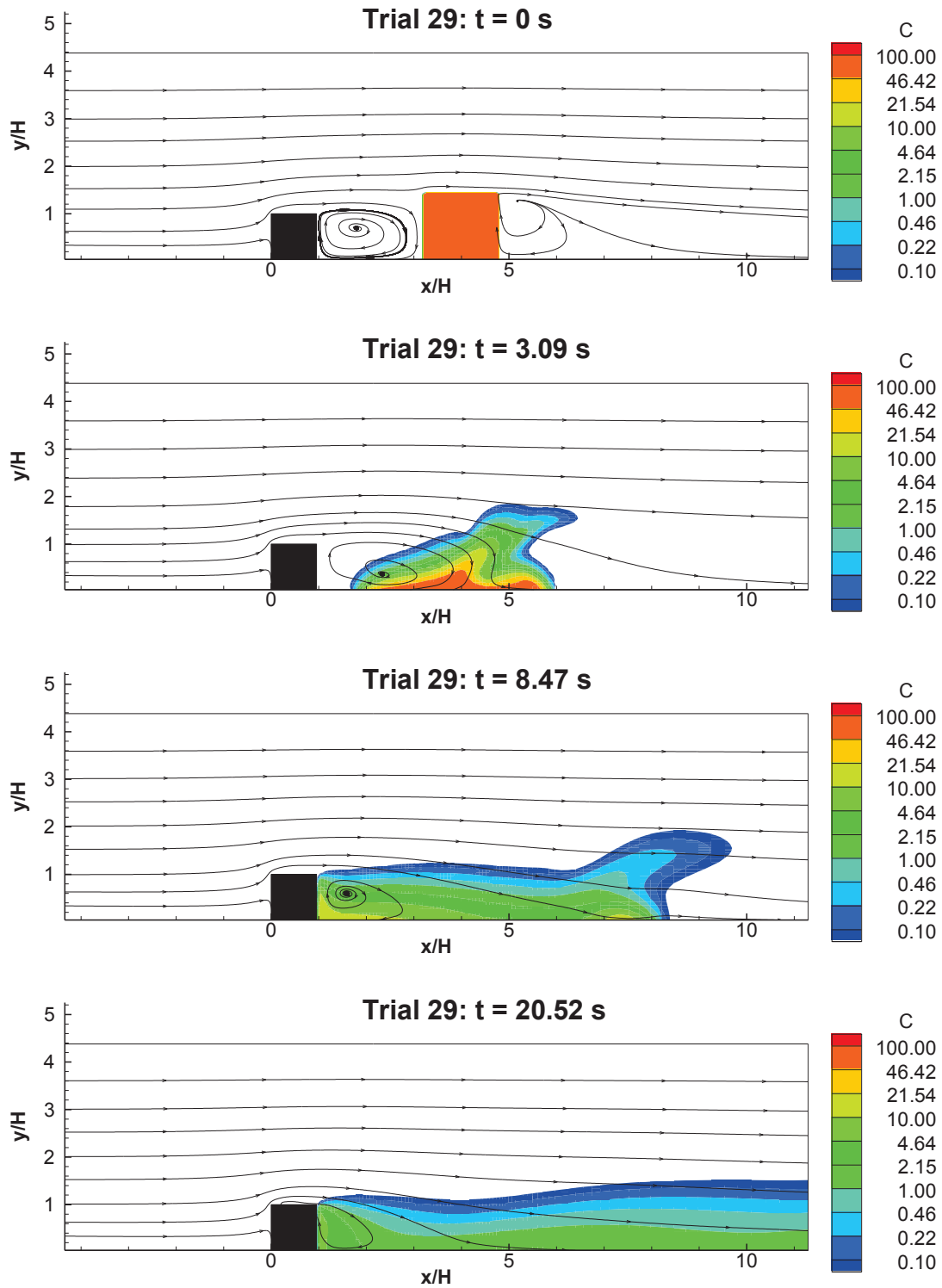
**Figure 3.** Time evolution of mean flow streamlines and contours of mean concentration (% v/v) of the gas cloud in a vertical plane at $z/H = 0$ for trial number 29.
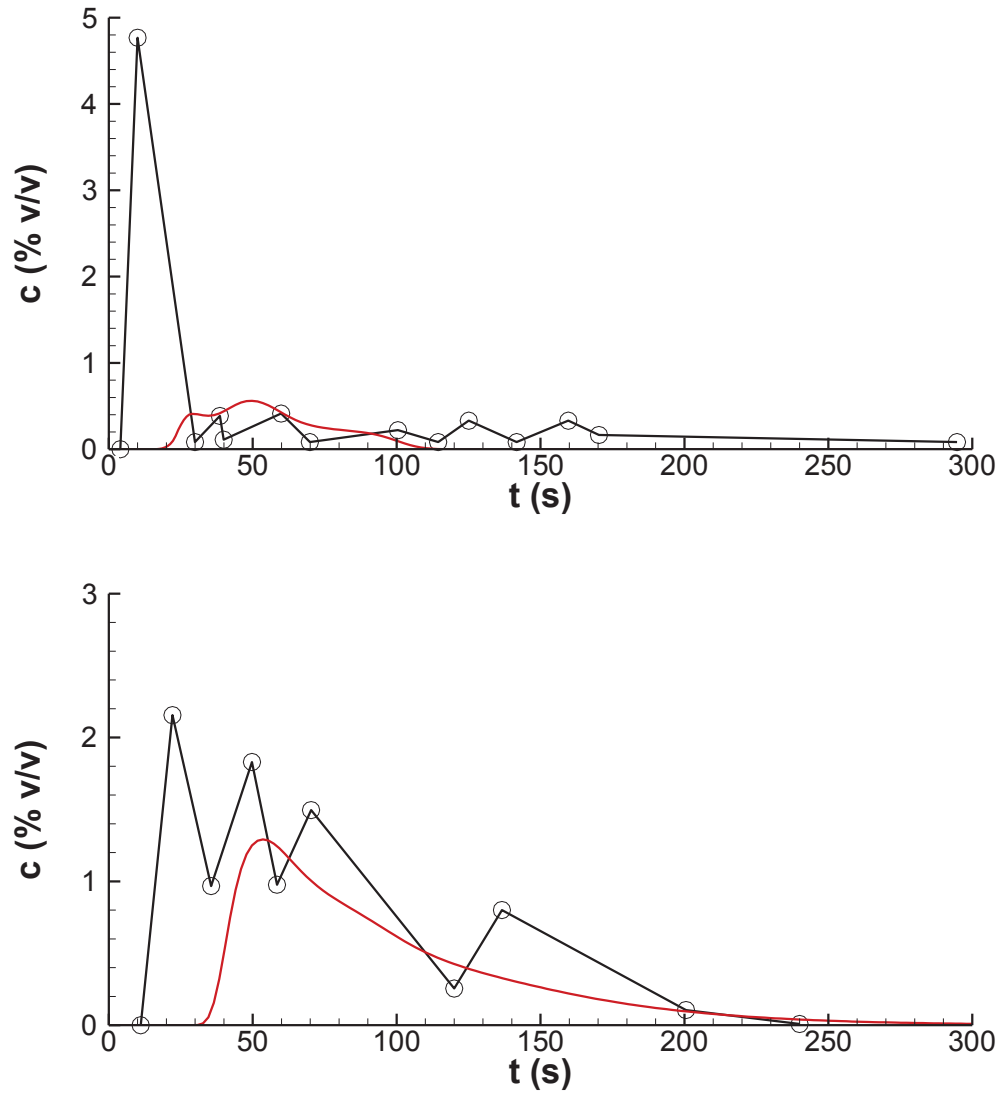
**Figure 4.** Time history of gas concentration on the windward face of the obstacle at a height of 6.4 m (top panel) and on the leeward face of the obstacle at a height of 0.4 m (bottom panel) for trial number 26: (–○–) experimental data from Davies and Singh (1985); (——) simulation.
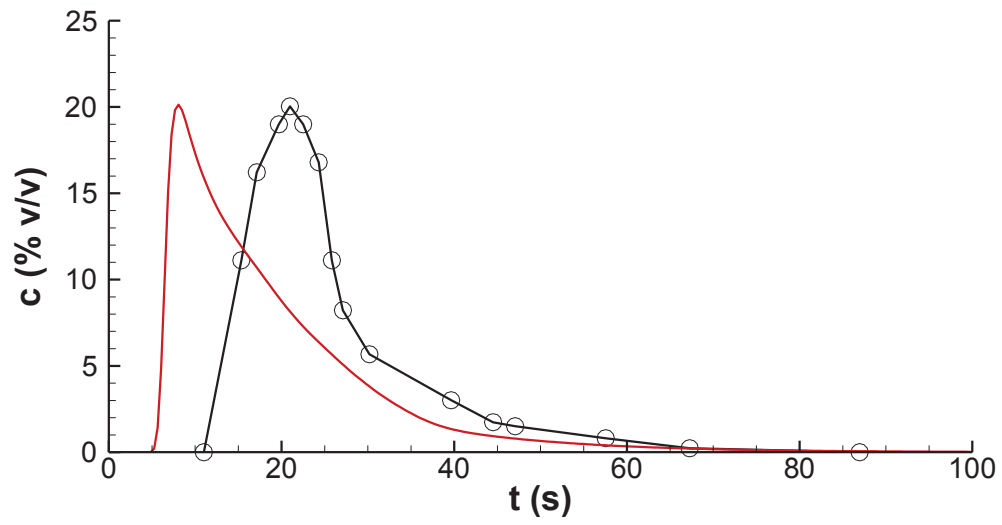
**Figure 5.** Time history of gas concentration on the leeward face of the obstacle at a height of 0.4 m for trial number 29: (–◦–) experimental data from Davies and Singh (1985); (—) simulation.
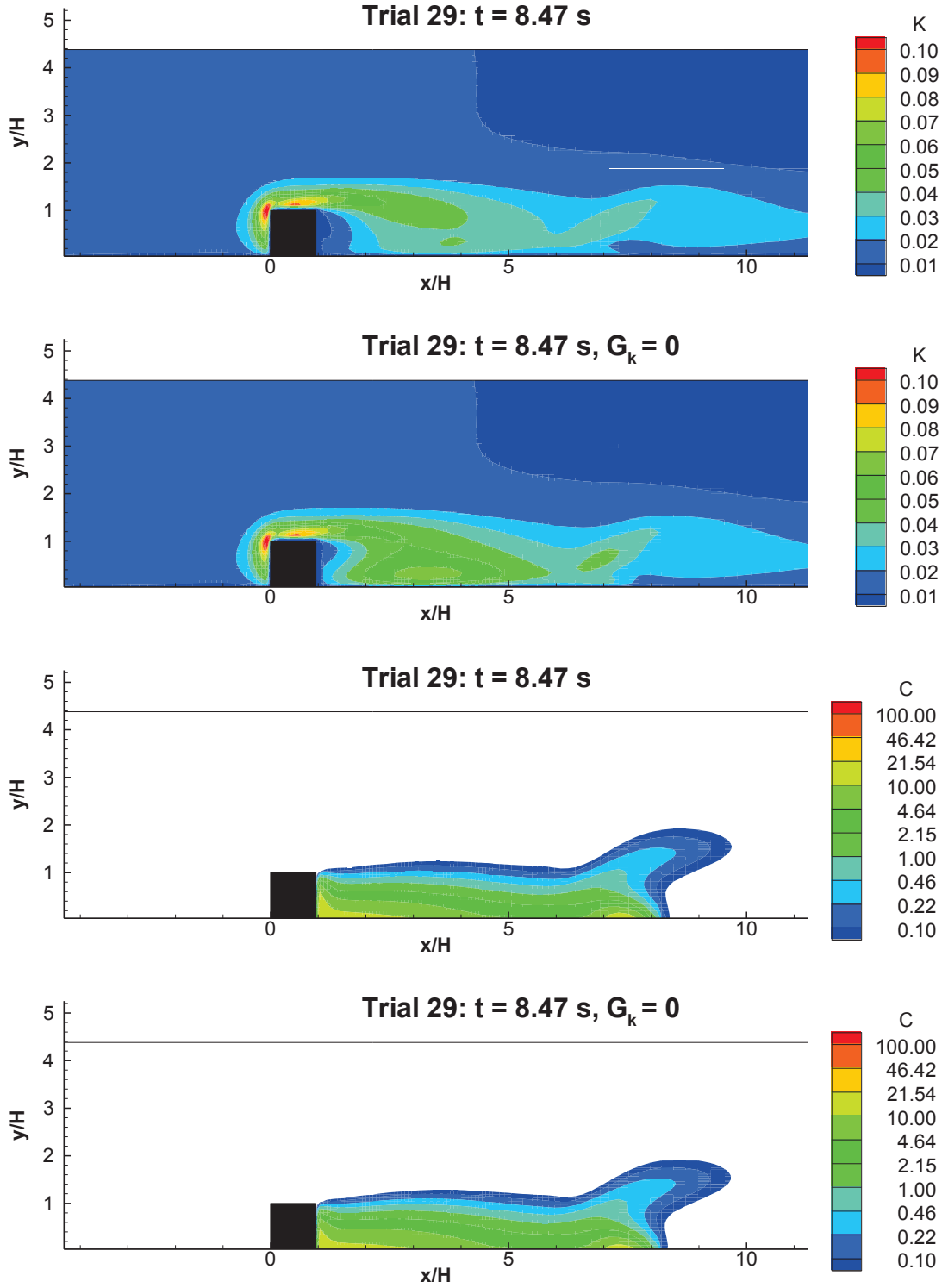
**Figure 6.** Buoyancy production term sensitivity analysis: contours of turbulence kinetic energy (top two panels) and mean concentration (% v/v) in the gas cloud (bottom two panels) in a vertical plane at $z/H = 0$ for trial number 29, with and without inclusion of the $G_k$ term in the turbulence transport equations.
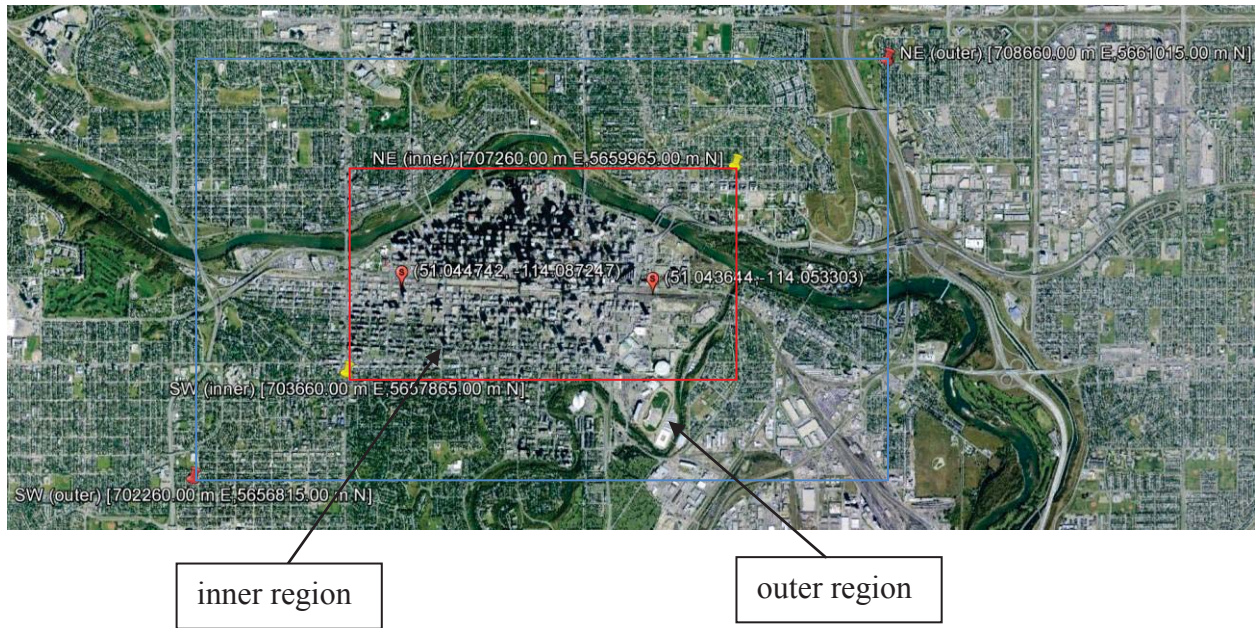
**Figure 7.** Google map showing "inner region" and "outer region" of the computational domain.
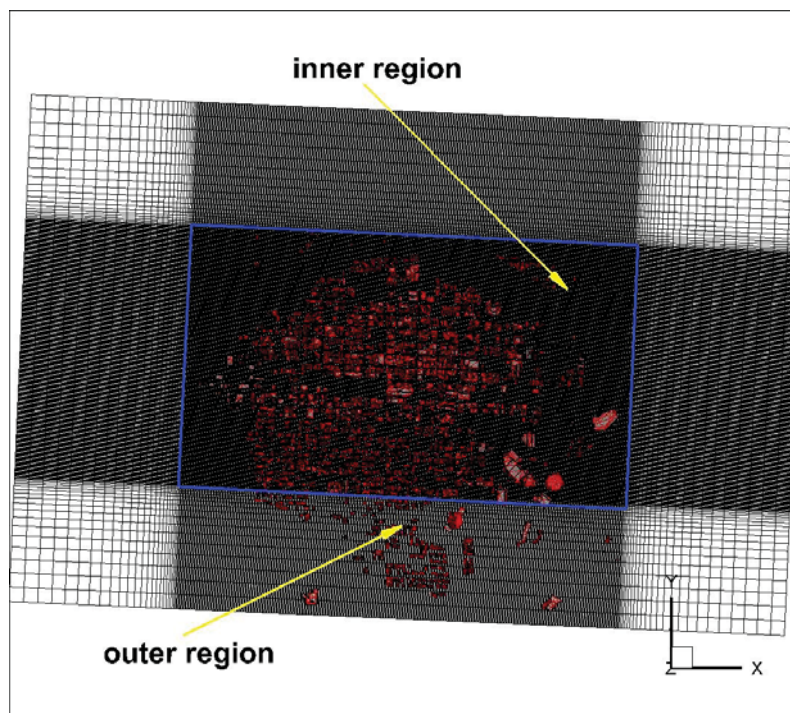


**Figure 8.** Top view of the computational grid consisting of "inner region" and "outer region".
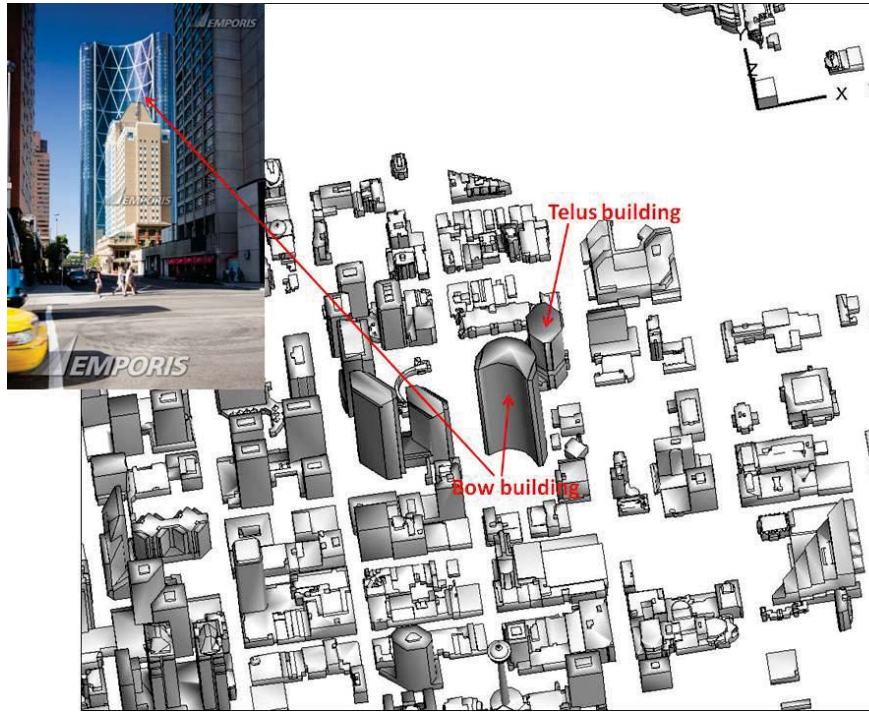
**Figure 9.** New Shapefiles including the Bow Building in the City of Calgary provided by 3DInternet Inc.
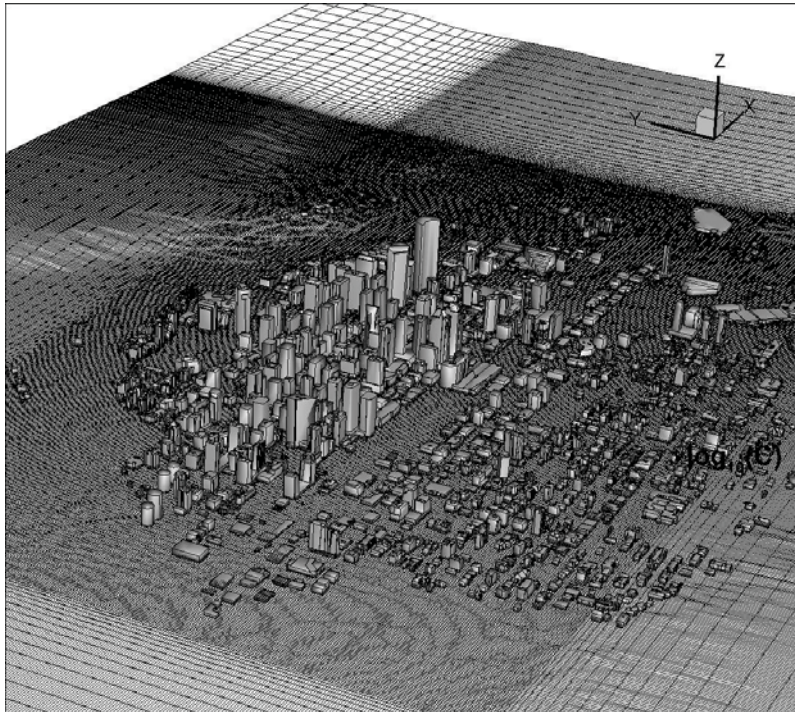


**Figure 10.** 3D view of the computational grid consisting of 498×336×65 nodes in the *x*-, *y*- and *z*-directions, respectively.
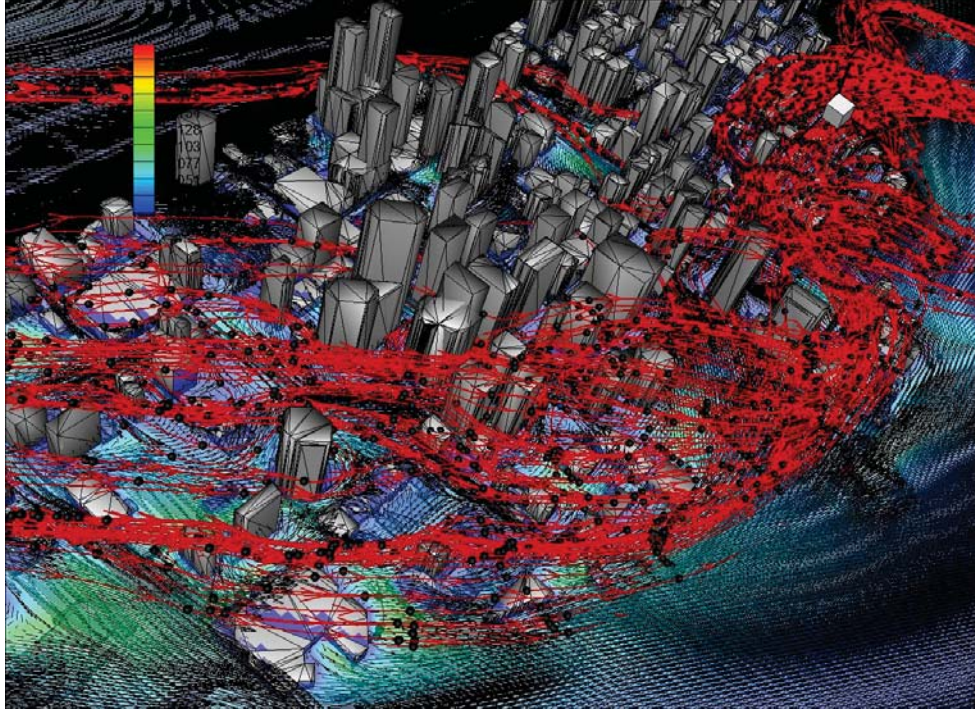
**Figure 11.** Sample streamline patterns and associated velocity fields at 135° wind direction in the City of Calgary.
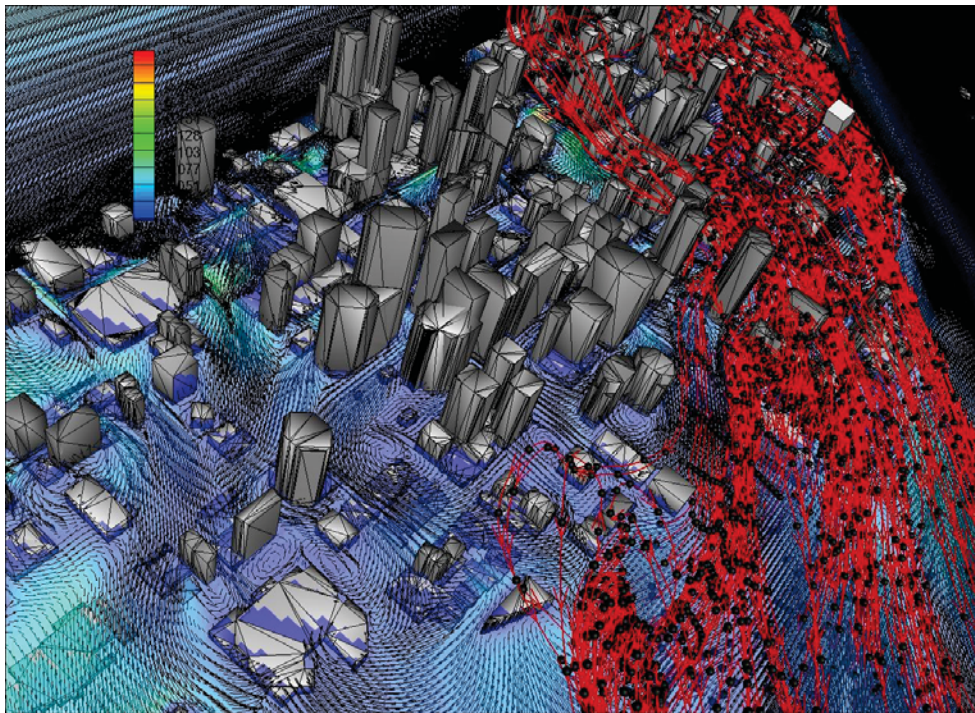


**Figure 12.** Sample streamline patterns and associated velocity fields at 225° wind direction in the City of Calgary.
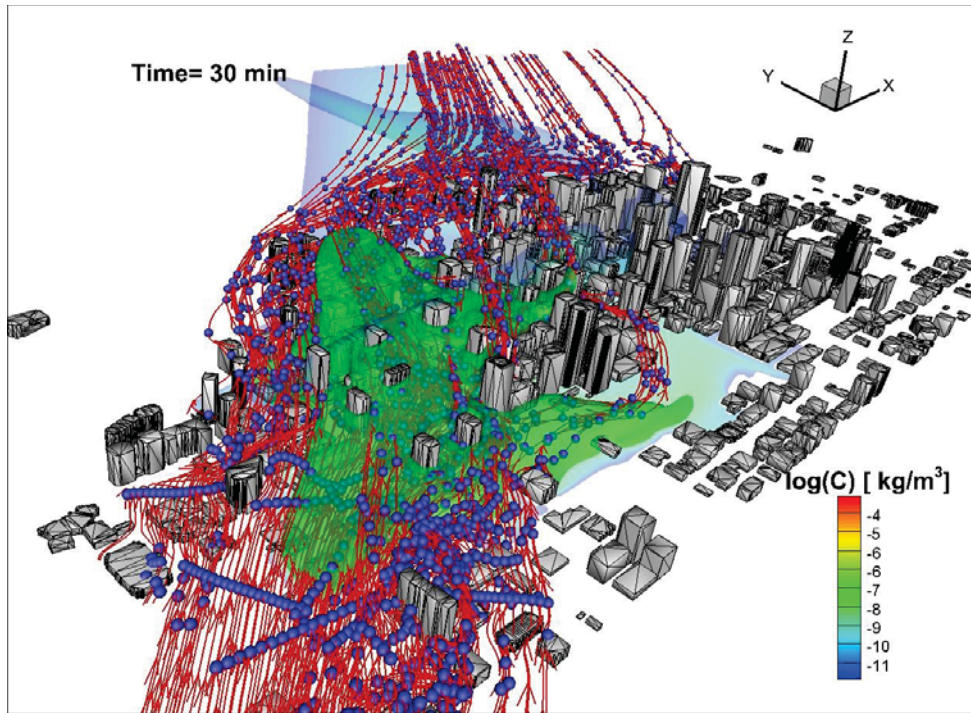
**Figure 13.** Scenario 1 **(**front view) – Sample streamline patterns superimposed with iso-surfaces of concentration at 225° wind direction in the City of Calgary.
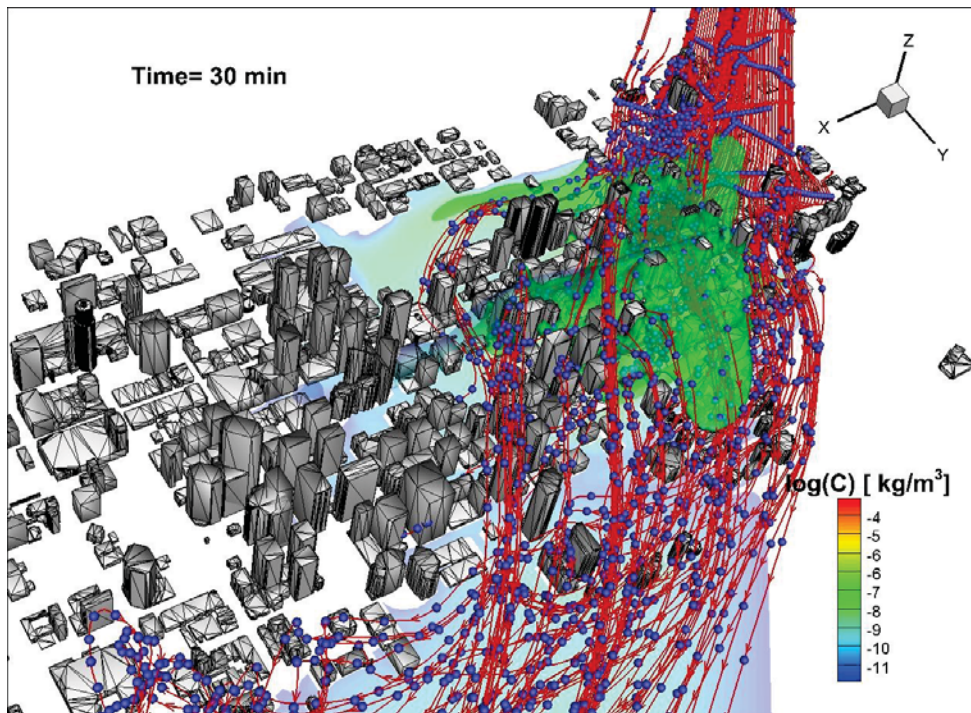


**Figure 14.** Scenario 1 **(**rear view) – Sample streamline patterns superimposed with iso-surfaces of concentration at 225° wind direction in the City of Calgary.
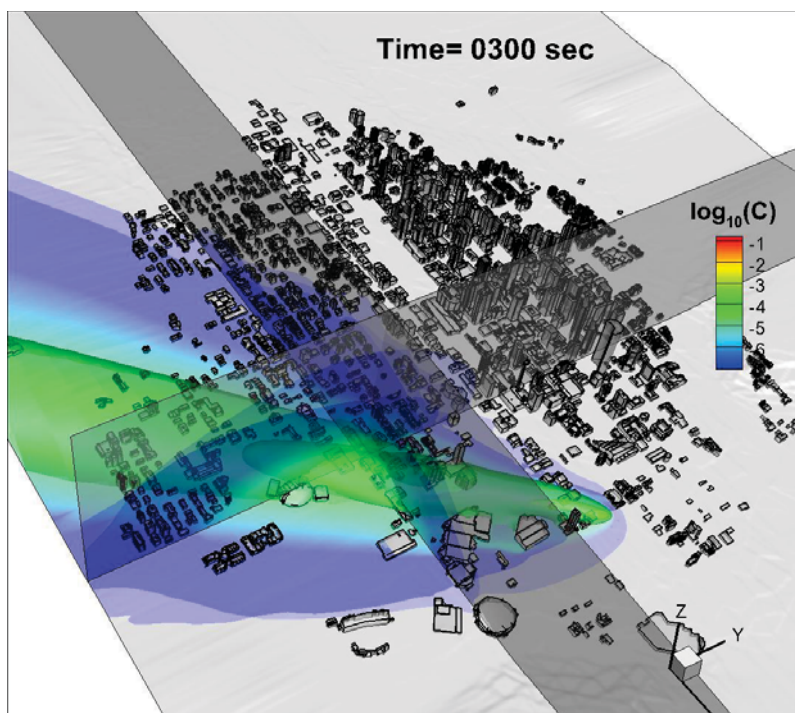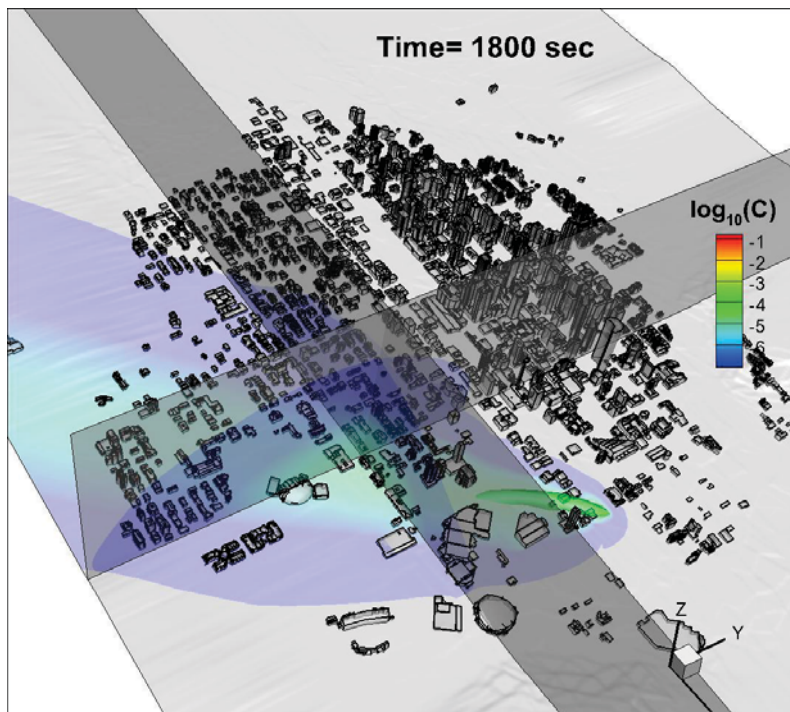
**Figure 15.** Scenario 1 – Contours of concentration on a logarithmic scale at *t* = 5 min at a wind direction of 45° with a source located at (51 deg, 02', 37.12" N, 114 deg, 03', 11.89" W).
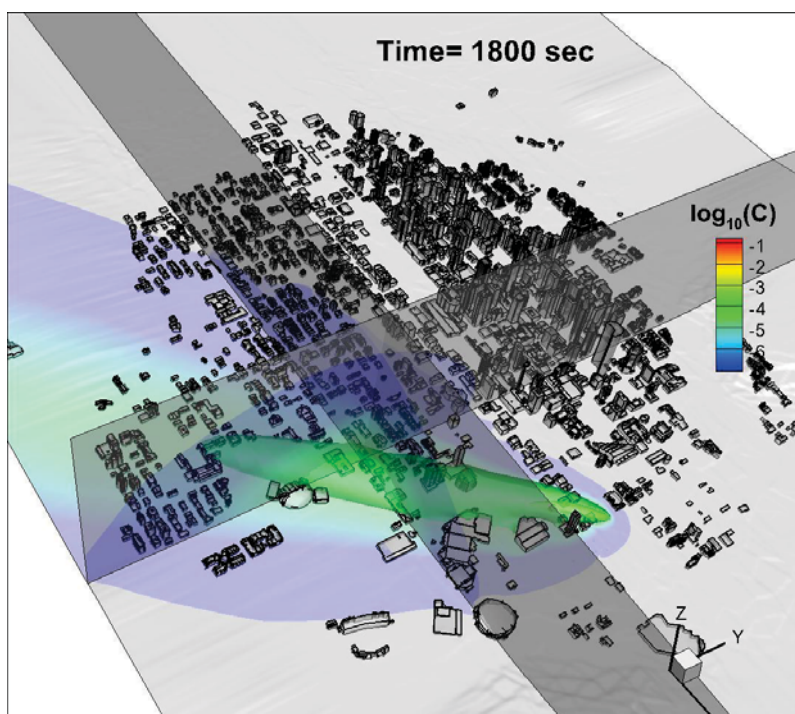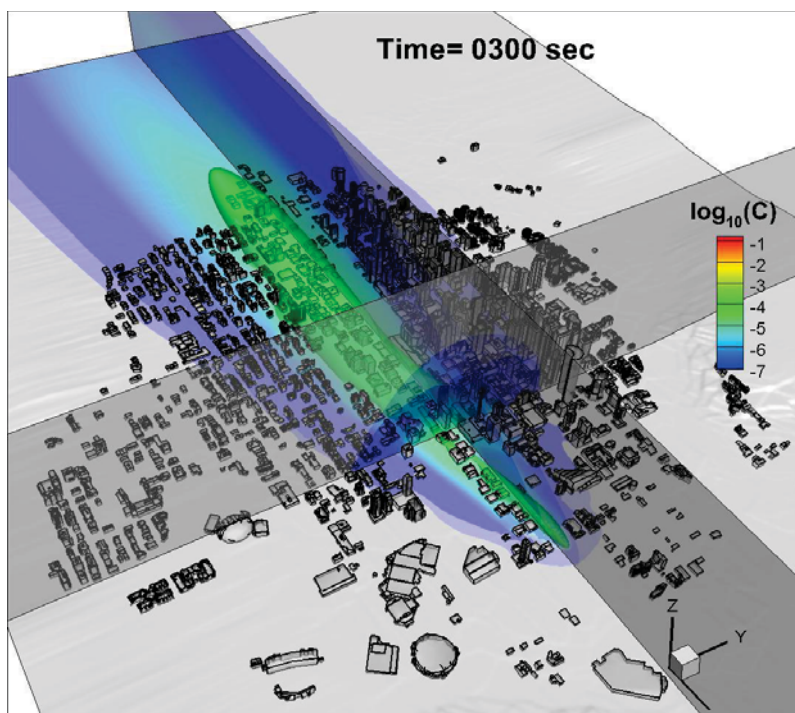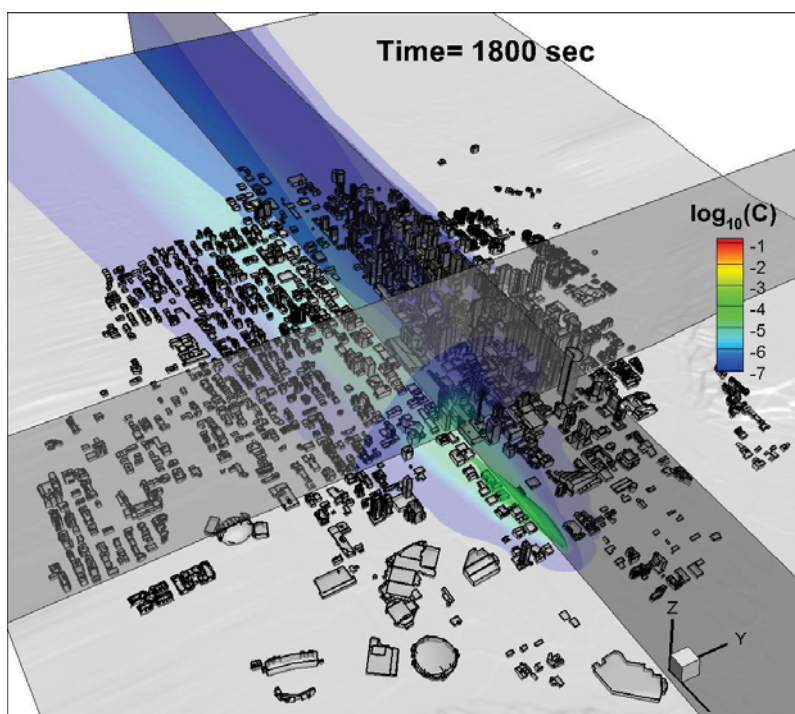


**Figure 16.** Scenario 1 – Contours of concentration on a logarithmic scale at *t* = 30 min at a wind direction of 45° with a source located at (51 deg, 02', 37.12" N, 114 deg, 03', 11.89" W).
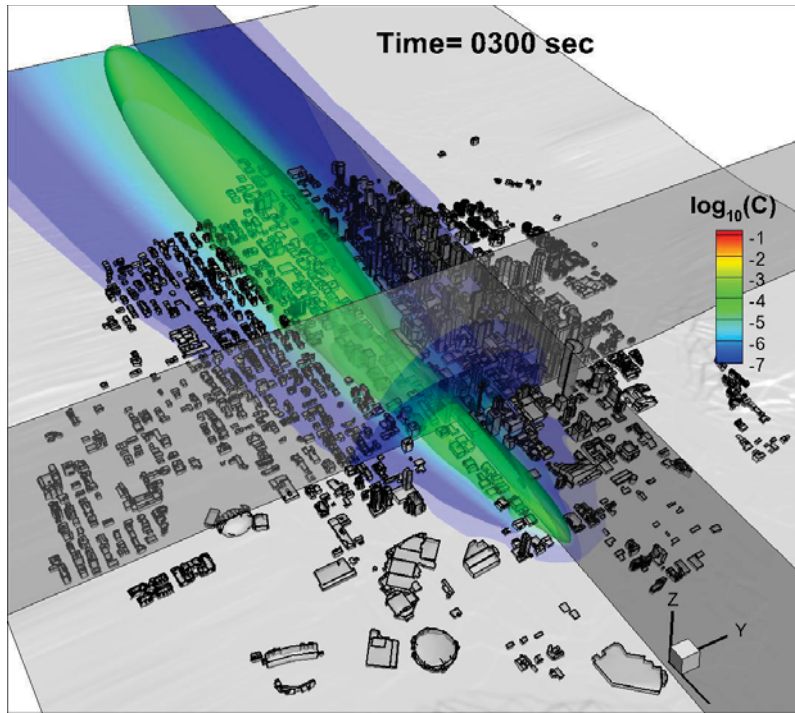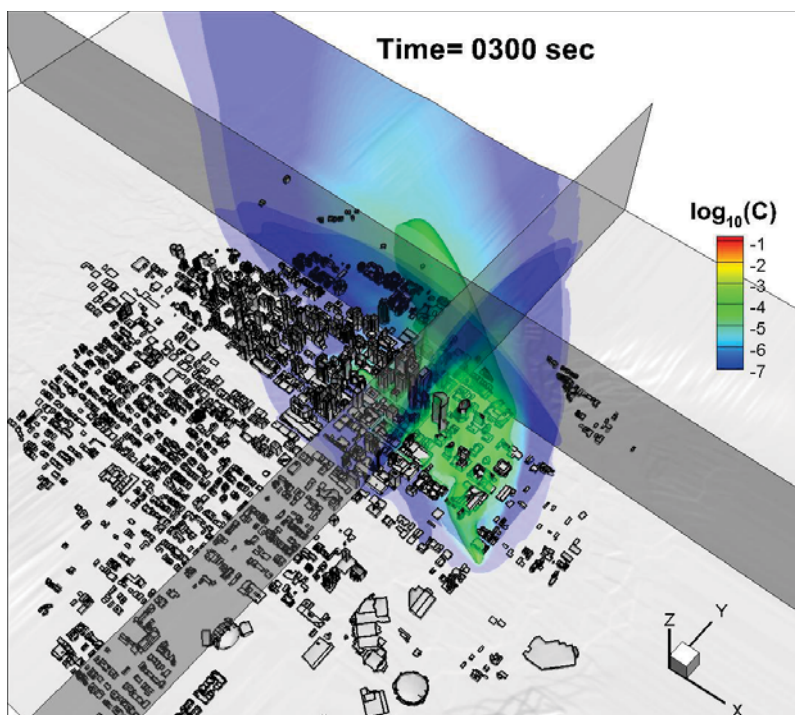
**Figure 17.** Scenario 1 – Contours of concentration on a logarithmic scale at *t* = 5 min at a wind direction of 90° with a source located at (51 deg, 02', 37.12" N, 114 deg, 03', 11.89" W).
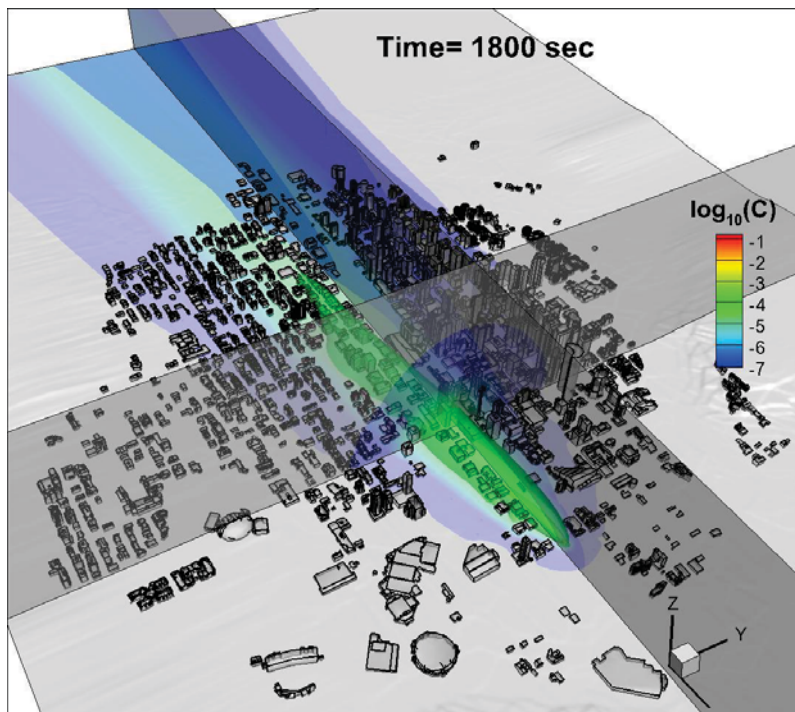
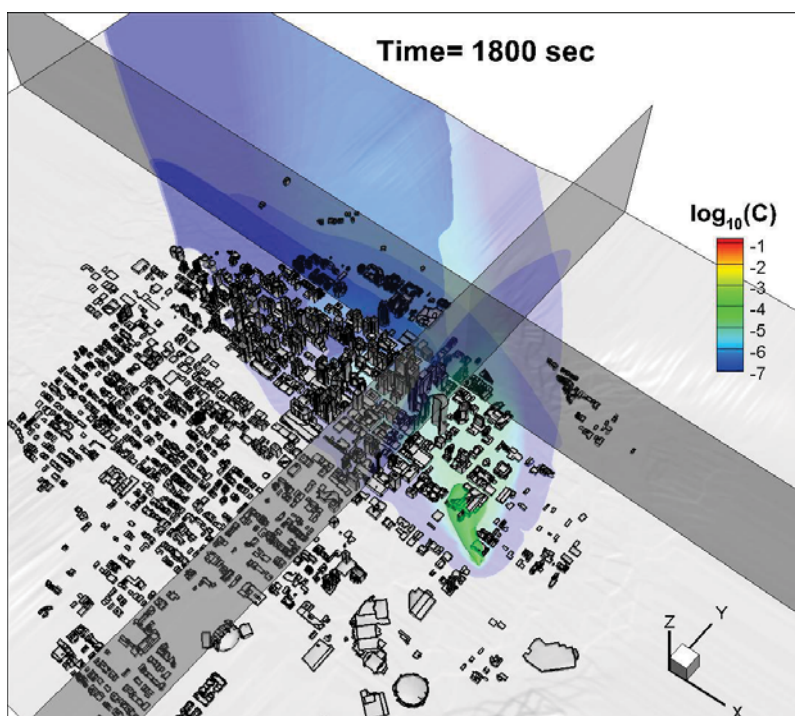

**Figure 18.** Scenario 1 – Contours of concentration on a logarithmic scale at *t* = 30 min at a wind direction of 90° with a source located at (51 deg, 02', 37.12" N, 114 deg, 03', 11.89" W).
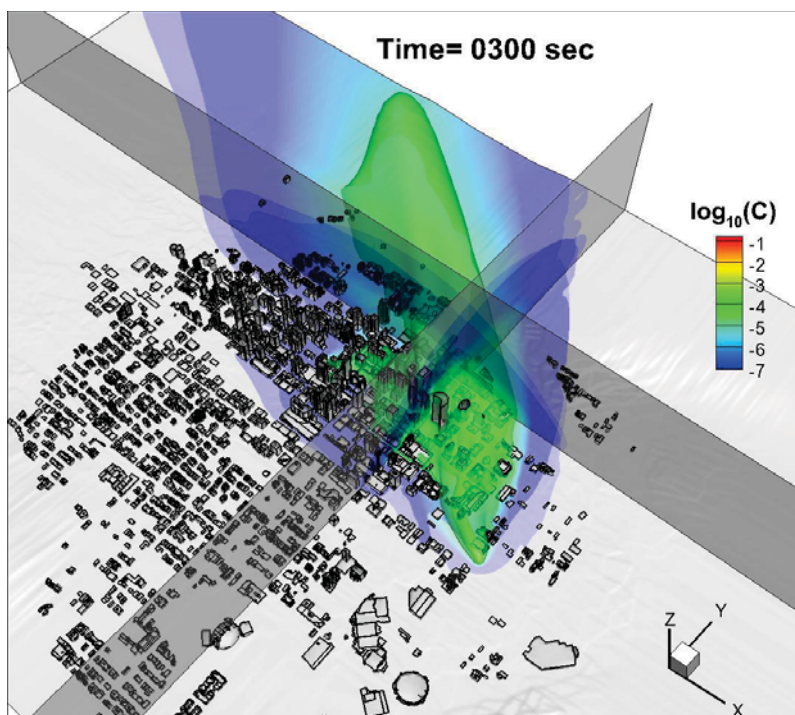
**Figure 19.** Scenario 1 – Contours of concentration on a logarithmic scale at $t$ = 5 min at a wind direction of 135° with a source located at (51 deg, 02', 37.12" N, 114 deg, 03', 11.89" W).
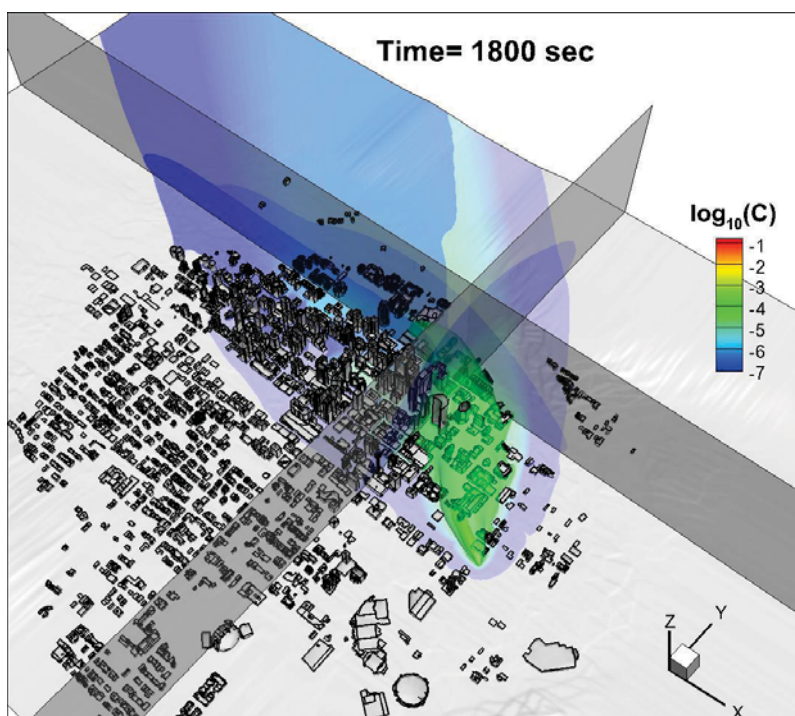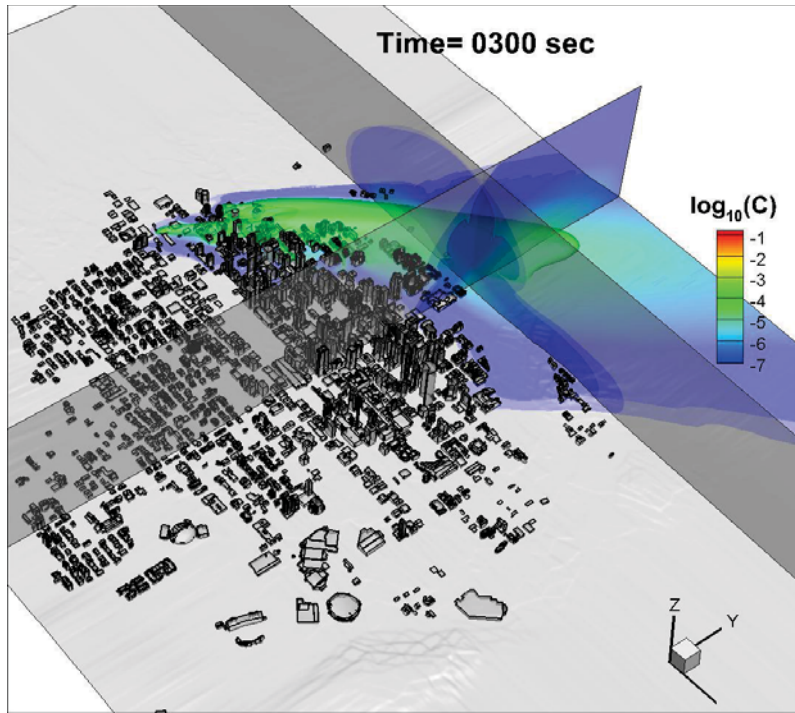


**Figure 20.** Scenario 1 – Contours of concentration on a logarithmic scale at $t$ = 30 min at a wind direction of 135° with a source located at (51 deg, 02', 37.12" N, 114 deg, 03', 11.89" W).
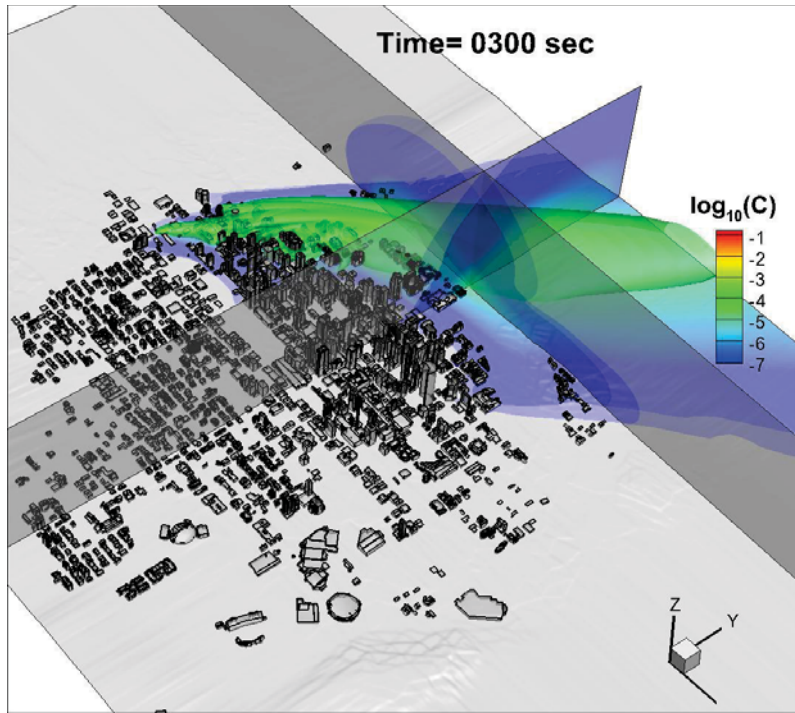
**Figure 21.** Scenario 1 – Contours of concentration on a logarithmic scale at $t$ = 5 min at a wind direction of 225° with a source located at (51 deg, 02', 41.07" N, 114 deg, 05', 14.09" W).
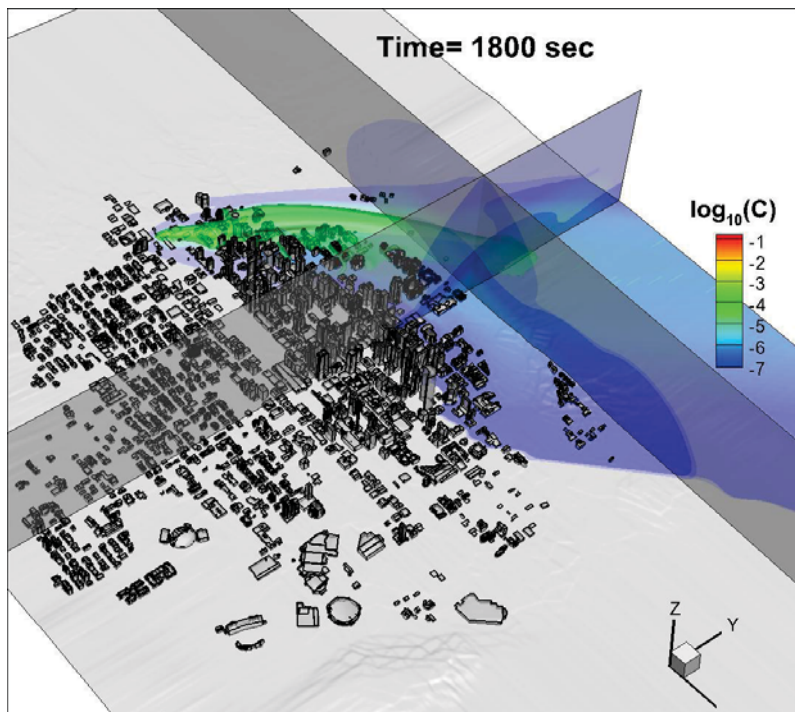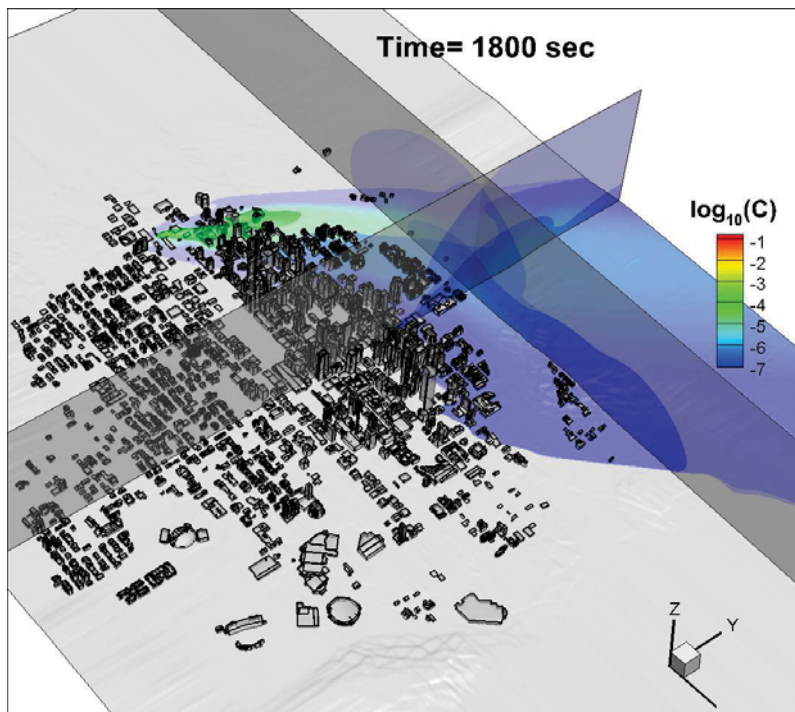


**Figure 22.** Scenario 1 – Contours of concentration on a logarithmic scale at $t$ = 30 min at a wind direction of 225° with a source located at (51 deg, 02', 41.07" N, 114 deg, 05', 14.09" W).
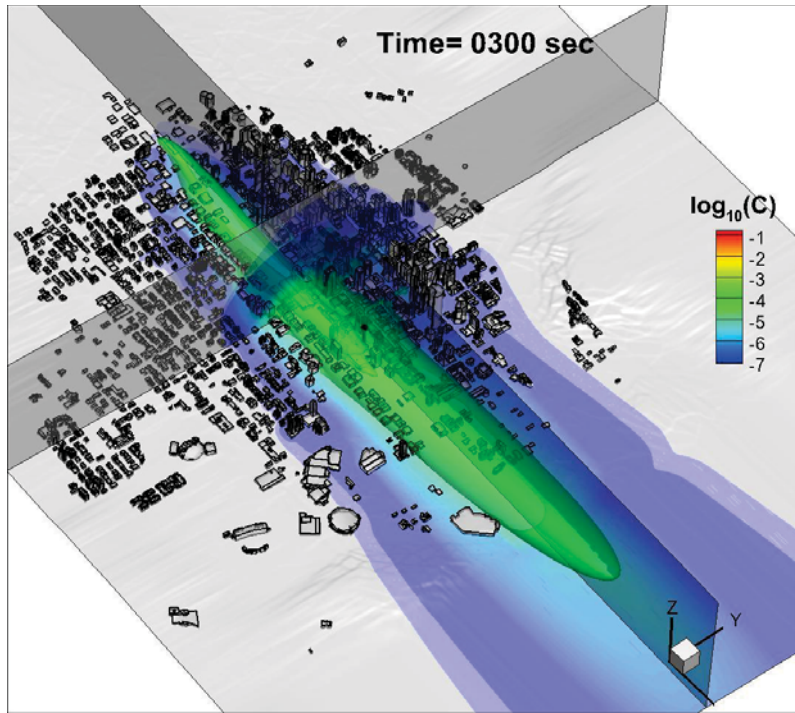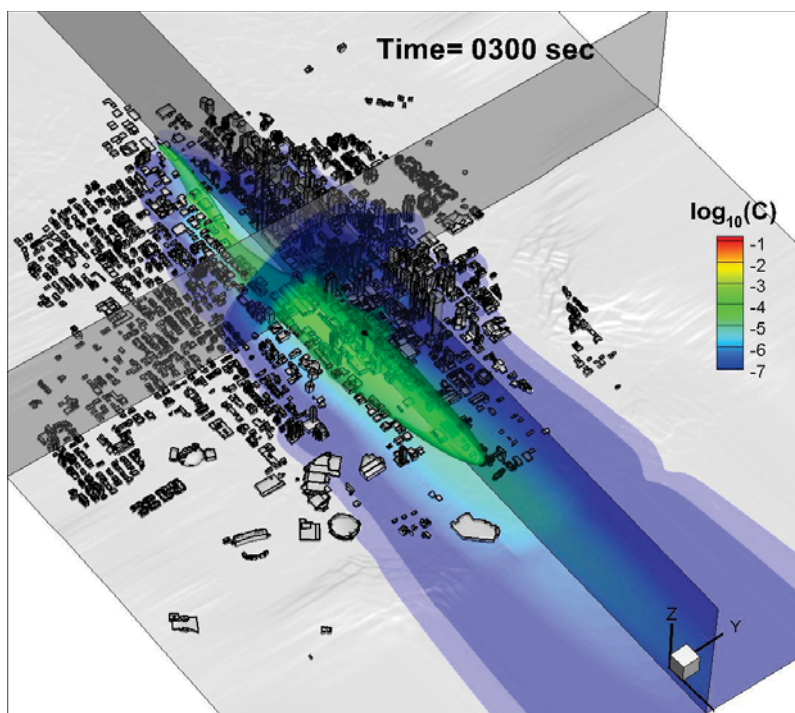
**Figure 23.** Scenario 1 – Contours of concentration on a logarithmic scale at *t* = 5 min at a wind direction of 270° with a source located at (51 deg, 02', 41.07" N, 114 deg, 05', 14.09" W).
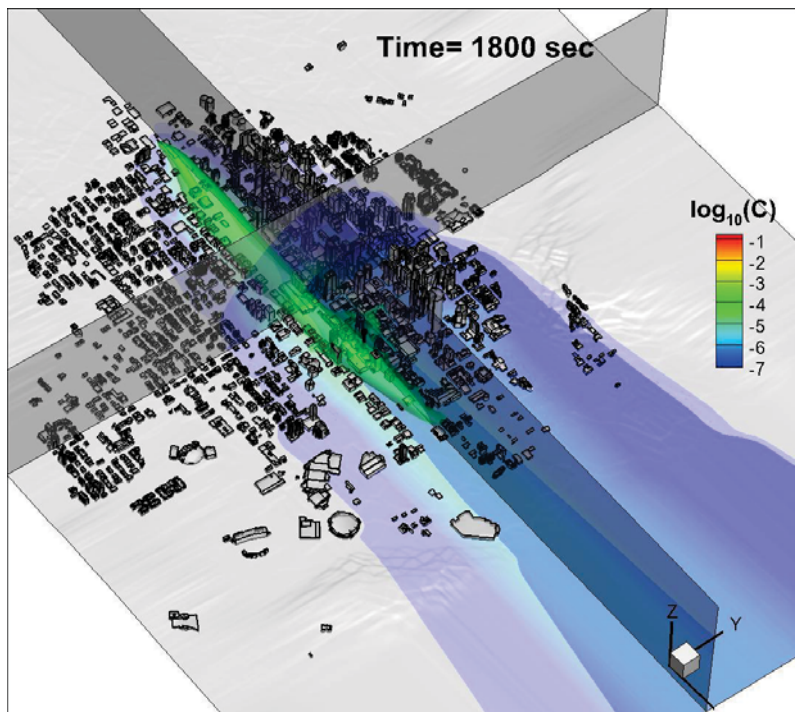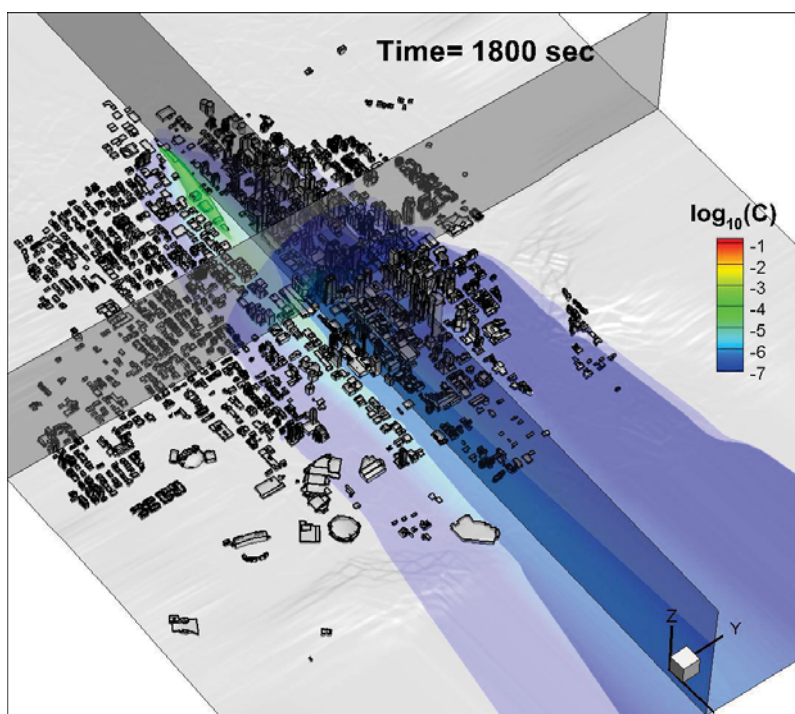


**Figure 24.** Scenario 1 – Contours of concentration on a logarithmic scale at *t* = 30 min at a wind direction of 270° with a source located at (51 deg, 02', 41.07" N, 114 deg, 05', 14.09" W).
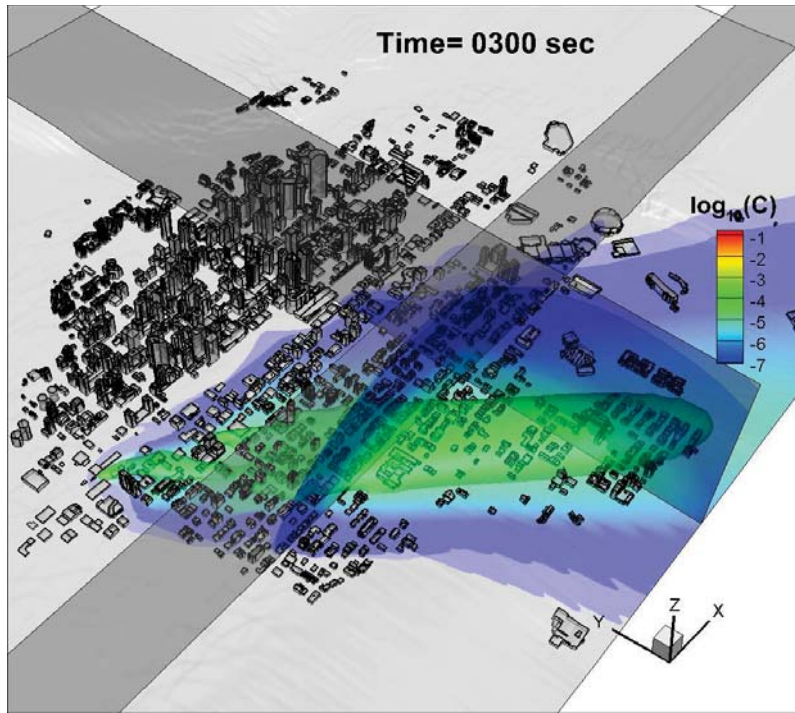
47
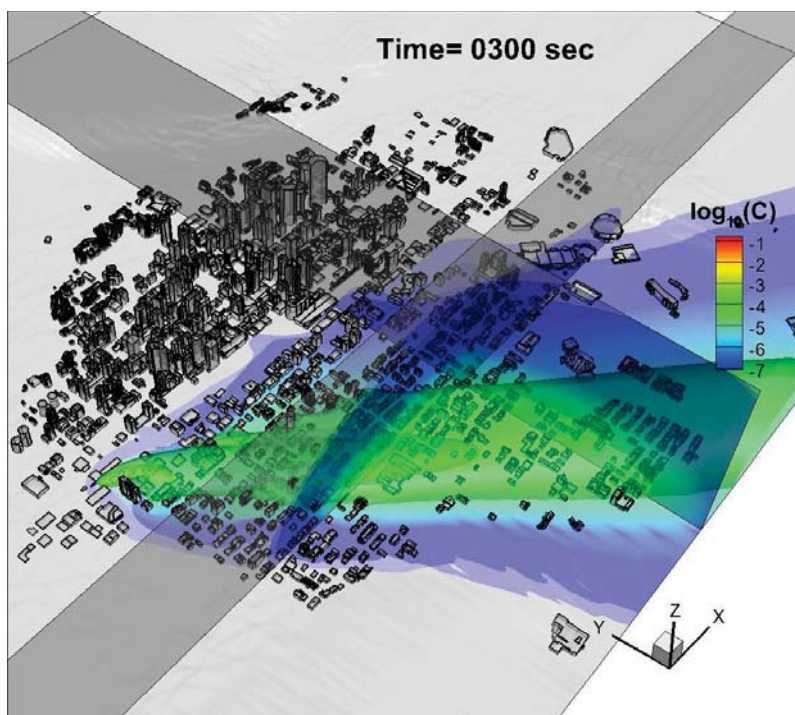
**Figure 25.** Scenario 1 – Contours of concentration on a logarithmic scale at *t* = 5 min at a wind direction of 315° with a source located at (51 deg, 02', 41.07" N, 114 deg, 05', 14.09" W).
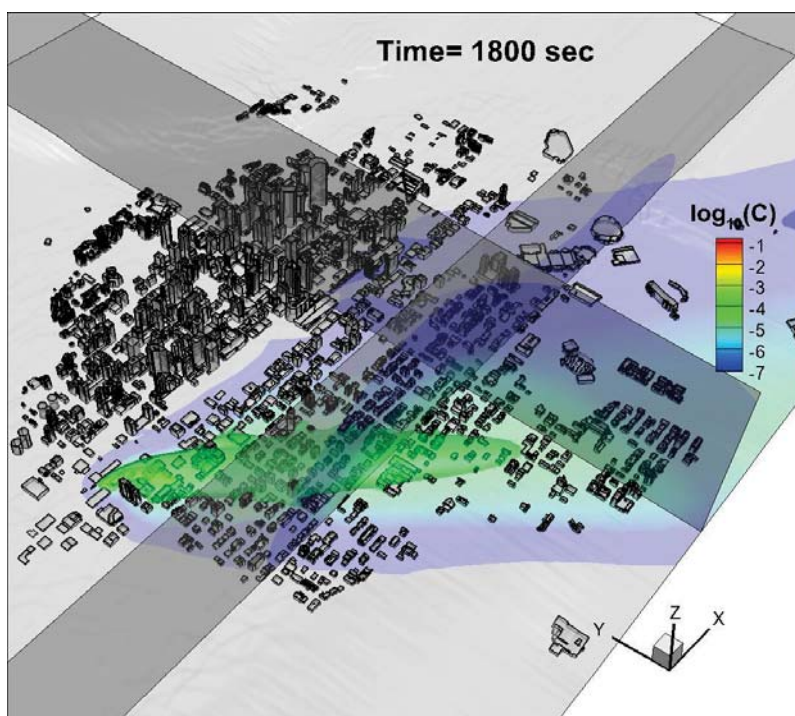


**Figure 26.** Scenario 1 – Contours of concentration on a logarithmic scale at *t* = 30 min at a wind direction of 315° with a source located at (51 deg, 02', 41.07" N, 114 deg, 05', 14.09" W).
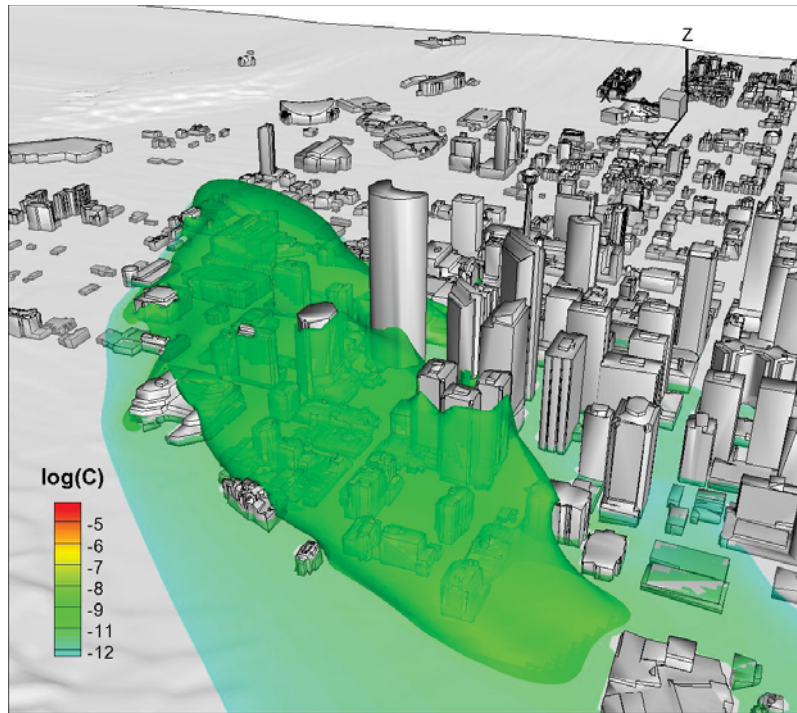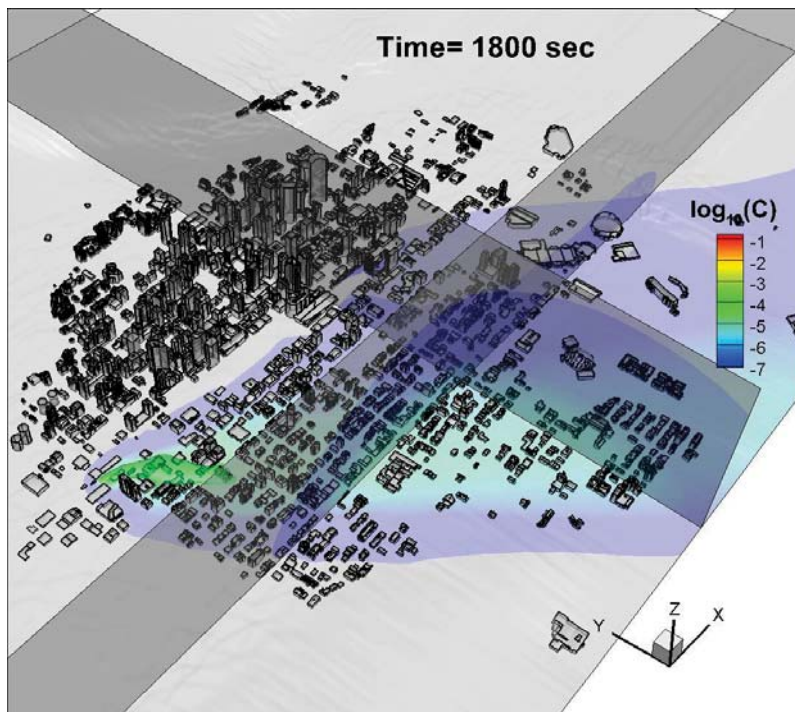
**Figure 27.** Scenario 1 – Contours of concentration of a dense gas (chlorine) at $t$ = 10 min at a wind direction of 135° with a source at Location 1 using the "Q-approach".
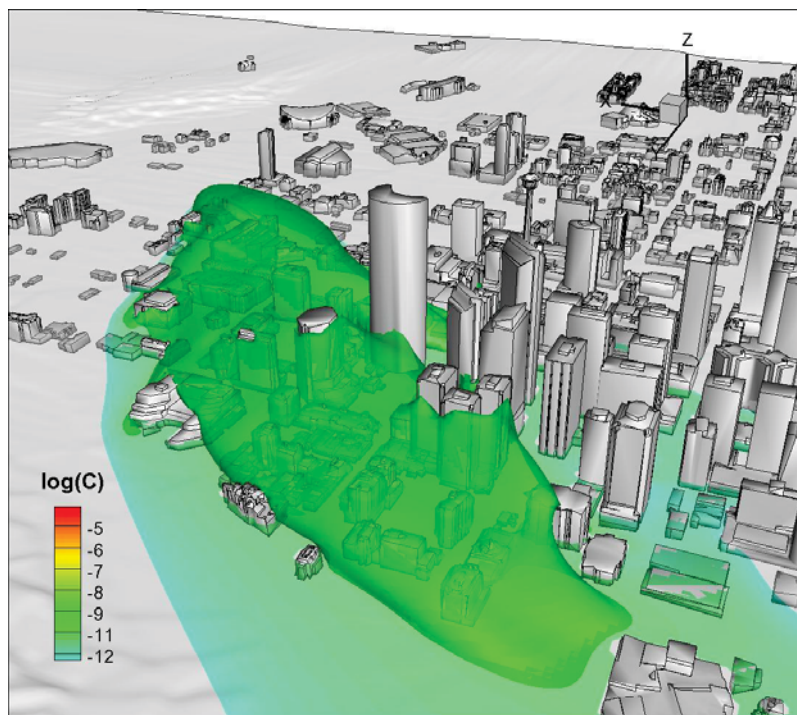


**Figure 28.** Scenario 1 – Contours of concentration of a dense gas (chlorine) at $t$ = 10 min at a wind direction of 135° with a source at Location 1 using the "$W_{jet}$-approach".
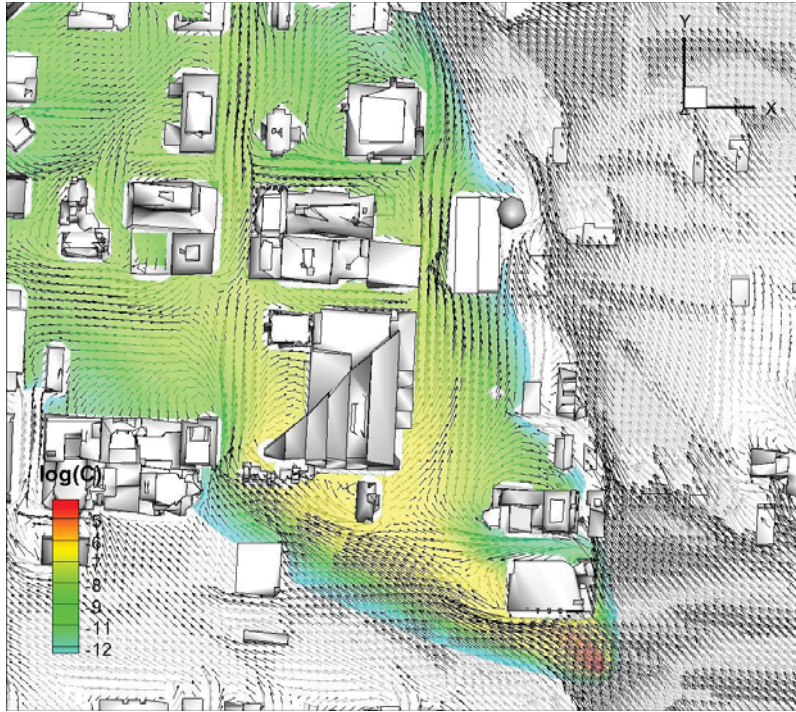
**Figure 29.** Scenario 1 (dense gas result) – Contours of log(C) superimposed with the velocity vector field at *t* = 10 min at a wind direction of 135° with a source at Location 1.
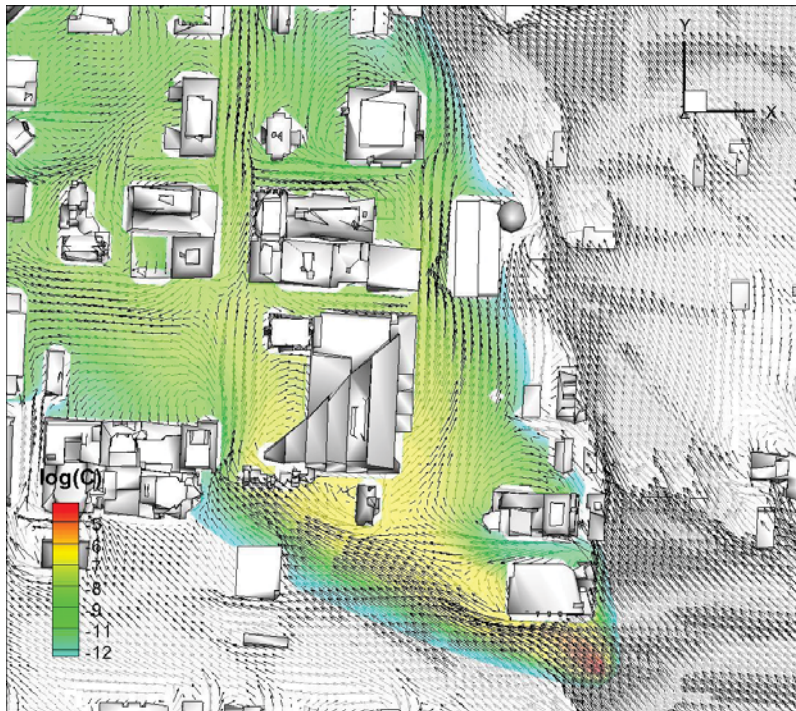


**Figure 30.** Scenario 1 (passive gas result) – Contours of log(C) superimposed with the velocity vector field at *t* = 10 min at a wind direction of 135° with a source at Location 1.
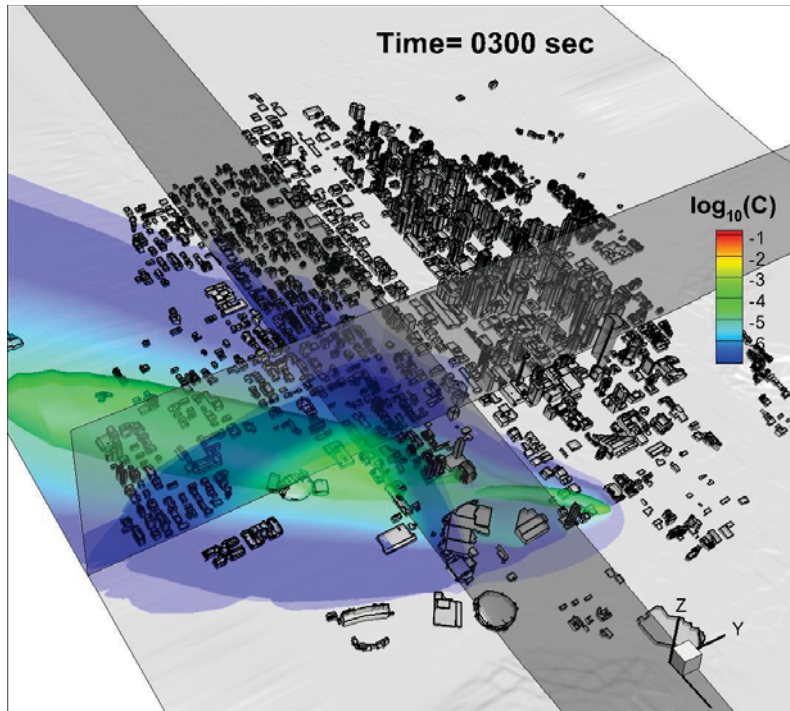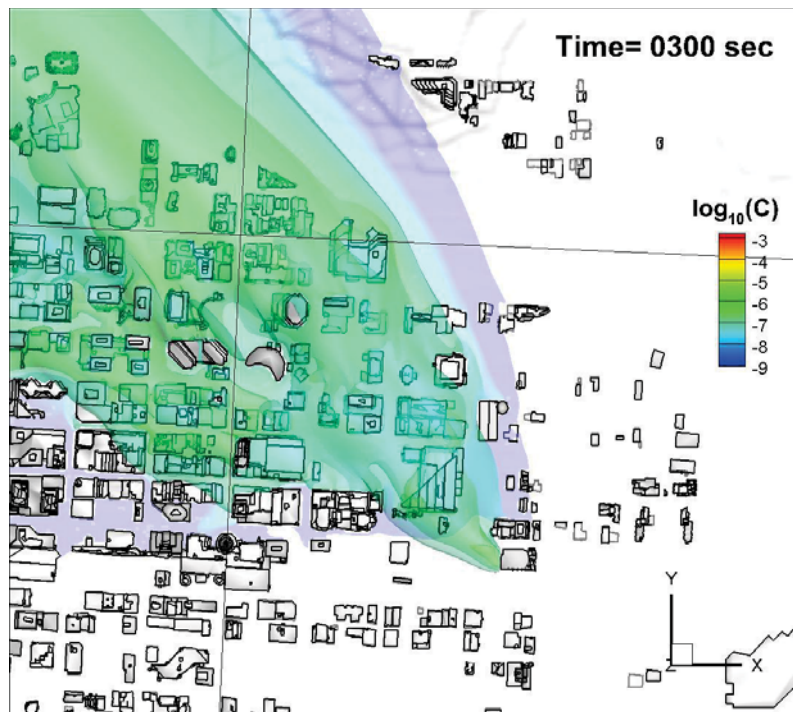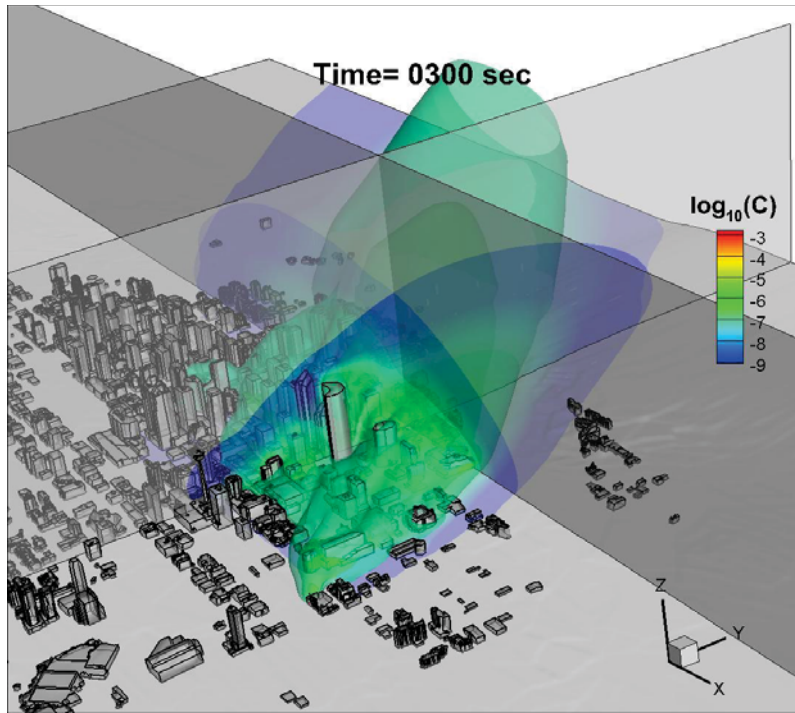
**Figure 31.** Scenario 2 – Contours of concentration on a logarithmic scale at $t$ = 5 min at a wind direction of 45° with a source located at (51 deg, 02', 37.12" N, 114 deg, 03', 11.89" W).



**Figure 32.** Scenario 2 – Contours of concentration on a logarithmic scale at $t$ = 30 min at a wind direction of 45° with a source located at (51 deg, 02', 37.12" N, 114 deg, 03', 11.89" W).

**Figure 33.** Scenario 2 – Contours of concentration on a logarithmic scale at $t = 5$ min at a wind direction of 90° with a source located at (51 deg, 02', 37.12" N, 114 deg, 03', 11.89" W).



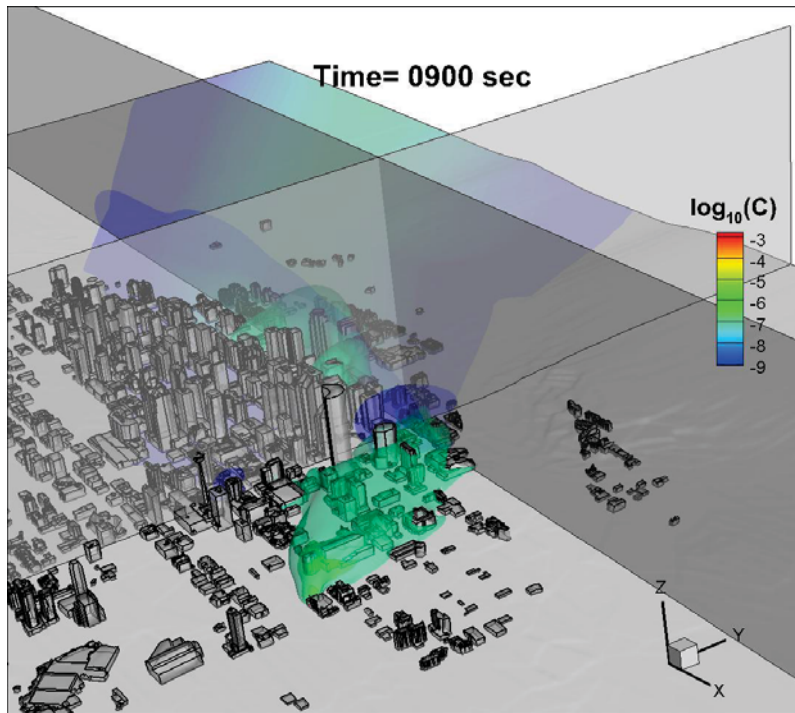**Figure 34.** Scenario 2 – Contours of concentration on a logarithmic scale at $t = 30$ min at a wind direction of 90° with a source located at (51 deg, 02', 37.12" N, 114 deg, 03', 11.89" W).
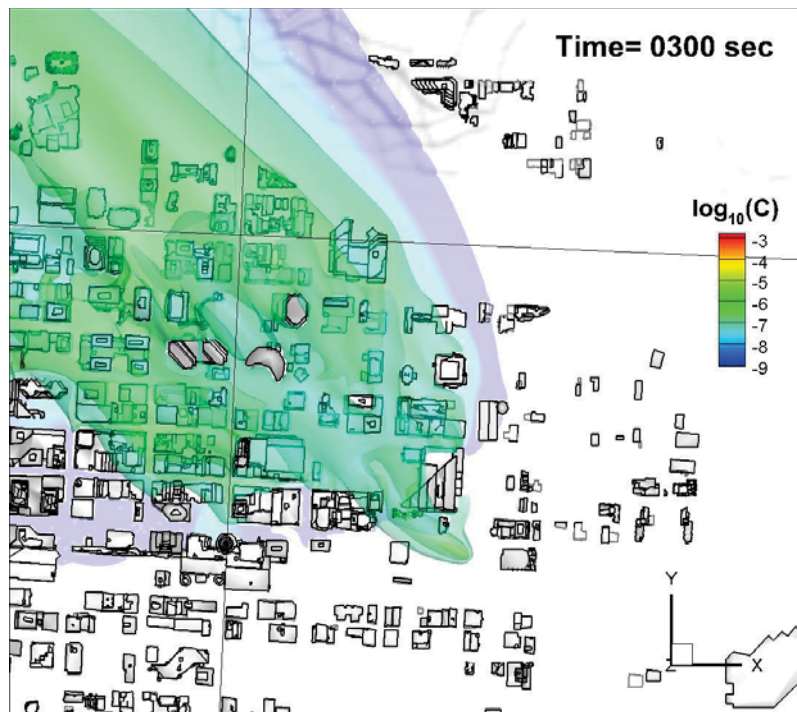
**Figure 35.** Scenario 2 – Contours of concentration on a logarithmic scale at *t* = 5 min at a wind direction of 135° with a source located at (51 deg, 02', 37.12" N, 114 deg, 03', 11.89" W).



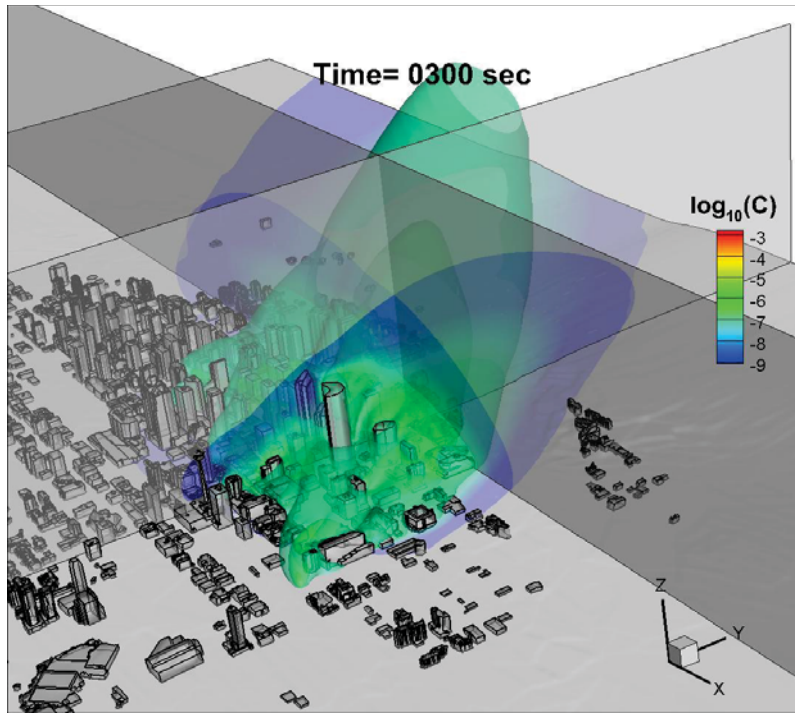**Figure 36.** Scenario 2 – Contours of concentration on a logarithmic scale at *t* = 30 min at a wind direction of 135° with a source located at (51 deg, 02', 37.12" N, 114 deg, 03', 11.89" W).

**Figure 37.** Scenario 2 – Contours of concentration on a logarithmic scale at $t$ = 5 min at a wind direction of 225° with a source located at (51 deg, 02', 41.07" N, 114 deg, 05', 14.09" W).



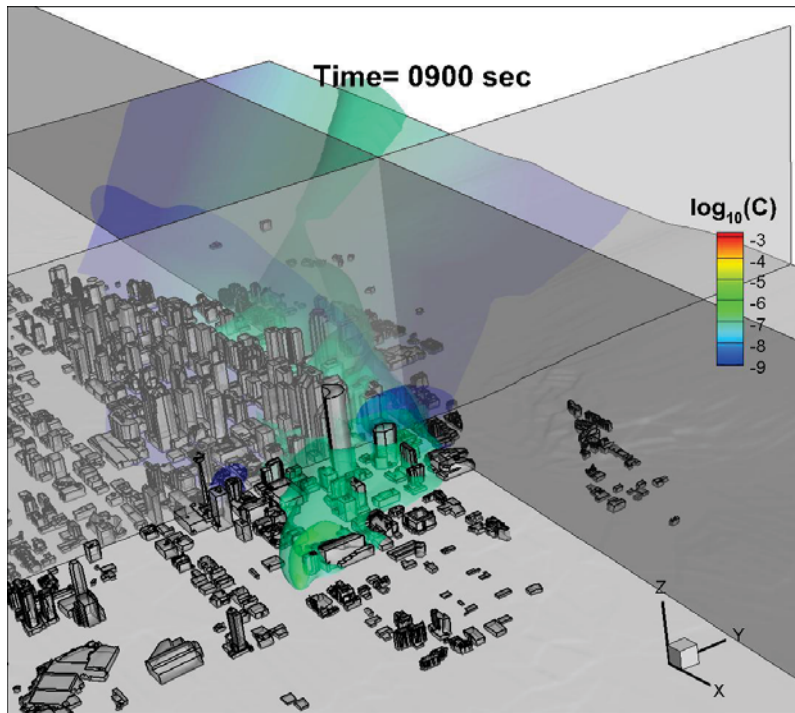**Figure 38.** Scenario 2 – Contours of concentration on a logarithmic scale at $t$ = 30 min at a wind direction of 225° with a source located at (51 deg, 02', 41.07" N, 114 deg, 05', 14.09" W).

**Figure 39.** Scenario 2 – Contours of concentration on a logarithmic scale at $t$ = 5 min at a wind direction of 270° with a source located at (51 deg, 02', 41.07" N, 114 deg, 05', 14.09" W).



**Figure 40.** Scenario 2 – Contours of concentration on a logarithmic scale at $t$ = 30 min at a wind direction of 270° with a source located at (51 deg, 02', 41.07" N, 114 deg, 05', 14.09" W).

**Figure 41.** Scenario 2 – Contours of concentration on a logarithmic scale at *t* = 5 min at a wind direction of 315° with a source located at (51 deg, 02', 41.07" N, 114 deg, 05', 14.09" W).



**Figure 42.** Scenario 2 – Contours of concentration on a logarithmic scale at *t* = 30 min at a wind direction of 315° with a source located at (51 deg, 02', 41.07" N, 114 deg, 05', 14.09" W).

Datasets delivered to 3DInternet [**Δt=1 sec**]
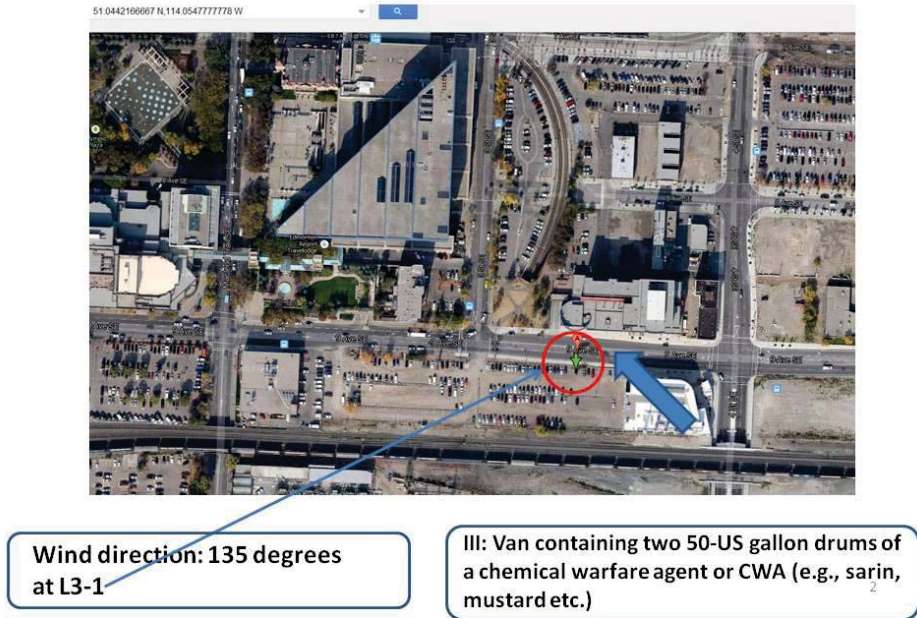


**Figure 43.** Scenario 3 – Location of the source L3-1 at (51 deg, 02', 39.18" N, 114 deg, 03', 17.20" W) at a wind direction of 135°.



**Figure 44.** Scenario 3 – Top view of contours of concentration on a logarithmic scale at $t = 5$ min at a wind direction of 135° with the source L3-1 located at (51 deg, 02', 39.18" N, 114 deg, 03', 17.20" W).
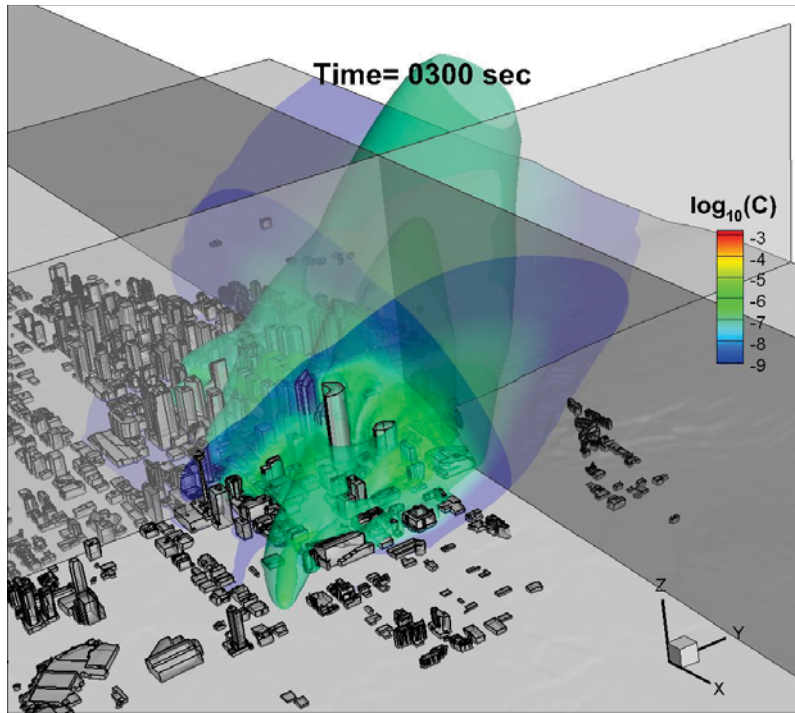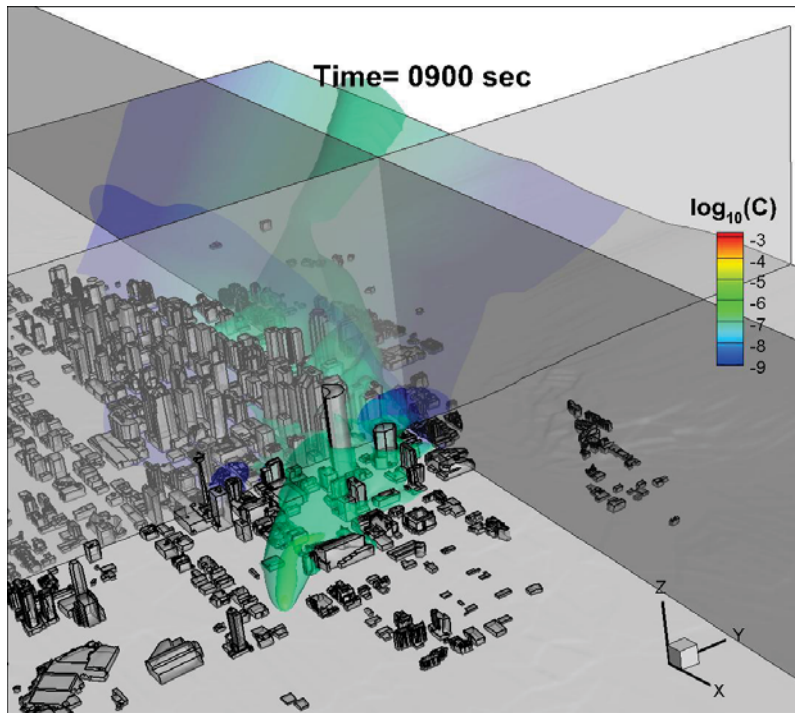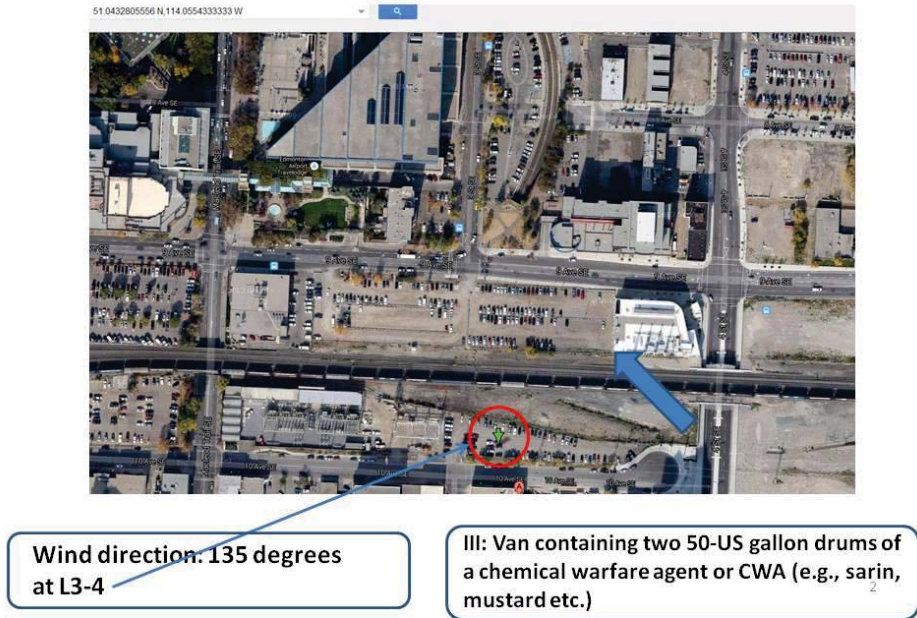
**Figure 45.** Scenario 3 – Contours of concentration on a logarithmic scale at $t$ = 5 min at a wind direction of 135° with the source L3-1 located at (51 deg, 02', 39.18" N, 114 deg, 03', 17.20" W).



**Figure 46.** Scenario 3 – Contours of concentration on a logarithmic scale at $t$ = 15 min at a wind direction of 135° with the source L3-1 located at (51 deg, 02', 39.18" N, 114 deg, 03', 17.20" W).

**Wind direction: 135 degrees at L3-2**

**III: Van containing two 50-US gallon drums of a chemical warfare agent or CWA (e.g., sarin, mustard etc.)**

**Figure 47.** Scenario 3 – Location of the source L3-2 at (51 deg, 02', 38.62" N, 114 deg, 03', 20.18" W) at a wind direction of 135°.
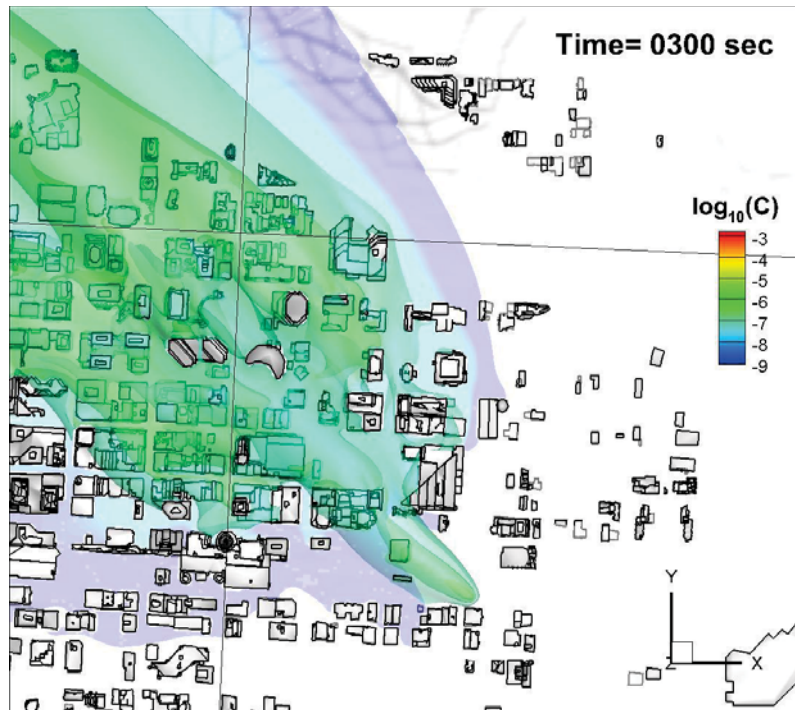


**Figure 48.** Scenario 3 – Top view of contours of concentration on a logarithmic scale at $t = 5$ min at a wind direction of 135° with the source L3-2 located at (51 deg, 02', 38.62" N, 114 deg, 03', 20.18" W).
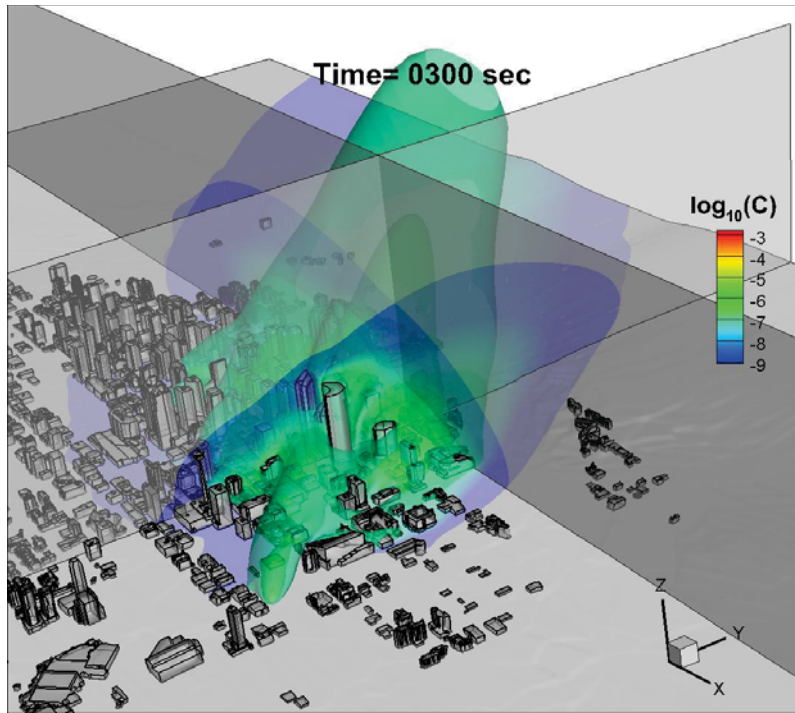
**Figure 49.** Scenario 3 – Contours of concentration on a logarithmic scale at *t* = 5 min at a wind direction of 135° with the source L3-2 located at (51 deg, 02', 38.62" N, 114 deg, 03', 20.18" W).
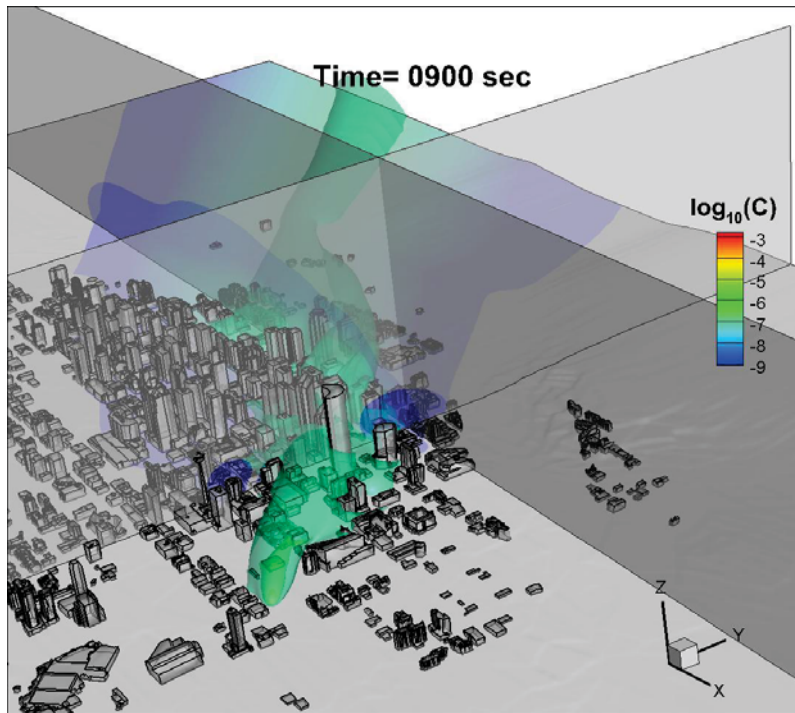


**Figure 50.** Scenario 3 – Contours of concentration on a logarithmic scale at *t* = 15 min at a wind direction of 135° with the source L3-2 located at (51 deg, 02', 38.62" N, 114 deg, 03', 20.18" W).
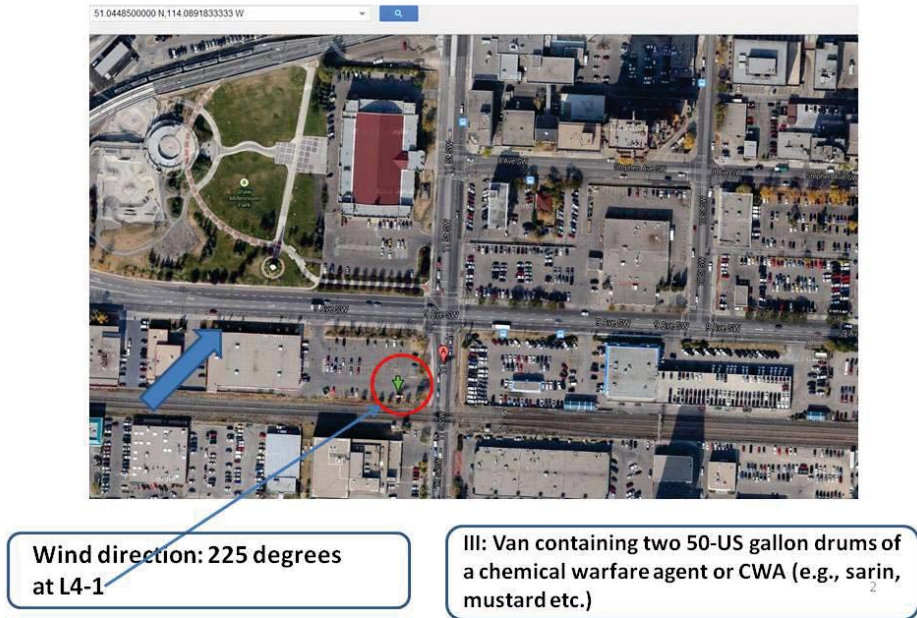
Datasets delivered to 3DInternet [**Δt=1 sec**]
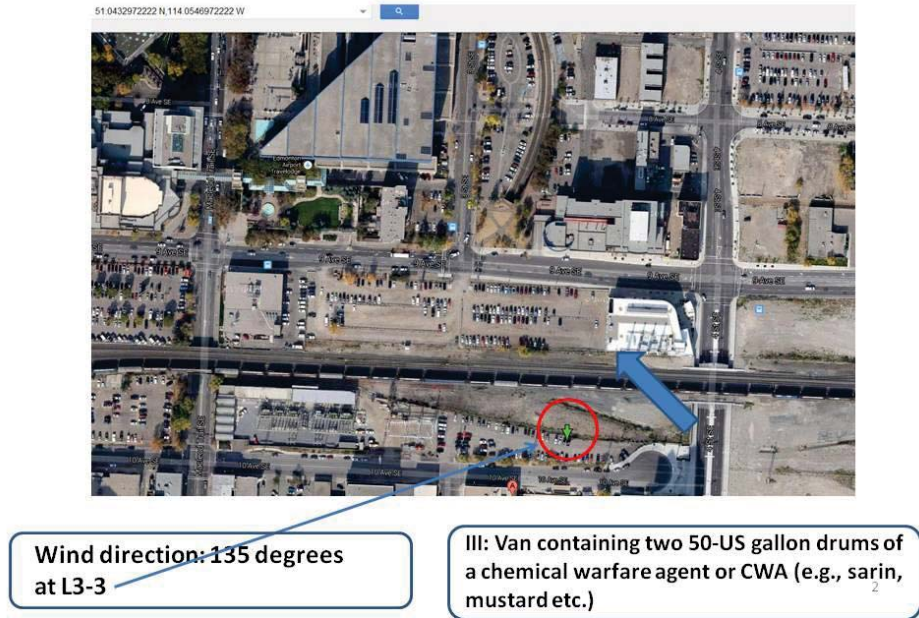


**Figure 51.** Scenario 3 – Location of the source L3-3 at (51 deg, 02', 35.87" N, 114 deg, 03', 16.91" W) at a wind direction of 135°.
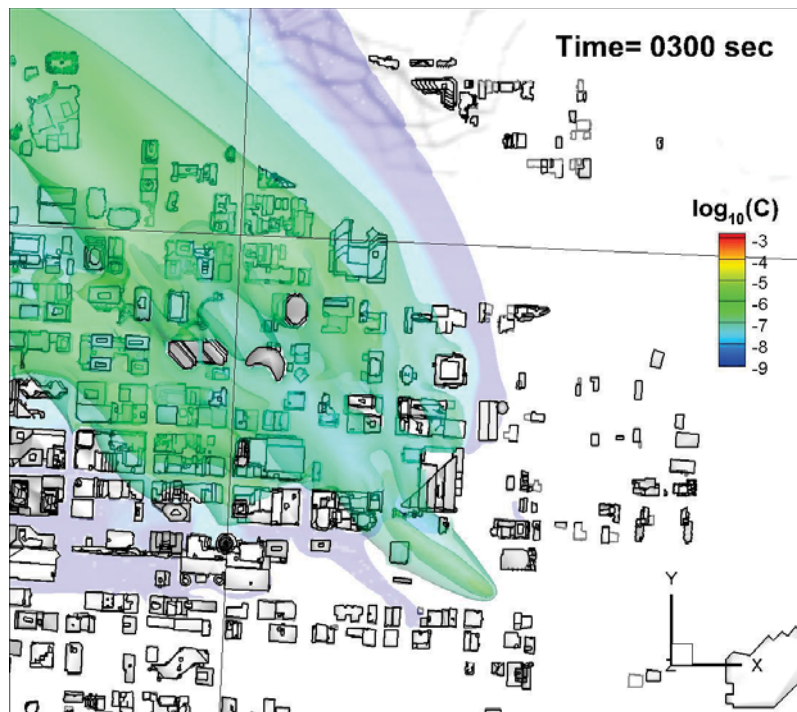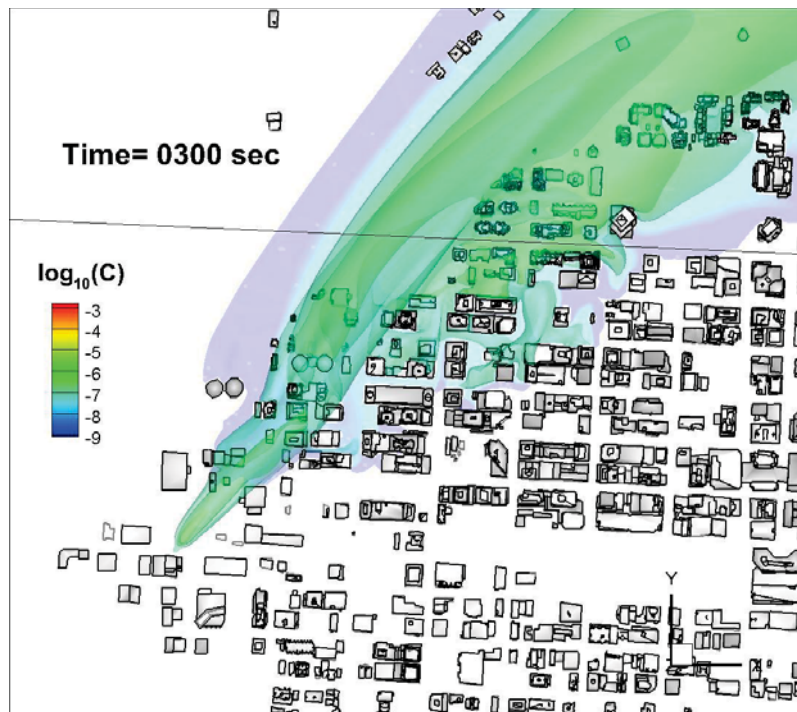


**Figure 52.** Scenario 3 – Top view of contours of concentration on a logarithmic scale at $t$ = 5 min at a wind direction of 135° with the source L3-3 located at (51 deg, 02', 35.87" N, 114 deg, 03', 16.91" W).
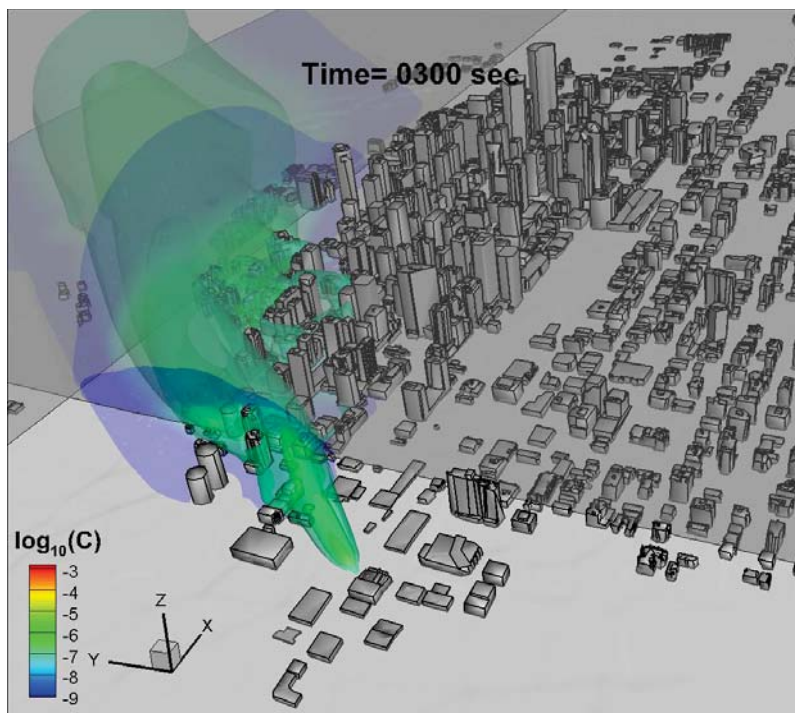
**Figure 53.** Scenario 3 – Contours of concentration on a logarithmic scale at $t$ = 5 min at a wind direction of 135° with the source L3-3 located at (51 deg, 02', 35.87" N, 114 deg, 03', 16.91" W).
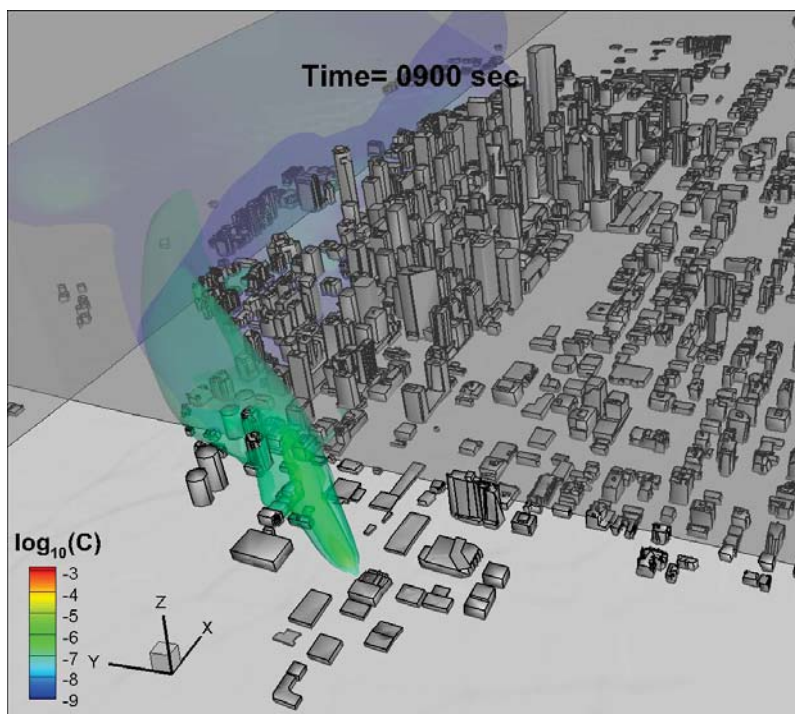


**Figure 54.** Scenario 3 – Contours of concentration on a logarithmic scale at $t$ = 15 min at a wind direction of 135° with the source L3-3 located at (51 deg, 02', 35.87" N, 114 deg, 03', 16.91" W).

Datasets delivered to 3DInternet [**Δt=1 sec**]



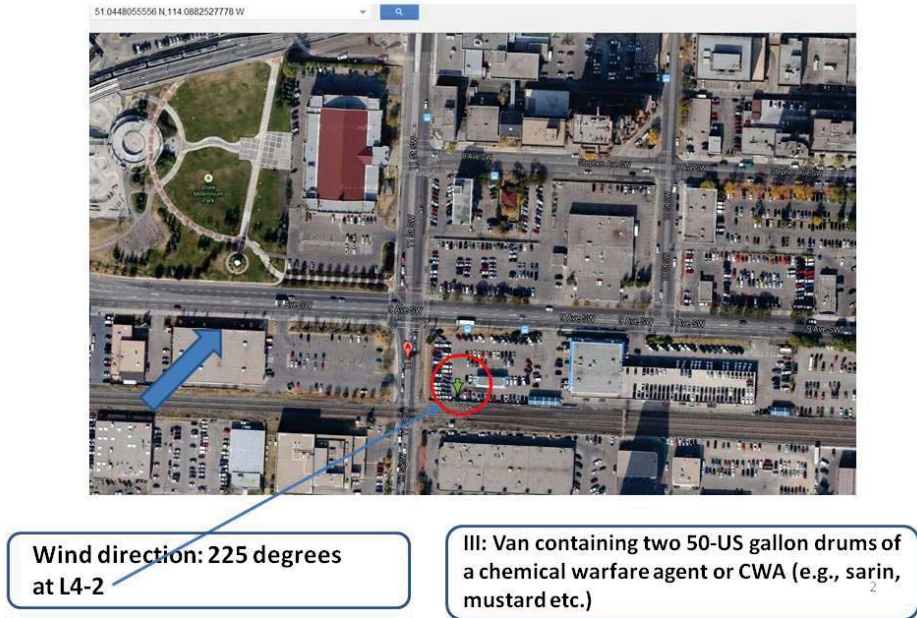**Figure 55.** Scenario 3 – Location of the source L3-4 at (51 deg, 02', 35.81" N, 114 deg, 03', 19.56" W) at a wind direction of 135°.
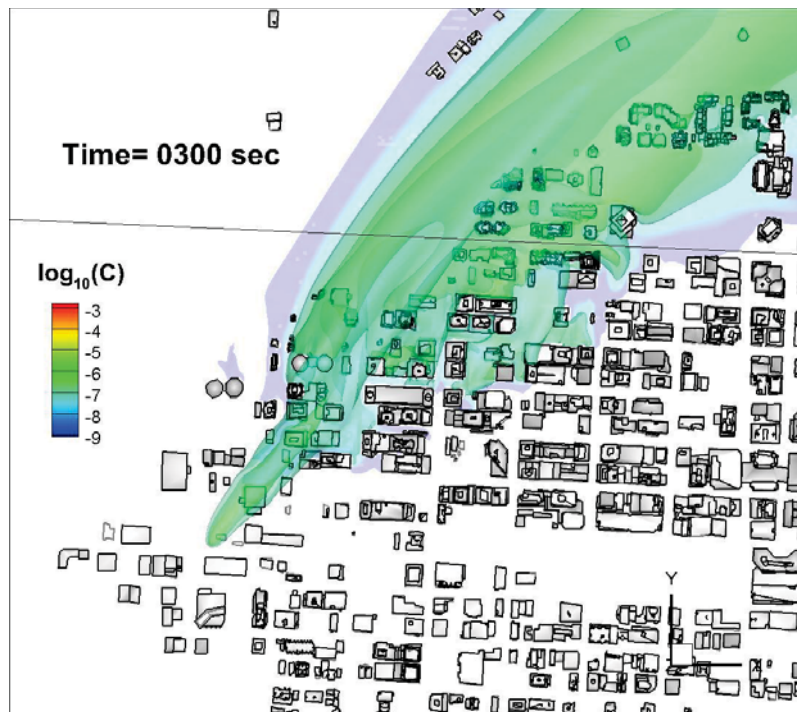


**Figure 56.** Scenario 3 – Top view of contours of concentration on a logarithmic scale at $t = 5$ min at a wind direction of 135° with the source L3-4 located at (51 deg, 02', 35.81" N, 114 deg, 03', 19.56" W).

**Figure 57.** Scenario 3 – Contours of concentration on a logarithmic scale at $t$ = 5 min at a wind direction of 225° with the source L3-4 located at (51 deg, 02', 35.81" N, 114 deg, 03', 19.56" W).
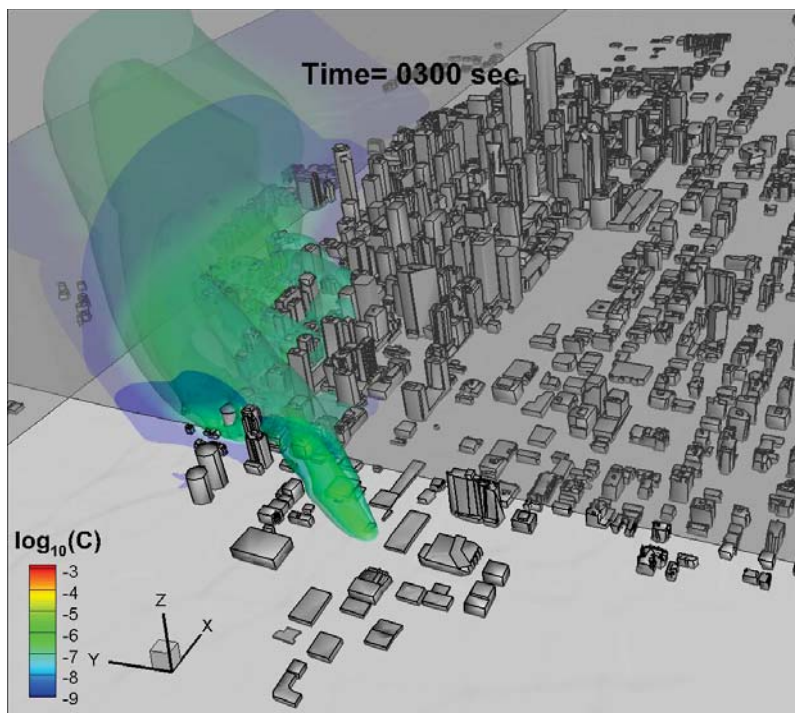


**Figure 58.** Scenario 3 – Contours of concentration on a logarithmic scale at $t$ = 15 min at a wind direction of 225° with the source L3-4 located at (51 deg, 02', 35.81" N, 114 deg, 03', 19.56" W).

Datasets delivered to 3DInternet [**Δt=1 sec**]

**Wind direction: 225 degrees at L4-1**

**III: Van containing two 50-US gallon drums of a chemical warfare agent or CWA (e.g., sarin, mustard etc.)**

**Figure 59.** Scenario 3 – Location of the source L4-1 at (51 deg, 02', 41.46" N, 114 deg, 05', 21.06" W) at a wind direction of 225°.



Time= 0300 sec

$\log_{10}(C)$

**Figure 60.** Scenario 3 – Top view of contours of concentration on a logarithmic scale at $t = 5$ min at a wind direction of 225° with the source L4-1 located at (51 deg, 02', 41.46" N, 114 deg, 05', 21.06" W).
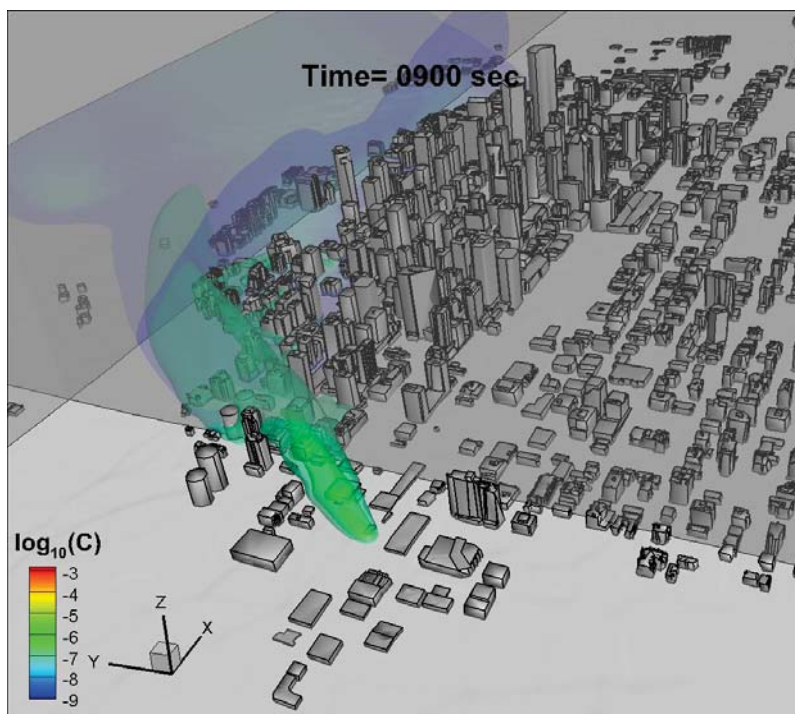
65

**Figure 61.** Scenario 3 – Contours of concentration on a logarithmic scale at $t = 5$ min at a wind direction of 225° with the source L4-1 located at (51 deg, 02', 41.46" N, 114 deg, 05', 21.06" W).



**Figure 62.** Scenario 3 – Contours of concentration on a logarithmic scale at $t = 15$ min at a wind direction of 225° with the source L4-1 located at (51 deg, 02', 41.46" N, 114 deg, 05', 21.06" W).
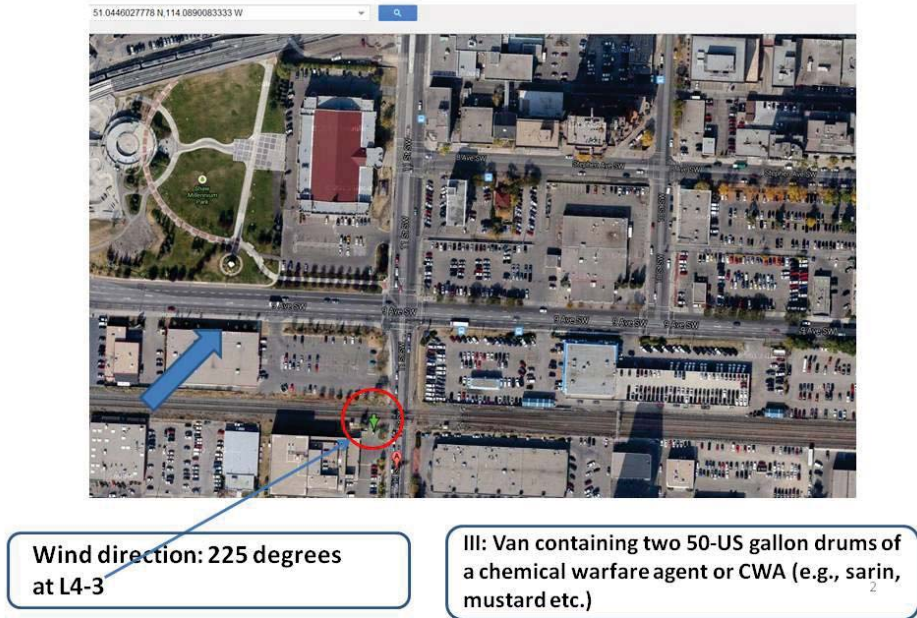
## Datasets delivered to 3DInternet [Δt=1 sec]



**Wind direction: 225 degrees at L4-2**

**III: Van containing two 50-US gallon drums of a chemical warfare agent or CWA (e.g., sarin, mustard etc.)**

**Figure 63.** Scenario 3 – Location of the source L4-2 at (51 deg, 02', 41.30" N, 114 deg, 05', 17.71" W) at a wind direction of 225°.



Time= 0300 sec

$\log_{10}(C)$

**Figure 64.** Scenario 3 – Top view of contours of concentration on a logarithmic scale at $t = 5$ min at a wind direction of 225° with the source L4-2 located at (51 deg, 02', 41.30" N, 114 deg, 05', 17.71" W).
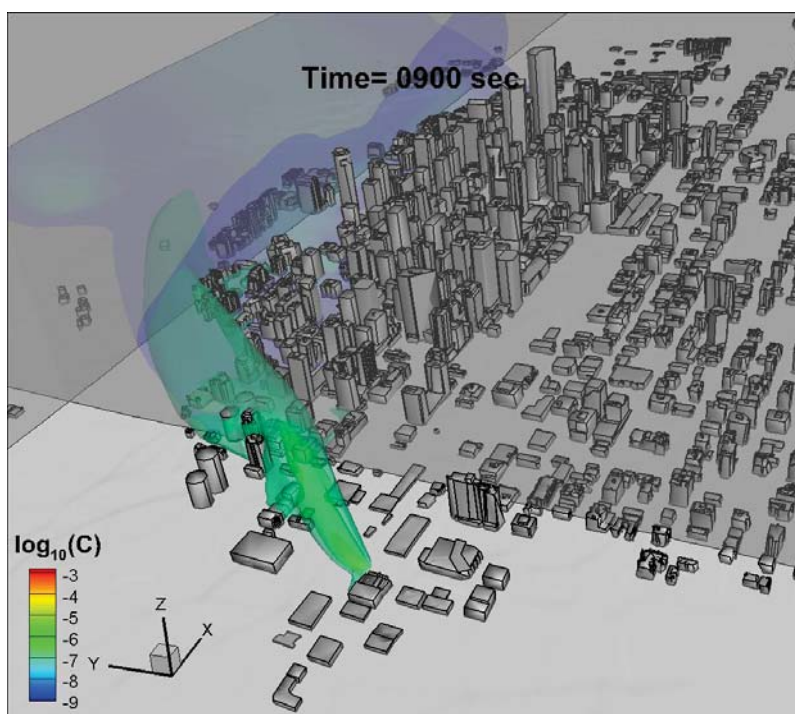
**Figure 65.** Scenario 3 – Contours of concentration on a logarithmic scale at *t* = 5 min at a wind direction of 225° with the source L4-2 located at (51 deg, 02', 41.30" N, 114 deg, 05', 17.71" W).



**Figure 66.** Scenario 3 – Contours of concentration on a logarithmic scale at *t* = 15 min at a wind direction of 225° with the source L4-2 located at (51 deg, 02', 41.30" N, 114 deg, 05', 17.71" W).

Datasets delivered to 3DInternet [**Δt=1 sec**]

Wind direction: 225 degrees at L4-3

III: Van containing two 50-US gallon drums of a chemical warfare agent or CWA (e.g., sarin, mustard etc.)

**Figure 67.** Scenario 3 – Location of the source L4-3 at (51 deg, 02', 40.57" N, 114 deg, 05', 20.43" W) at a wind direction of 225°.



Time= 0300 sec

$\log_{10}(C)$
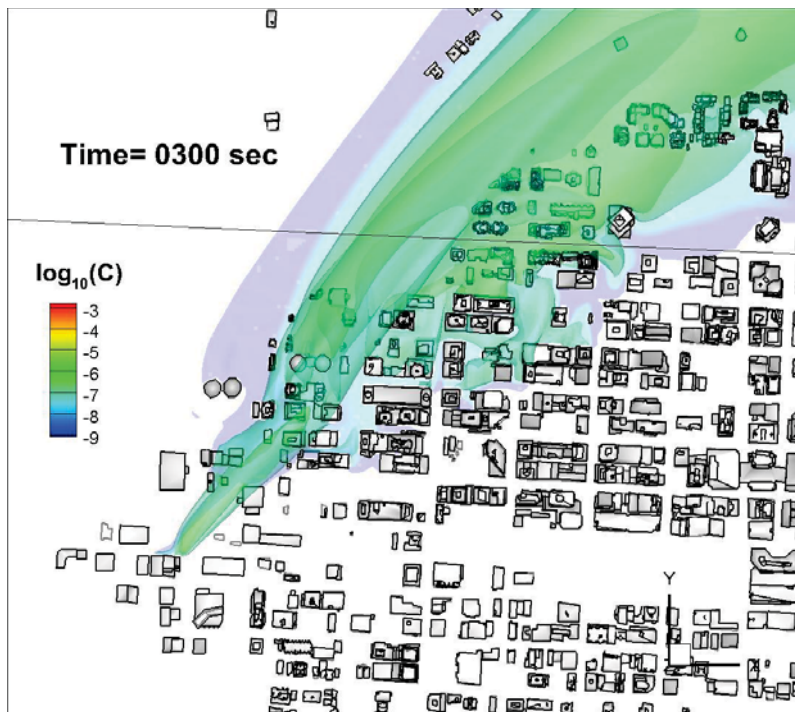
**Figure 68.** Scenario 3 – Top view of contours of concentration on a logarithmic scale at $t = 5$ min at a wind direction of 225° with the source L4-3 located at (51 deg, 02', 40.57" N, 114 deg, 05', 20.43" W).
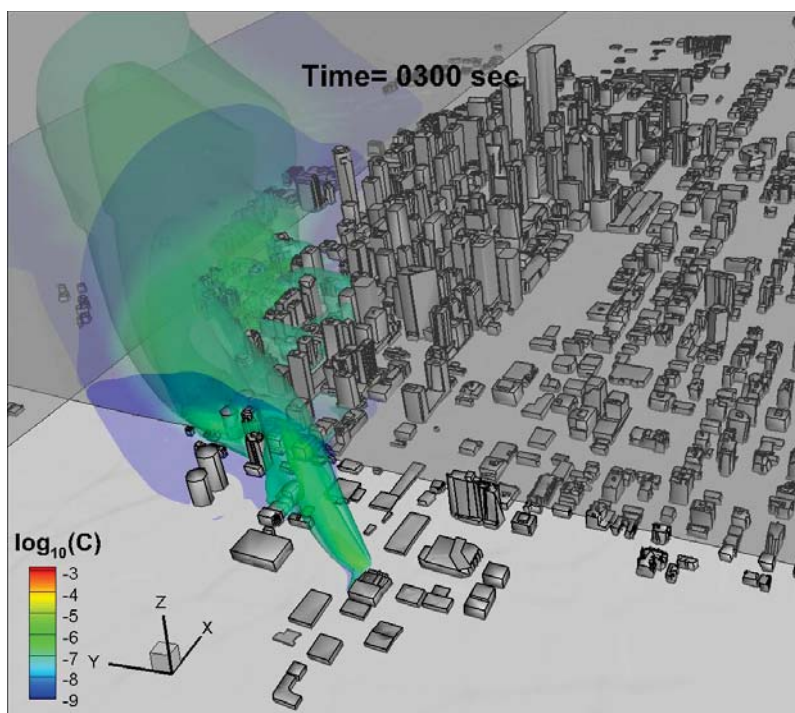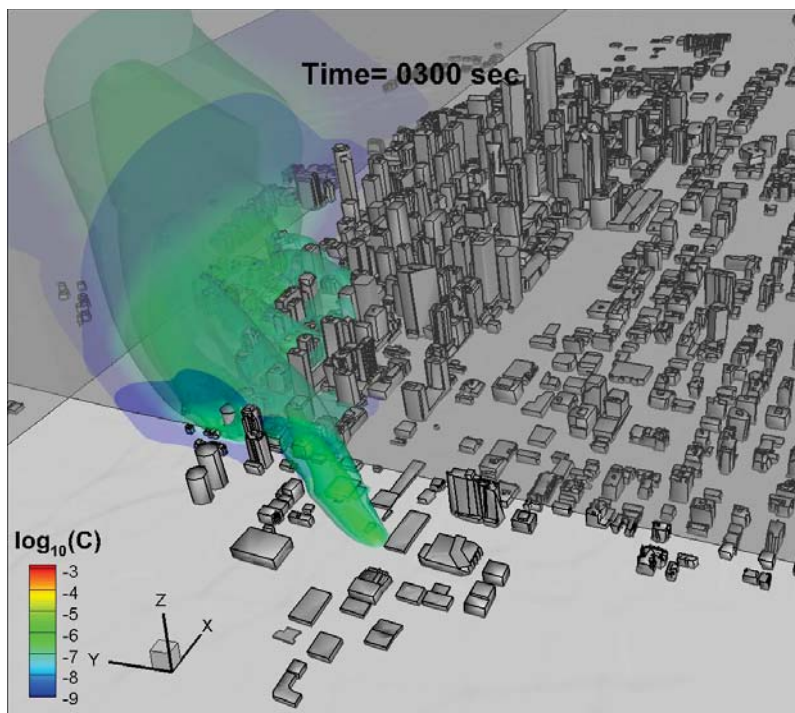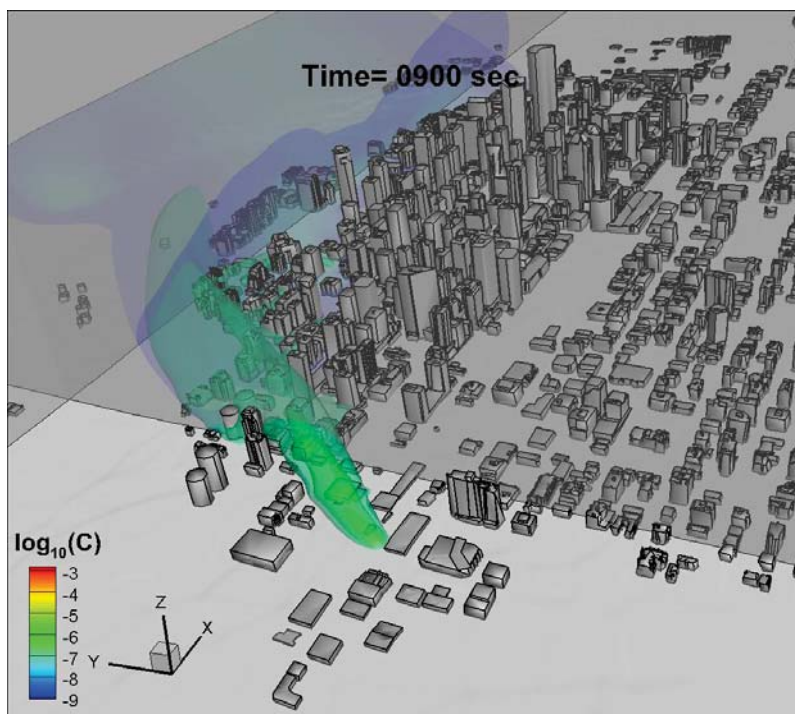
**Figure 69.** Scenario 3 – Contours of concentration on a logarithmic scale at $t$ = 5 min at a wind direction of 225° with the source L4-3 located at (51 deg, 02', 40.57" N, 114 deg, 05', 20.43" W).



**Figure 70.** Scenario 3 – Contours of concentration on a logarithmic scale at $t$ = 15 min at a wind direction of 225° with the source L4-3 located at (51 deg, 02', 40.57" N, 114 deg, 05', 20.43" W).

Datasets delivered to 3DInternet [**Δt=1 sec**]
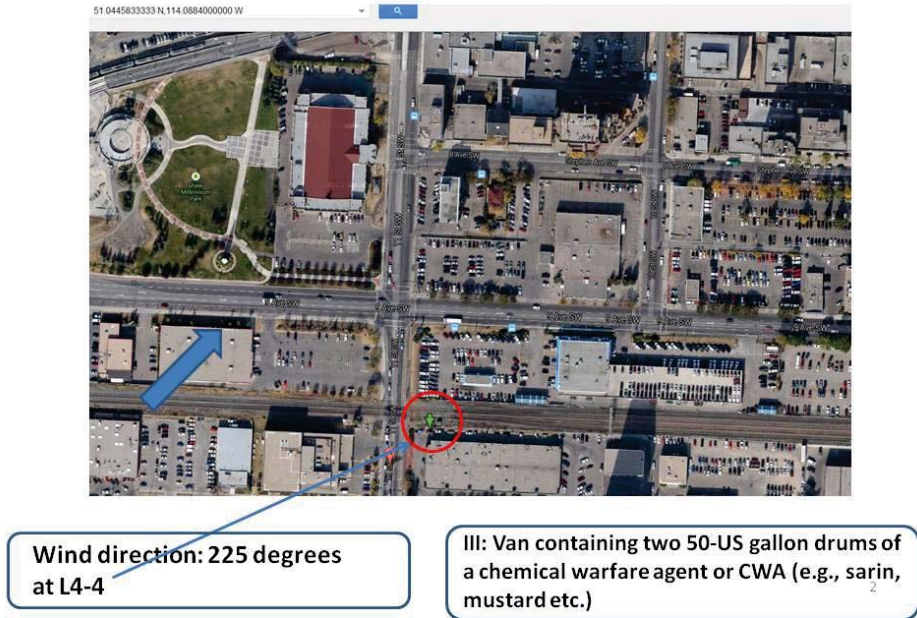


**Figure 71.** Scenario 3 – Location of the source L4-4 at (51 deg, 02', 40.50" N, 114 deg, 05', 18.24" W) at a wind direction of 225°.
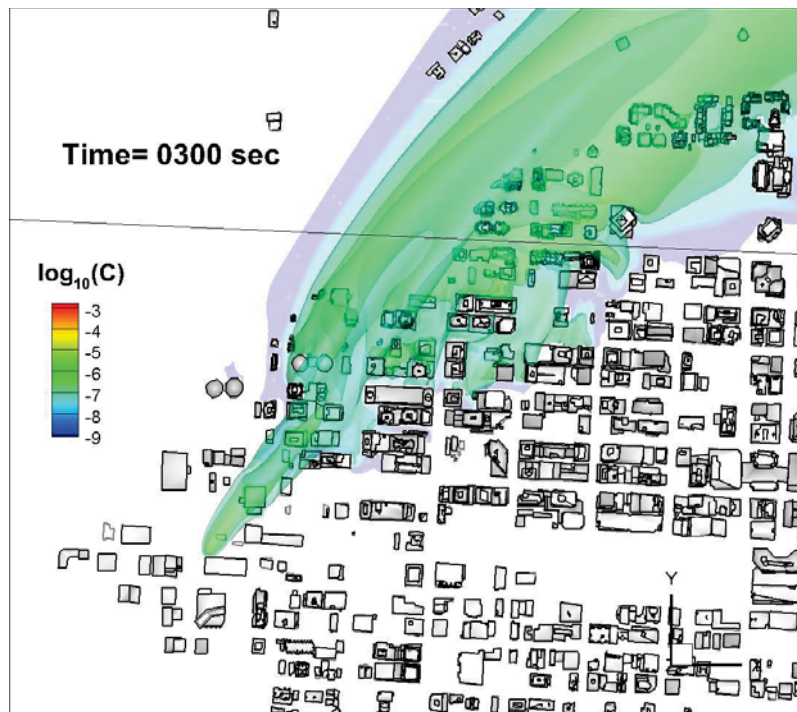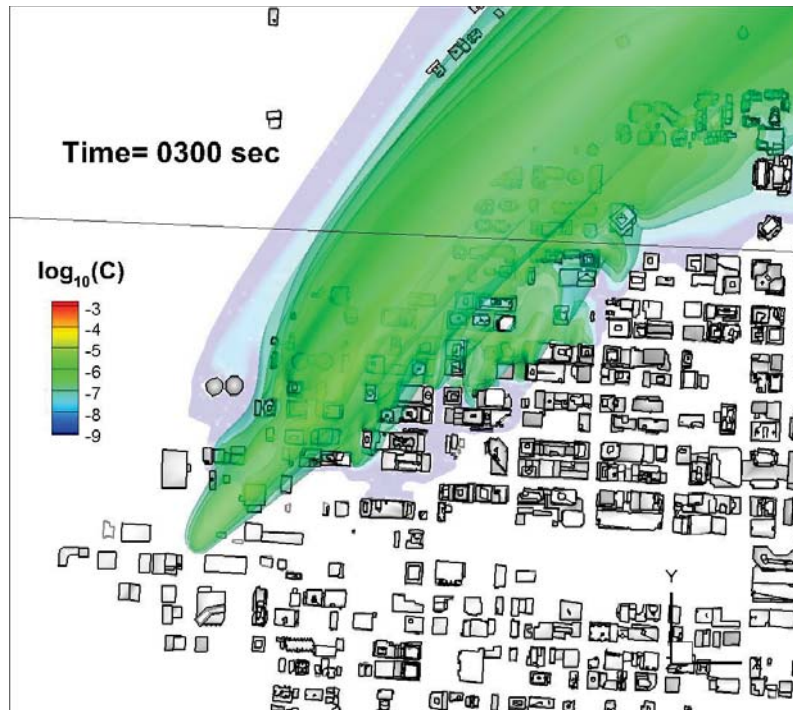


**Figure 72.** Scenario 3 – Top view of contours of concentration on a logarithmic scale at *t* = 5 min at a wind direction of 225° with the source L4-4 located at (51 deg, 02', 40.50" N, 114 deg, 05', 18.24" W).
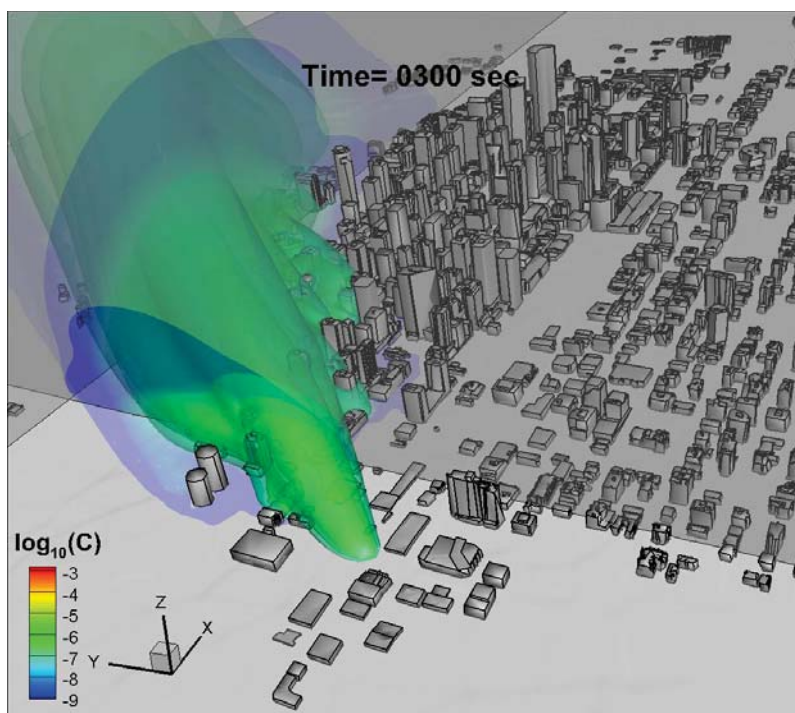
**Figure 73.** Scenario 3 – Contours of concentration on a logarithmic scale at $t$ = 5 min at a wind direction of 225° with the source L4-4 located at (51 deg, 02', 40.50" N, 114 deg, 05', 18.24" W).



**Figure 74.** Scenario 3 – Contours of concentration on a logarithmic scale at $t$ = 15 min at a wind direction of 225° with the source L4-4 located at (51 deg, 02', 40.50" N, 114 deg, 05', 18.24" W).
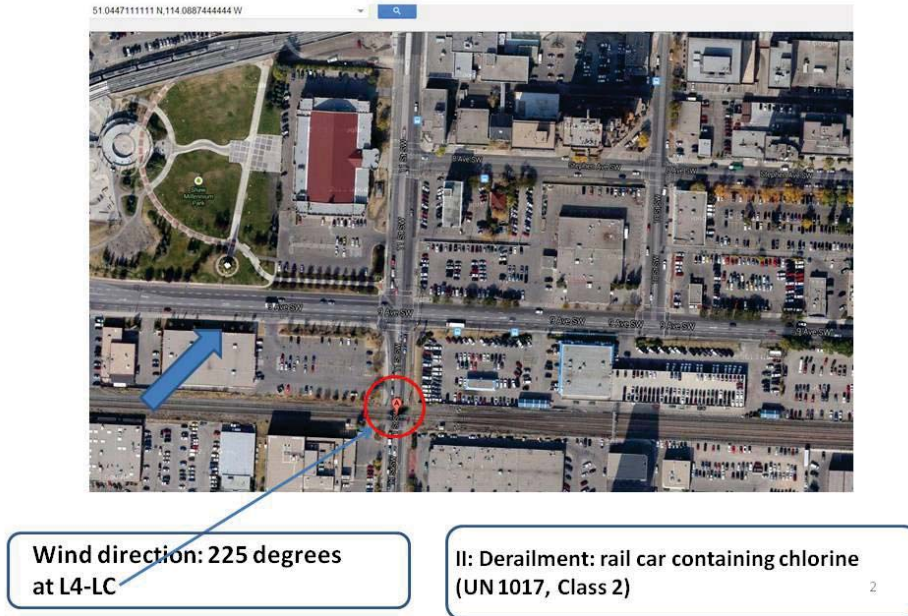
**Figure 75.** Scenario 3 – Location of the source L4-LC at (51 deg, 02', 40.96" N, 114 deg, 05', 19.48" W) at a wind direction of 225°.



**Figure 76.** Scenario 3 – Top view of contours of concentration on a logarithmic scale at $t$ = 5 min at a wind direction of 225° with the source L4-LC located at (51 deg, 02', 40.96" N, 114 deg, 05', 19.48" W).

**Figure 77.** Scenario 3 – Contours of concentration on a logarithmic scale at $t$ = 5 min at a wind direction of 225° with the source L4-LC located at (51 deg, 02', 40.96" N, 114 deg, 05', 19.48" W).
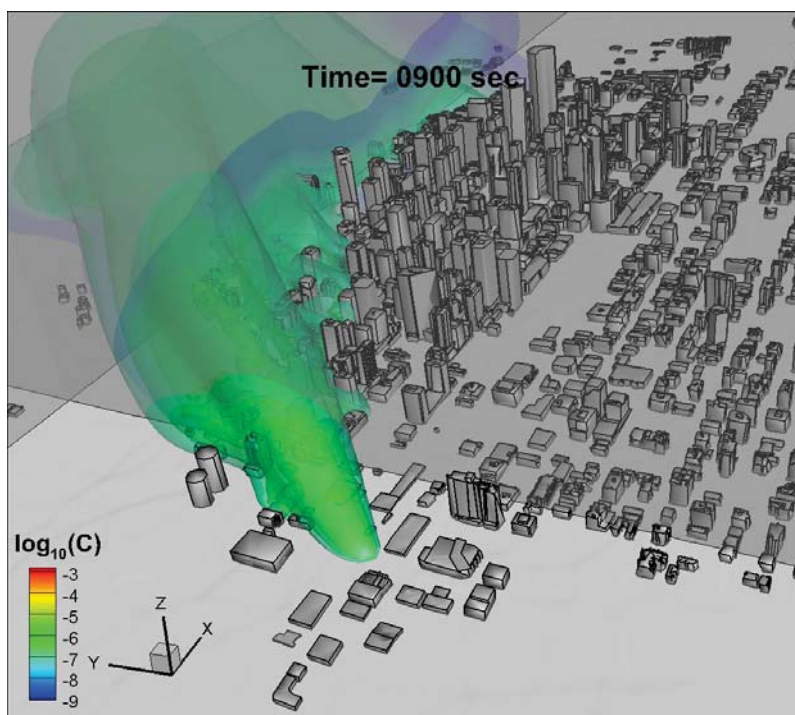


**Figure 78.** Contours of concentration on a logarithmic scale at $t$ = 15 min at a wind direction of 225° with the source L4-LC located at (51 deg, 02', 40.96" N, 114 deg, 05', 19.48" W).

74
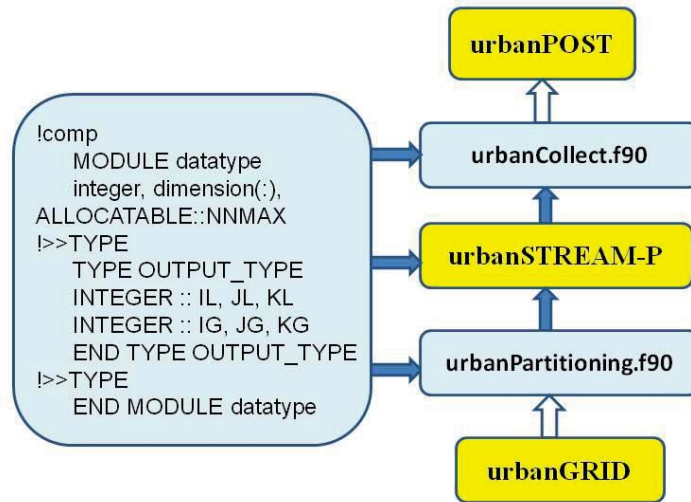
**Figure 79.** Illustration of compact data structure being used in `urbanPartitioning.f90`, `urbanCollect.f90` and urbanSTREAM-P. Note that `urbanPartitioning.f90` and `urbanCollect.f90` are pre-processor and post-processor of urbanSTREAM-P interfacing urbanGRID and urbanPOST.
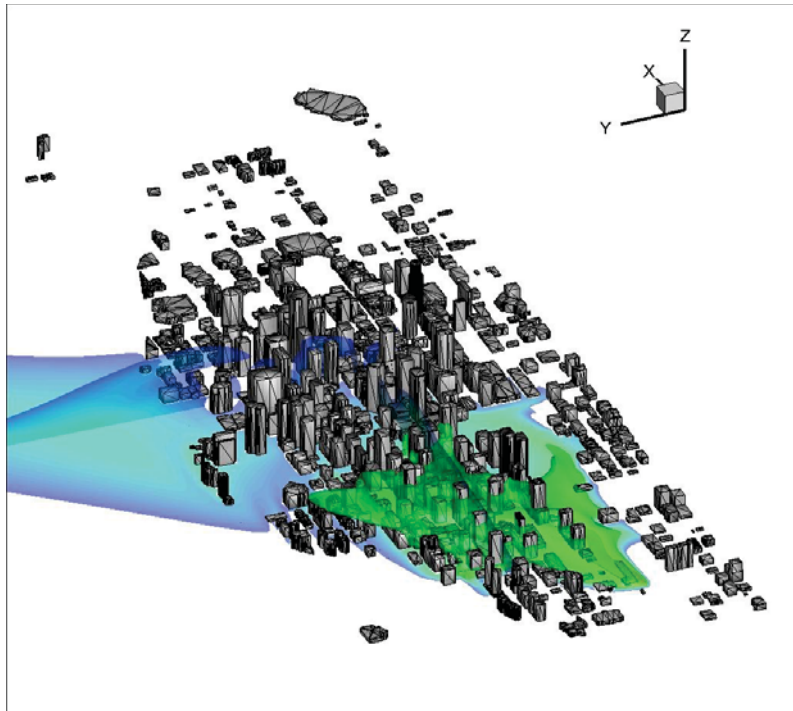


**Figure 80.** Scenario 1 – Contours of concentration on a logarithmic scale at $t = 30$ min for southwest wind direction. No compact data structure is used (viz., compression ratio is 100%).
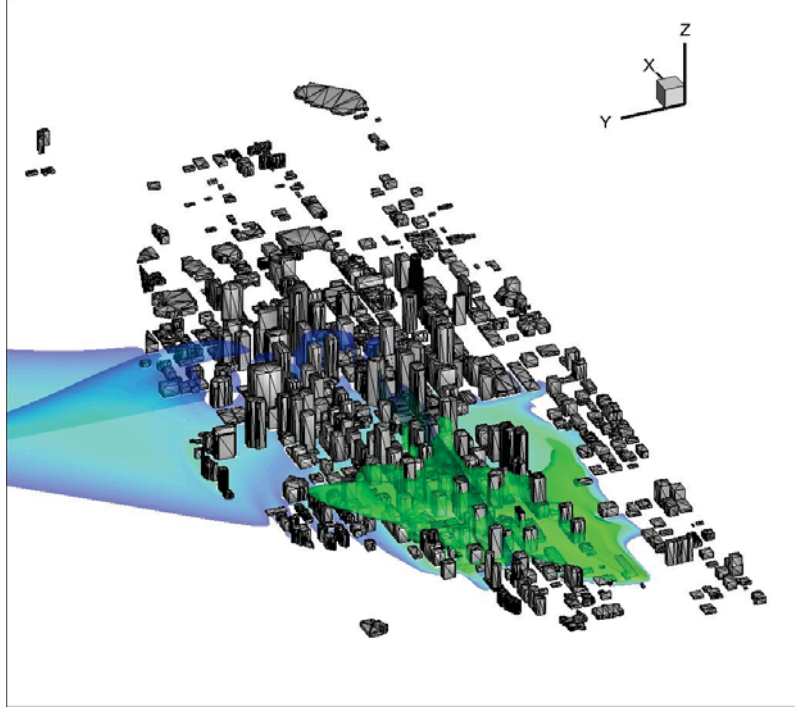
**Figure 81.** Scenario 1 – Contours of concentration on a logarithmic scale at $t = 30$ min for southwest wind direction. The compact data structure is employed, and the compression ratio is 27% with $C_{cut-off}=1.E-20$ kg/m$^3$.



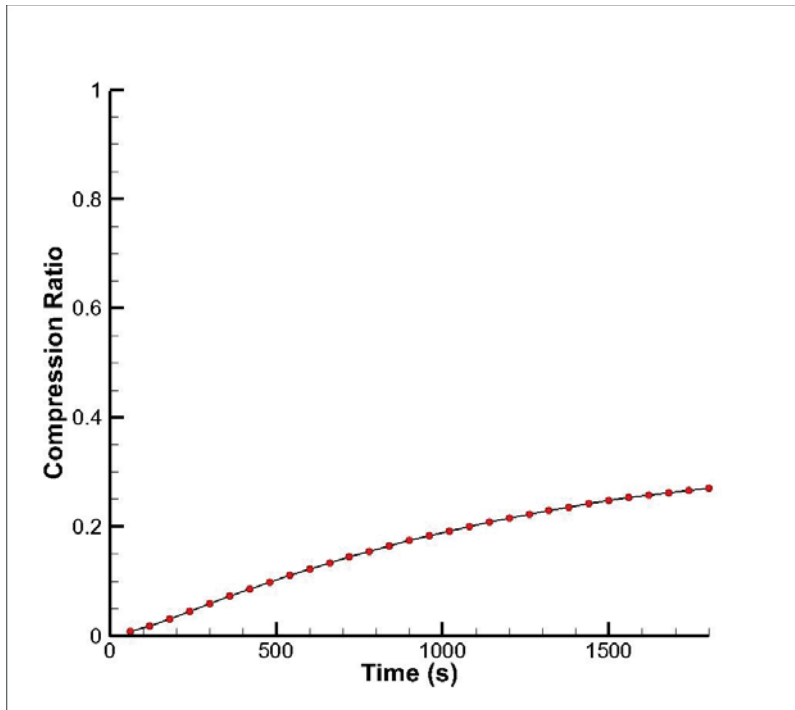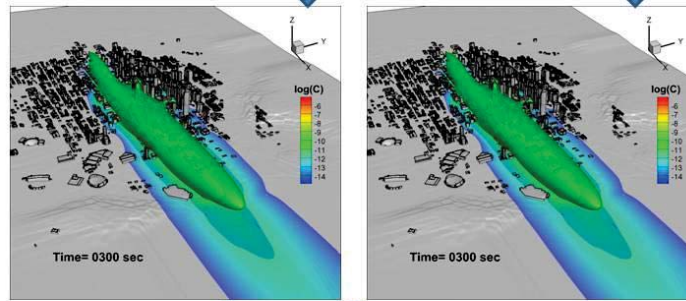**Figure 82.** Time history of compression ratio for the concentration data using the compact data structure for Scenario 1 (see also Figure 81).

**Figure 83.** Scenario 1 – Sample concentration results obtained from urbanPOST and `read_data.f90` for west wind direction (or 270° wind direction) at $t = 300$ sec to show the validity of the data converter: `read_data.f90` (see also Appendix A).
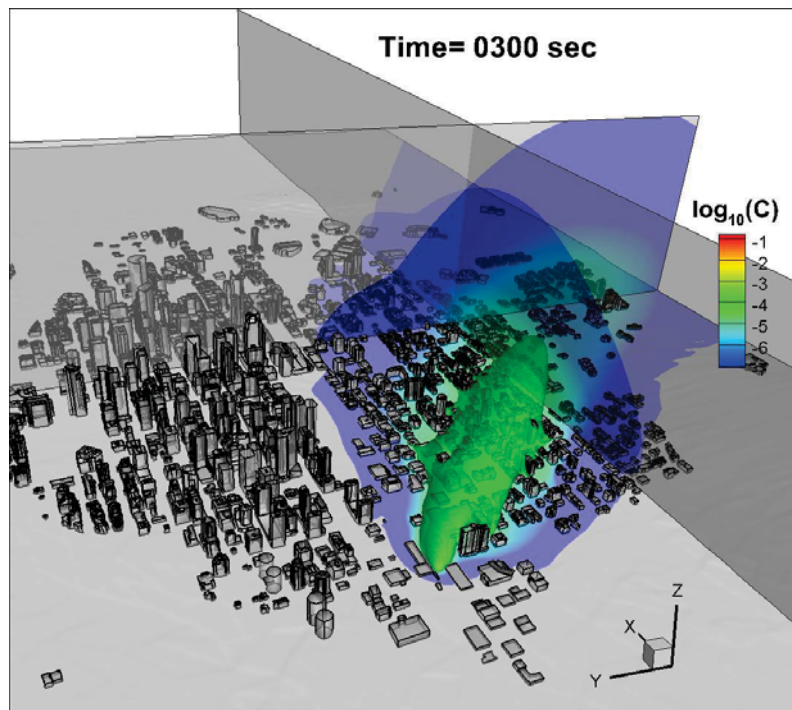


**Figure 84.** Scenario 1 – Contours of concentration on a logarithmic scale at $t = 5$ min at a wind direction of 315° from a source of continuous release.
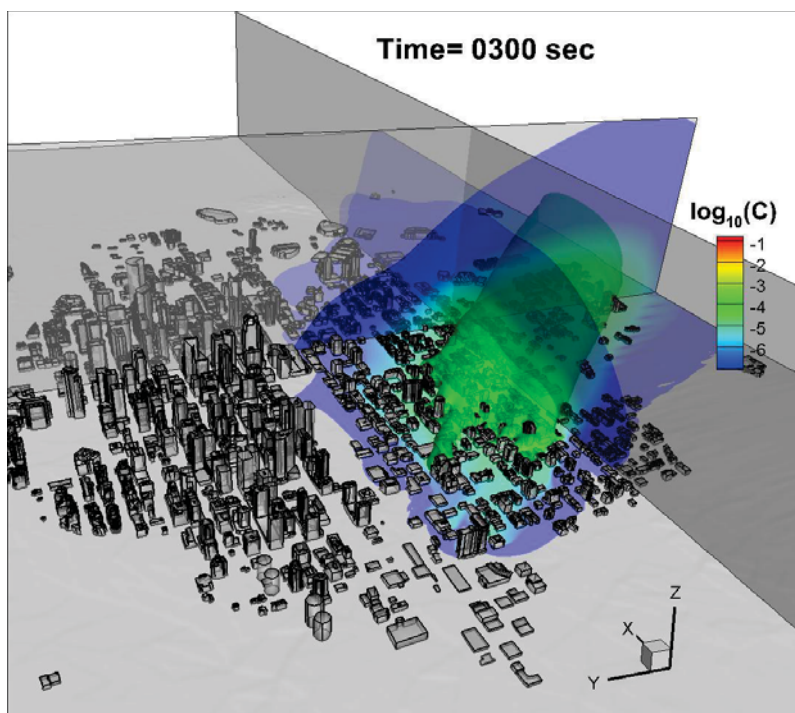
**Figure 85.** Scenario 1 – Contours of concentration on a logarithmic scale at $t$ = 5 min at a wind direction of 315° from a source of puff release.
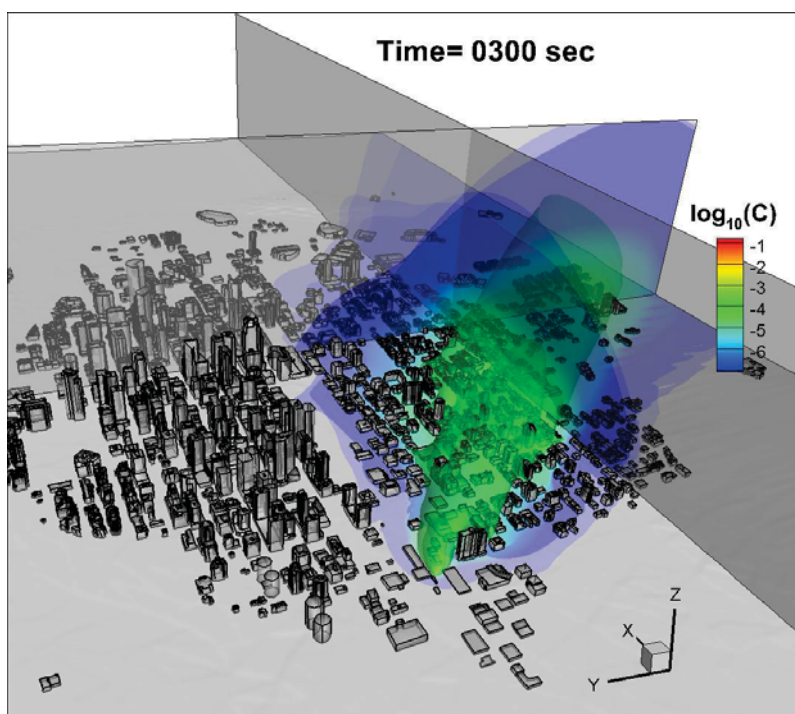


**Figure 86.** Scenario 1 – Contours of concentration on a logarithmic scale at $t$ = 5 min at a wind direction of 315° from a source of combining both continuous and puff releases.